



**POLITECNICO**  
MILANO 1863

SCUOLA DI INGEGNERIA INDUSTRIALE  
E DELL'INFORMAZIONE

# Tensor-Based Compression and Interpolation of Electron-Phonon Matrix Elements: Towards AbInitio Diagrammatic Monte Carlo

TESI DI LAUREA MAGISTRALE IN  
ENGINEERING PHYSICS - INGEGNERIA FISICA

Author: **Davide Patricelli**

Student ID: 250933

Advisor: Prof. Paolo Biscari

Co-advisors: Cesare Franchini

Academic Year: 2024 - 25



# Abstract



## Abstract in lingua italiana



# Contents

<b>Abstract</b>	i
<b>Abstract in lingua italiana</b>	iii
<b>Contents</b>	v
<b>Introduction</b>	1
<b>1 Electrons</b>	3
1.1 Electrons in a Periodic Potential . . . . .	4
1.1.1 Real Space . . . . .	4
1.1.2 Reciprocal Space . . . . .	7
1.1.3 Bloch Theorem and the wavefunction symmetry . . . . .	10
1.2 Density Functional Theory . . . . .	14
1.2.1 Hartree-Fock Ansatz . . . . .	15
1.2.2 Hohenberg-Kohn Theorems . . . . .	16
1.2.3 Kohn-Sham Equations . . . . .	17
1.3 Second Quantization . . . . .	21
1.3.1 Creation and Annihilation Operators . . . . .	22
1.3.2 Operators in Second Quantization . . . . .	23
1.3.3 Non-Interacting Electronic Hamiltonian in Second Quantization .	24
<b>2 Phonons</b>	27
2.1 Lattice Vibrations . . . . .	27
2.1.1 Born–Oppenheimer Approximation . . . . .	27
2.1.2 Harmonic Approximation . . . . .	28
2.1.3 Dynamical Matrix . . . . .	30
2.1.4 Symmetries . . . . .	31
2.1.5 Acoustic Sum Rule . . . . .	33

2.2	Phonons in Density Functional Theory . . . . .	34
2.2.1	Finite Difference Method . . . . .	34
2.2.2	Density Functional Perturbation Theory (DFPT) . . . . .	35
2.3	Phonon Quantization . . . . .	36
2.3.1	Bosonic Nature of Phonons . . . . .	38
2.4	The Electron-Phonon Interaction . . . . .	38
2.4.1	Interaction Hamiltonian . . . . .	39
2.4.2	Screening and Linear Response . . . . .	41
2.4.3	Electron-Phonon Coupling in Density Functional Theory . . . . .	41
<b>3</b>	<b>Diagrammatic Monte Carlo</b>	<b>43</b>
3.1	Quantum Many-Body Theory . . . . .	43
3.1.1	Time Evolution . . . . .	43
3.1.2	Green Function . . . . .	46
3.1.3	Finite Temperature . . . . .	49
3.1.4	Reduction Formula . . . . .	51
3.1.5	From Wick Theorem to Feynman Diagrams . . . . .	54
3.2	From Perturbation Expansion to Monte Carlo Simulation of the Holstein Model . . . . .	58
3.2.1	Monte Carlo Integration . . . . .	59
3.2.2	Green Function Histogram . . . . .	60
3.2.3	Markov Chain Monte Carlo and Detailed Balance . . . . .	63
3.2.4	Blocking Analysis . . . . .	65
3.3	Momentum and Band-Resolved Implementation . . . . .	66
3.3.1	Electron-Phonon Diagram Anatomy . . . . .	66
3.3.2	Improved Estimator for the Green Function . . . . .	71
3.3.3	Energy Estimator . . . . .	72
3.3.4	Results: Breathing Electron-Phonon Coupling . . . . .	73
<b>4</b>	<b>Tensor Decomposition and Interpolation</b>	<b>77</b>
4.1	Generalized Fourier Interpolation . . . . .	77
4.1.1	Wannier Function . . . . .	79
4.1.2	Maximally Localized Wannier Functions . . . . .	81
4.1.3	Deformation Potential Transformation . . . . .	82
4.1.4	Electron-Phonon Tensor in Momentum and Wannier Space . . . . .	86
4.2	Tensor Decomposition . . . . .	90
4.2.1	Low-Rank Approximation: From PCA to Tensor SVD . . . . .	90
4.2.2	Tucker Decomposition . . . . .	92

4.2.3	Notes on the implementation . . . . .	94
4.2.4	Compression Results . . . . .	95
4.2.5	Structure of the Tensor in Bloch and Wannier Representations . . .	97
4.3	Interpolation . . . . .	99
4.3.1	Wannier Interpolation . . . . .	100
4.3.2	Disentanglement . . . . .	100
4.3.3	Phonon Interpolation . . . . .	101
4.3.4	Matrix Element Interpolation . . . . .	102
<b>5</b>	<b>Back to Monte Carlo</b>	<b>107</b>
5.1	Interpolation performance . . . . .	107
5.2	Sign Problem . . . . .	110
5.3	Conclusions and Further Developments . . . . .	111
<b>Bibliography</b>		<b>113</b>
<b>A Appendix A</b>		<b>117</b>
<b>B Appendix B</b>		<b>119</b>
B.0.1	Add Update . . . . .	119
<b>Acknowledgements</b>		<b>121</b>



# Introduction

The aim of this thesis is to create and validate a bridge between two powerful methods in computational physics: Density Functional Theory, which allows the calculation of many quantities of interest *ab initio*, and Diagrammatic Monte Carlo, a stochastic method that can converge to practically exact theoretical results. The goal is therefore to motivate and develop a consistent framework that may be referred to as *ab initio* Diagrammatic Monte Carlo.

These methods are applied in particular to one of the fundamental interactions occurring in condensed matter: the interaction between electrons and phonons. This is an intrinsically interacting quantum many-body problem, at the basis of the accurate understanding of many physical phenomena and material properties, as well as of the formation of emergent quasiparticles such as the polaron.

The main obstacle in moving from DFT outputs to Monte Carlo simulations is that, in order to describe the interaction between these fermionic and bosonic degrees of freedom within an effective Hamiltonian, one needs access to a high-dimensional tensor encoding the electron–phonon coupling. Computing and storing this tensor in full is impractical. While interpolation techniques exist, their computational cost is typically too high to be compatible with the repeated evaluations required in a Diagrammatic Monte Carlo simulation.

To overcome this limitation, it is necessary to reformulate the problem at the level of its representation. In the Bloch basis, the electron–phonon coupling tensor is intrinsically high-dimensional and delocalized, making any direct compression ineffective. By transforming the problem to the Wannier representation, where spatial locality becomes explicit, the tensor acquires a structured form that reveals an intrinsic low-rank character. We then introduce techniques from numerical linear algebra, commonly employed in data analysis and machine learning to handle high-dimensional datasets, and adapt them to the specific structural properties of the problem. This enables a controlled dimensionality reduction of the coupling tensor, reducing the computational complexity of the interpolation step and significantly accelerating the overall algorithm while preserving physical

accuracy.

In order to arrive at this point, Chapters 1 and 2 introduce, in a reasonably detailed manner, the description of electronic and vibrational degrees of freedom, together with their mutual coupling. Although this presentation may initially appear somewhat distant from the final computational objective, many aspects of the transformations developed later rely precisely on these solid-state physics concepts. At the same time, the basic principles of DFT calculations for the relevant quantities are introduced, with further details provided in Appendix A. Particular attention is devoted to clarifying the passage from semiclassical or first-quantized descriptions to a fully second-quantized formulation, which is essential for embedding the problem within a many-body framework.

This provides the necessary foundation for Chapter 3, where the fundamental tools of quantum field theory in condensed matter physics are introduced, together with the concept of quantum correlators and Feynman diagrams. From this perspective, the construction of a Monte Carlo method based on the diagrammatic expansion of many-body theory follows naturally. The chapter is completed with the considerations required for an *ab initio* implementation that retains full momentum and band dependence.

This, in turn, highlights the necessity of not directly using raw DFT outputs, but instead defining techniques that allow the low-rank factorization, compression, and efficient interpolation of the electron–phonon tensor through advanced linear algebra tools and a generalized Fourier interpolation scheme. This central development is addressed in Chapter 4.

Finally, the last chapter discusses the effects and implications of inserting these methods into a Diagrammatic Monte Carlo framework, outlining both the limitations encountered and possible directions for future developments.

The text presents the main theoretical foundations together with the corresponding implementation aspects. Given the strongly computational character of the thesis, implementation details are provided in the appendices: Appendix A contains the DFT calculations and the Python scripts used to process their outputs, while Appendix B describes the development of the Monte Carlo code.

# 1 | Electrons

## Introduction

In a certain sense, the problem of writing down the complete equation describing the interaction of electrons in a solid is not difficult, at least if one neglects spin degrees of freedom and the internal structure of the ions. Treating the ions as pointlike charged particles of charge  $Ze$ , and considering only electrostatic interactions between ion–ion, electron–ion, and electron–electron pairs, the system is described by the following non-relativistic Hamiltonian:

$$\hat{H} = -\sum_{i=1}^{N_e} \frac{\hbar^2}{2m} \nabla_i^2 - \sum_{I=1}^{N_p} \frac{\hbar^2}{2M_I} \nabla_I^2 + \frac{1}{2} \sum_{\substack{i,j=1 \\ i \neq j}}^{N_e} \frac{e^2}{|\mathbf{r}_i - \mathbf{r}_j|} + \frac{1}{2} \sum_{\substack{I,J=1 \\ I \neq J}}^{N_p} \frac{Z^2 e^2}{|\mathbf{R}_I - \mathbf{R}_J|} - \sum_{i=1}^{N_e} \sum_{I=1}^{N_p} \frac{Ze^2}{|\mathbf{r}_i - \mathbf{R}_I|}$$

The corresponding many-body wavefunction depends on all electronic and ionic coordinates,

$$\psi = \psi(\mathbf{r}_1, \dots, \mathbf{r}_{N_e}; \mathbf{R}_1, \dots, \mathbf{R}_{N_p}),$$

and satisfies the time-independent Schrödinger equation

$$\hat{H}\psi = E\psi.$$

In principle, solving this eigenvalue problem would allow for a complete microscopic description of many of the phases observed in quantum materials, chemistry, and materials science more generally. In practice, however, this task is computationally intractable. The Hilbert space to which the many-body wavefunction belongs grows exponentially with the number of particles, while physically relevant systems typically involve particle numbers of the order of Avogadro's number. Indeed, it has been rigorously shown that even on a quantum computer the exact diagonalization of generic many-body electronic Hamiltonians requires exponential time in the system size [1]. Nevertheless, over the past decades a wide range of approximations and theoretical tools have been developed that render the quantum many-body problem tractable in practice. The aim of this chapter

and following is to introduce the conceptual framework and approximations within which the many-body problem will be addressed throughout this thesis.

## 1.1. Electrons in a Periodic Potential

One of the aspects that plays a central role both in Density Functional Theory calculations and, even more prominently, in Chapter 4, where transformations of the basis describing the physics of the problem are introduced, is the symmetry of the crystal lattice and the properties of the quantum problem that can be deduced from it.

Crystal symmetries have a direct impact on practical DFT calculations, as they reduce the number of independent points that need to be explicitly considered and guide the sampling of the Brillouin zone. At the same time, they play a fundamental role in the definition of basis transformations and tensor representations of physical quantities.

This section is therefore devoted to recalling these symmetry principles, which, explicitly or implicitly, form the foundation of the following analysis and are deeply embedded in the structure of the numerical methods and codes employed throughout this work [2, 3].

### 1.1.1. Real Space

The first quantum theory of electrons in a static crystal was developed by Bloch in 1928. The starting point is that in a crystal, ions are arranged in a regular periodic array, which is translationally invariant. Specifically, the full lattice is specified by all integer linear combinations of three non-coplanar vectors  $\mathbf{a}_1, \mathbf{a}_2, \mathbf{a}_3$ . The position of an ion  $p$  is given by:

$$\mathbf{R}_p = n_1 \mathbf{a}_1 + n_2 \mathbf{a}_2 + n_3 \mathbf{a}_3 \quad (1.1)$$

The set of vectors  $\mathbf{R}_p$  is closed under vector addition and subtraction and thus respect the definition of a Bravais Lattice. This implies that the lattice is translationally invariant. As a consequence, if we define the translation operator acting on a function of space as:

$$\hat{T}_{\mathbf{R}} f(\mathbf{r}) = f(\mathbf{r} + \mathbf{R}), \quad (1.2)$$

we expect quantities directly related to the ions arrangement, such as the electron-ion electrostatic potential, to respect this symmetry:

$$\hat{T}_{\mathbf{R}_p} U_I(\mathbf{r}) \equiv U_I(\mathbf{r} + \mathbf{R}_p) = U_I(\mathbf{r}). \quad (1.3)$$

In addition, the crystal is expected to be symmetric under a set of point operations, such as rotations, reflections, and inversion, which form a group known as the **Point Group**  $\mathcal{G}$  of the Bravais lattice. Combining these point operations with the translational symmetry yields a larger group called the **Space Group**. It can be shown that, due to the periodic arrangement, only certain rotations are possible (e.g., 1, 2, 3, 4, and 6-fold), and there exists a limited number of possible point groups and Bravais lattices in each dimension.

More importantly, the potential introduced before is also invariant under these symmetry operations:

$$\hat{\mathcal{R}} U_I(\mathbf{r}) \equiv U_I(\hat{\mathcal{R}}^{-1}\mathbf{r}) = U_I(\mathbf{r}), \quad \hat{\mathcal{R}}, \hat{\mathcal{R}}^{-1} \in \mathcal{G}. \quad (1.4)$$

We can thus start, considering the Schrödinger equation for a single electron, neglecting the explicit electron-electron Coulomb interaction, in a generic periodic potential that can, in principle, also include effective electron contributions, plus the electron-ion  $U_I$  previously introduced:

$$\hat{H}(\mathbf{r})\psi(\mathbf{r}) = \left( -\frac{\hbar^2}{2m} \nabla^2 + U(\mathbf{r}) \right) \psi(\mathbf{r}) = \varepsilon \psi(\mathbf{r}). \quad (1.5)$$

Since the Laplace operator has spherical symmetry<sup>1</sup>, the full symmetry of the Hamiltonian in (1.5) is determined by the symmetry of the potential  $U$ .

Both in analytical and computational calculations, rather than working with an infinite system, it is convenient to exploit the periodicity of the lattice and restrict the description to a finite volume. For this purpose, the concept of the **primitive cell** is widely used. It is defined as a volume of space containing a single lattice point that, when translated by all lattice vectors, tiles the entire space without overlap. A common choice is the parallelepiped spanned by the primitive lattice vectors  $\mathbf{a}_i$ , such that any point inside the

---

<sup>1</sup>The Laplace operator  $\nabla^2$  is spherically symmetric because it is invariant under any rotation of the coordinate system. In Cartesian coordinates, it is the sum of second derivatives with respect to  $x, y$ , and  $z$ , treating all directions equally. When expressed in spherical coordinates, it naturally separates into radial and angular parts, reflecting the underlying spherical symmetry of space.

cell can be written as

$$\mathbf{r} = x_1 \mathbf{a}_1 + x_2 \mathbf{a}_2 + x_3 \mathbf{a}_3, \quad x_i \in [0, 1). \quad (1.6)$$

The primitive cell provides the most compact description of the lattice, but it does not necessarily reflect all the spatial symmetries of the underlying Bravais lattice. For this reason, it is often convenient to introduce the **conventional unit cell**, which also fills space by translation but may contain more than one lattice point. As illustrated in Fig. 1.1 (left), the conventional cell is typically chosen to make the symmetry of the crystal explicit, even at the cost of a larger volume.

Once a unit cell is specified, a crystal structure is fully determined by associating a *basis* of  $B$  atoms to each lattice point. Each atom in the basis is characterized by an internal position  $\boldsymbol{\tau}_\kappa$ , which can also be expressed in fractional coordinates according to Eq. (1.6). The absolute position of any ion in the crystal is then given by

$$\mathbf{R} = \mathbf{R}_p + \boldsymbol{\tau}_\kappa, \quad (1.7)$$

where  $\mathbf{R}_p$  labels the position of the unit cell in the lattice, as schematically shown in Fig. 1.1 (right).

In the following, we focus on a face-centered cubic (fcc) Bravais lattice, which is relevant for a variety of materials, including elemental silicon and ionic compounds such as LiF.

Additionally, although considering an infinite crystal is a very useful approximation, since all sites become equivalent, this is often impractical for calculations. A more practical approach is to consider a finite lattice with  $N = N_1 N_2 N_3$  sites, obtained from the lattice vectors  $\mathbf{a}_i$  but restricting the coefficients in the linear combination<sup>2</sup> (1.1) to  $n_i = 0, 1, \dots, N_i - 1$ .

We can then restore the translational and, more generally, the symmetry equivalence with respect to the infinite Bravais lattice by folding opposite sides of the finite lattice, imposing the so-called

**Born–von Kármán boundary conditions:**

$$\psi(\mathbf{r} + N_i \mathbf{a}_i) = \psi(\mathbf{r}), \quad i = 1, 2, 3. \quad (1.8)$$

---

<sup>2</sup>It is actually more common to use a centered system with  $n_i = -\frac{N_i}{2}, \dots, -1, 0, 1, \dots, \frac{N_i}{2} - 1$ .

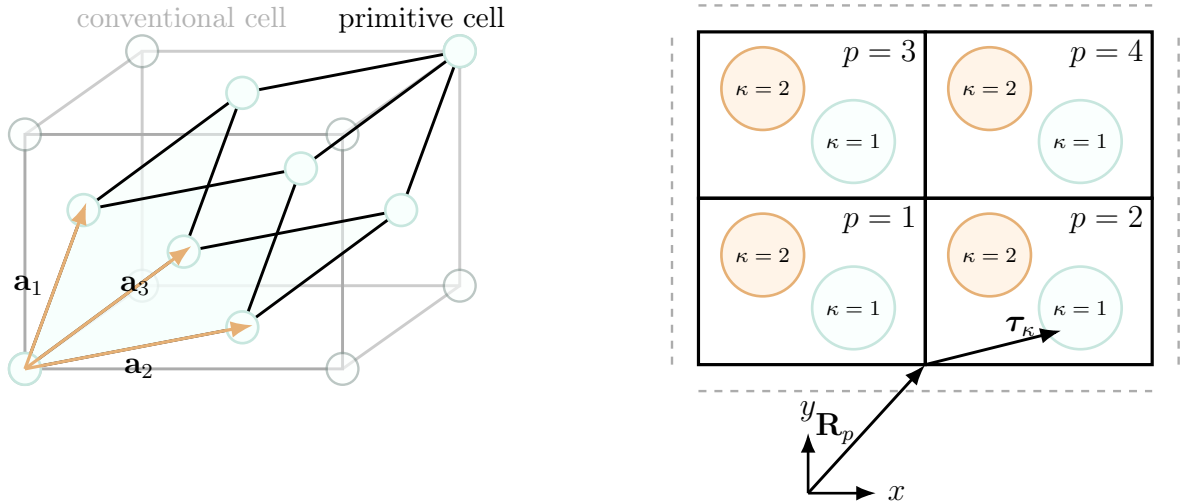


**Figure 1.1:** **Left:** Conventional cubic unit cell and embedded primitive cell of a face-centered cubic lattice, with one possible choice of primitive lattice vectors  $\mathbf{a}_i$ . **Right:** Two-dimensional schematic of a crystal lattice decomposed into unit cells labeled by  $\mathbf{R}_p$ , each containing a basis of atoms at internal positions  $\tau_\kappa$ .

In numerical calculations, one typically specifies either a single unit cell, in which case the code effectively performs a primitive-cell approximation, or a larger supercell composed of multiple unit cells, similar to the finite lattice described above. The numerical method then solves the problem exactly within this finite cell or supercell and enforces periodic boundary conditions, thereby approximating the infinite system while managing computational cost.

### 1.1.2. Reciprocal Space

Given the spatial periodicity of the system, it is natural to introduce a Fourier representation and work in momentum space rather than in real space. To perform such an expansion, we require a basis of plane waves that shares the periodicity of the lattice. This requirement can be expressed as:

$$e^{i\mathbf{G} \cdot (\mathbf{r} + \mathbf{R}_p)} = e^{i\mathbf{G} \cdot \mathbf{r}} \quad \forall \mathbf{r} \in \mathbb{R}^3, \mathbf{R}_p \in \text{Bravais lattice}, \quad (1.9a)$$

which implies

$$e^{i\mathbf{G} \cdot \mathbf{R}} = 1. \quad (1.9b)$$

This condition defines a set of momentum vectors that itself forms a Bravais lattice<sup>3</sup>,

---

<sup>3</sup>If  $\mathbf{G}_1$  and  $\mathbf{G}_2$  belong to the reciprocal lattice, then their sum and difference also satisfy Eq. (1.9b).

commonly referred to as the *reciprocal lattice*. As a consequence, any reciprocal lattice vector can be written as an integer linear combination of three primitive vectors,

$$\mathbf{G} = m_1 \mathbf{b}_1 + m_2 \mathbf{b}_2 + m_3 \mathbf{b}_3,$$

where the reciprocal lattice vectors satisfy the orthogonality condition

$$\mathbf{b}_i \cdot \mathbf{a}_j = 2\pi\delta_{ij}, \quad i, j = 1, 2, 3, \quad (1.10)$$

with  $\delta_{ij}$  denoting the Kronecker delta.

As in real space, reciprocal space can be tiled by repeating a primitive cell, which is most commonly chosen to be the *First Brillouin Zone* (FBZ)<sup>4</sup>.

The Fourier expansion of a function that shares the periodicity of the lattice, such as the Coulomb potential, can then be written as:

$$U(\mathbf{r}) = \sum_{\mathbf{G}} e^{i\mathbf{G}\cdot\mathbf{r}} U_{\mathbf{G}}, \quad (1.11a)$$

$$U_{\mathbf{G}} = \frac{1}{v} \int_{\text{P.C.}} d\mathbf{r} e^{-i\mathbf{G}\cdot\mathbf{r}} U(\mathbf{r}), \quad (1.11b)$$

where the integral is performed over the primitive cell and  $v$  denotes its volume.

It is worth emphasizing the Fourier duality between real space and reciprocal space. For instance, Eq. (1.9b) implies that the volume of the First Brillouin Zone is

$$V_{\text{FBZ}} = \frac{(2\pi)^3}{v}.$$

Turning now to the wavefunction, under the periodic boundary conditions introduced in Eq. (1.8), it acquires a periodicity of  $N_i \mathbf{a}_i$  along each lattice direction. This allows it to be expanded as a Fourier series over a discrete set of wavevectors. The allowed momenta satisfy

$$e^{i\mathbf{k}\cdot(N_i \mathbf{a}_i)} = 1 \quad \Rightarrow \quad \mathbf{k} = \sum_{i=1}^3 \frac{m_i}{N_i} \mathbf{b}_i, \quad (1.12a)$$

---

<sup>4</sup>While a primitive cell is not uniquely defined in general, the First Brillouin Zone corresponds to a specific choice: the Wigner–Seitz cell of the reciprocal lattice. It is constructed as the set of points closer to the origin than to any other reciprocal lattice point and inherits the full symmetry of the lattice.

and the wavefunction can be written as

$$\psi(\mathbf{r}) = \sum_{\mathbf{k}} e^{i\mathbf{k}\cdot\mathbf{r}} \psi_{\mathbf{k}}, \quad (1.13a)$$

$$\psi_{\mathbf{k}} = \frac{1}{V} \int d\mathbf{r} e^{-i\mathbf{k}\cdot\mathbf{r}} \psi(\mathbf{r}), \quad (1.13b)$$

where the integral is taken over the finite volume  $V$  on which periodic boundary conditions are imposed.

Physical quantities are often expressed in terms of wavevectors folded into the First Brillouin Zone. In this representation, reciprocal space is no longer continuous but discretized due to the finite system size, with a spacing

$$\Delta\mathbf{k} = \frac{(2\pi)^3}{V} \quad (1.14)$$

Replacing the Fourier series for the potential and the wavefunction in the Schrödinger equation (1.5), we take advantage of the fact that derivatives become algebraic operations in the kinetic term, while the potential term reads:

$$U(\mathbf{r})\psi(\mathbf{r}) = \sum_{\mathbf{G}} \sum_{\mathbf{k}} e^{i(\mathbf{G}+\mathbf{k})\cdot\mathbf{r}} U_{\mathbf{G}} c_{\mathbf{k}} = \sum_{\mathbf{G}} \sum_{\mathbf{k}'} e^{i\mathbf{k}'\cdot\mathbf{r}} U_{\mathbf{G}} c_{\mathbf{k}'-\mathbf{G}} = \sum_{\mathbf{k}} \sum_{\mathbf{G}'} e^{i\mathbf{k}\cdot\mathbf{r}} U_{\mathbf{G}'} c_{\mathbf{k}-\mathbf{G'}}. \quad (1.15)$$

Here we have introduced the change of variables  $\mathbf{k}' = \mathbf{k} + \mathbf{G}$  and used the fact that, within the discrete  $\mathbf{k}$ -mesh defined in Eq. (1.12a), adding or subtracting a reciprocal lattice vector  $\mathbf{G}$  amounts to a rigid shift of the entire grid. Since this shift is performed inside a complete summation over  $\mathbf{G}$ , the double sum can be reinterpreted as a sum over a fixed, centered  $\mathbf{k}$ -mesh, coupled to all its possible translations generated by reciprocal lattice vectors  $\mathbf{G}'$ .

This allows us to write:

$$\sum_{\mathbf{k}} e^{i\mathbf{k}\cdot\mathbf{r}} \left[ \left( \frac{\hbar^2}{2m} k^2 - \varepsilon \right) c_{\mathbf{k}} + \sum_{\mathbf{G}'} U_{\mathbf{G}'} c_{\mathbf{k}-\mathbf{G}'} \right] = 0 \quad (1.16)$$

This equation is satisfied for all  $\mathbf{r}$  only if the term inside the square brackets vanishes for each  $\mathbf{k}$ .

This implies that for each  $\mathbf{k}$ , once the Fourier coefficients of the potential are known, one obtains a system of  $N$  coupled equations with  $N + 1$  unknown: the coefficients  $c_{\mathbf{k}-\mathbf{G}'}$  and the eigenvalue  $\varepsilon_{\mathbf{k}}$ . This system admits multiple solutions, which can be labeled by an additional index  $n$ , called the band index. We can thus identify two type of quantum numbers: the *Band Index*<sup>5</sup>  $n$  and the *Crystal Momentum*  $\mathbf{k}$ , and the basis solutions of the Schrödinger<sup>6</sup> equation for an electron in a static periodic potential can be written as:

$$\psi_{n\mathbf{k}}(\mathbf{r}) = \sum_{\mathbf{G}'} c_{n,\mathbf{k}-\mathbf{G}'} e^{i(\mathbf{k}-\mathbf{G}') \cdot \mathbf{r}} = e^{i\mathbf{k} \cdot \mathbf{r}} u_{n\mathbf{k}}(\mathbf{r}), \quad (1.17a)$$

where we have introduced a function that is a superposition of plane waves with reciprocal lattice vectors, and therefore has the same periodicity as the lattice:

$$u_{n\mathbf{k}}(\mathbf{r}) = \sum_{\mathbf{G}'} c_{n,\mathbf{k}-\mathbf{G}'} e^{-i\mathbf{G}' \cdot \mathbf{r}}. \quad (1.17b)$$

### 1.1.3. Bloch Theorem and the wavefunction symmetry

The results we have derived at the end of last section is an important result often referred as **Bloch Theorem**, it is easy to show that from the properties of the solution also the equivalent result holds:

$$\psi_{n\mathbf{k}}(\mathbf{r} + \mathbf{R}) = e^{i\mathbf{k} \cdot \mathbf{R}} \psi_{n\mathbf{k}}(\mathbf{r}) \quad (1.18)$$

Where  $\mathbf{R}$  is a lattice vector. As a first fact this would mean that the observable electron density  $\rho(\mathbf{r}) = e|\psi_{n\mathbf{k}}(\mathbf{r})|^2$  is a periodic function. More importantly, this implies that the wavefunction and thus the energy eigenvalues are invariant with respect to traslation of the crystal index by reciprocal lattice vector, indeed using the first expression of the Bloch theorem one can show that:

$$\psi_{n\mathbf{k}+\mathbf{G}}(\mathbf{r}) = e^{i(\mathbf{k}+\mathbf{G}) \cdot \mathbf{r}} u_{n\mathbf{k}+\mathbf{G}}(\mathbf{r}) \quad (1.19a)$$

$$\begin{aligned} &= e^{i\mathbf{k} \cdot \mathbf{r}} e^{i\mathbf{G} \cdot \mathbf{r}} (e^{-i\mathbf{G} \cdot \mathbf{r}} u_{n\mathbf{k}}(\mathbf{r})) \\ &= e^{i\mathbf{k} \cdot \mathbf{r}} u_{n\mathbf{k}}(\mathbf{r}) = \psi_{n\mathbf{k}}(\mathbf{r}), \end{aligned} \quad (1.19b)$$

---

<sup>5</sup>The discreteness of the band index  $n$  is analogous to the energy quantization of a particle in a box. It arises from solving an eigenvalue problem in a finite volume  $V$ , where periodic boundary conditions lead to a discrete set of basis states and, consequently, to a discrete spectrum of eigenvalues.

<sup>6</sup>A wavefunction whose coefficients are nonzero only for indices differing from  $\mathbf{k}$  by reciprocal lattice vectors satisfies Eq. (1.16), complete ly equivalent to the Schrödinger equation. Such solutions can be chosen to be orthonormal with respect to both  $n$  and  $\mathbf{k}$ .

and therefore

$$\varepsilon_{n\mathbf{k}+\mathbf{G}} = \varepsilon_{n\mathbf{k}}. \quad (1.20)$$

### Brillouin Zone Edge Symmetry

In general, the equivalence of two crystal momentum vectors modulo a reciprocal lattice vector not only allows one to restrict the analysis to the first Brillouin zone (FBZ), but also has important consequences for the symmetry of states at its boundary.

In particular, crystal momenta lying on the edge of the FBZ may correspond to physically equivalent points, since they can be mapped onto each other by the addition of reciprocal lattice vectors. In limiting cases, boundary points may coincide with reciprocal lattice vectors themselves or differ from one another by a reciprocal lattice vector, implying that the corresponding Bloch states are equivalent and therefore have degenerate energies, as a direct consequence of translational symmetry.

### Point Group Symmetry

An operator  $\hat{\mathcal{R}}$  associated with any symmetry of the Hamiltonian commutes with  $\hat{H}$ ,

$$\hat{\mathcal{R}}(\hat{H}\psi) = (\hat{\mathcal{R}}\hat{H})(\hat{\mathcal{R}}\psi) = \hat{H}(\hat{\mathcal{R}}\psi). \quad (1.21)$$

As a consequence, the Hamiltonian and the symmetry operators can be simultaneously diagonalized. Moreover, when expressed in a basis adapted to the degenerate subspaces associated with the symmetry group, the Hamiltonian acquires a block-diagonal structure.

As a direct consequence of Eq. (1.21), any rotation<sup>7</sup> belonging to the point group of the crystal generates a wavefunction that is degenerate with the original one:

$$H(\hat{\mathcal{R}}\psi(\mathbf{r})) = \hat{\mathcal{R}}(H\psi(\mathbf{r})) = \varepsilon \hat{\mathcal{R}}\psi(\mathbf{r}). \quad (1.22)$$

The action of a point-group operator on a wavefunction is defined as

$$\hat{\mathcal{R}}\psi(\mathbf{r}) \equiv \psi(\hat{\mathcal{R}}^{-1}\mathbf{r}), \quad (1.23)$$

---

<sup>7</sup>The following discussion applies only to systems in which the full space group can be generated by the composition of lattice translations with point-group operations; such space groups are called *symmorphic*.

so that, when applied to a Bloch state, one obtains

$$\hat{\mathcal{R}}\psi_{n\mathbf{k}}(\mathbf{r}) = e^{i\mathbf{k}\cdot(\hat{\mathcal{R}}^{-1}\mathbf{r})}u_{n\mathbf{k}}(\hat{\mathcal{R}}^{-1}\mathbf{r}). \quad (1.24)$$

We now show that the rotated function corresponds to a Bloch state with rotated crystal momentum  $\hat{\mathcal{R}}\mathbf{k}$ . We start by noticing an important property of the scalar product, which admits a clear geometric interpretation: rotating both vectors in a scalar product in the same way leaves its value invariant,

$$\mathbf{k} \cdot (\hat{\mathcal{R}}^{-1}\mathbf{r}) = (\hat{\mathcal{R}}\mathbf{k}) \cdot (\hat{\mathcal{R}}\hat{\mathcal{R}}^{-1}\mathbf{r}) = (\hat{\mathcal{R}}\mathbf{k}) \cdot \mathbf{r}. \quad (1.25)$$

The argument for the periodic part is slightly more subtle. For a given  $\mathbf{k}$ , the function  $u_{n\mathbf{k}}(\mathbf{r})$  represents a specific lattice-periodic spatial pattern. Rotating its argument corresponds to rotating this pattern in real space. Since point-group operations map lattice vectors onto lattice vectors, the rotated function  $u_{n\mathbf{k}}(\hat{\mathcal{R}}^{-1}\mathbf{r})$  remains lattice-periodic. Moreover, because reciprocal lattice vectors are closed under the action of point-group rotations, the Fourier components of the rotated function are still labeled by reciprocal lattice vectors. As a result,  $u_{n\mathbf{k}}(\hat{\mathcal{R}}^{-1}\mathbf{r})$  can be identified, up to a phase choice, with the periodic part associated with the rotated crystal momentum,  $u_{n,\hat{\mathcal{R}}\mathbf{k}}(\mathbf{r})$ .

As a consequence, one can identify a *star* of  $\mathbf{k}$ -vectors, all connected to each other by point-group rotations, which correspond to degenerate Bloch states, reducing the number of points where quantities must be computed.

## Time Reversal Symmetry

In the scope of our case, a non-relativistic, time-independent system described by a real Hamiltonian—we consider the time-dependent Schrödinger equation:

$$i\hbar \frac{\partial \Psi}{\partial t} = H\Psi. \quad (1.26a)$$

Taking the complex conjugate, we obtain

$$i\hbar \frac{\partial \Psi^*}{\partial(-t)} = H\Psi^*. \quad (1.26b)$$

The inversion of the time variable in the second equation implies that if  $\Psi$  is a solution

describing the forward-time evolution,  $\Psi^*$  is a solution of the time-reversed problem<sup>8</sup>. More importantly, these two wavefunctions are both solutions of the time-independent Schrödinger equation and yield the same probability density; therefore, we expect them to be degenerate<sup>9</sup>.

Applied to Bloch states, the complex conjugate of a Bloch eigenstate is still a solution of Eq. 1.5, and therefore retains the Bloch form:

$$\psi_{n\mathbf{k}}^*(\mathbf{r}) = u_{n\mathbf{k}}^*(\mathbf{r})e^{-i\mathbf{k}\cdot\mathbf{r}} = u'_{n-\mathbf{k}}(\mathbf{r})e^{-i\mathbf{k}\cdot\mathbf{r}} \sim \psi_{n-\mathbf{k}}(\mathbf{r}). \quad (1.27)$$

The exponential factor shows that, in order to satisfy the Bloch condition,  $u'_{n-\mathbf{k}} \sim u_{n-\mathbf{k}}$  up to a phase.

Since  $\psi_{n\mathbf{k}}(\mathbf{r})$  and  $\psi_{n-\mathbf{k}}(\mathbf{r})$  are related by time-reversal symmetry, we consequently expect the following symmetry in the band structure:

$$\varepsilon_n(\mathbf{k}) = \varepsilon_n(-\mathbf{k}). \quad (1.28)$$

### Gauge freedom of Bloch states

Bloch eigenstates are defined up to a  $\mathbf{k}$ -dependent phase,

$$\psi_{n\mathbf{k}}(\mathbf{r}) \rightarrow e^{i\varphi_n(\mathbf{k})} \psi_{n\mathbf{k}}(\mathbf{r}), \quad (1.29)$$

which leaves the Schrödinger equation and all physical observables invariant. In particular, the electronic density  $\rho_{n\mathbf{k}}(\mathbf{r}) = e|\psi_{n\mathbf{k}}(\mathbf{r})|^2$  is unchanged under such a transformation.

If the phase  $\varphi_n(\mathbf{k})$  is periodic in reciprocal space,  $\varphi_n(\mathbf{k} + \mathbf{G}) = \varphi_n(\mathbf{k})$ , the Bloch form

$$\psi_{n\mathbf{k}}(\mathbf{r}) = e^{i\mathbf{k}\cdot\mathbf{r}} u_{n\mathbf{k}}(\mathbf{r}) \quad (1.30)$$

is preserved, since the phase can be absorbed into the lattice-periodic function  $u_{n\mathbf{k}}(\mathbf{r})$  without affecting its periodicity. This gauge freedom plays a central role in the construction of Wannier functions, where different smooth choices of  $\varphi_n(\mathbf{k})$  correspond to different, but physically equivalent, representations of the same electronic states [4], with different

<sup>8</sup>Classically, this corresponds to reversing the direction of time and, consequently, all velocities.

<sup>9</sup>If external magnetic fields or spin degrees of freedom are taken into account, the symmetry associated with time reversal becomes more subtle. In particular, if the time-reversal operation is not applied to the field sources, a particle moving with opposite velocity in a magnetic field experiences an opposite Lorentz force. Moreover, for spin-dependent wavefunctions, the construction of the time-reversal operator requires specifying its action on spin, which involves a rotation of the spin state about a transverse axis.

degrees of localization in real space. This aspect will become particularly important in Sec. 4, where this gauge freedom is exploited to transform physical observables into a low-dimensional latent space, enabling efficient compression and accurate interpolation on fine meshes in momentum space.

## 1.2. Density Functional Theory

Density Functional Theory (DFT) provides an efficient framework for addressing the complex computational problem of electrons and nuclei in materials introduced at the beginning of this chapter. To understand its efficacy, in this section we introduce the fundamental theoretical results established in the mid-1960s by Hohenberg, Kohn, and Sham. The fundamental achievement of this theory is that, to study the *Ground State* properties of a many-body system, it is sufficient to consider the electron density  $\rho(\mathbf{r})$  alone, rather than the complex wavefunction dependent on  $3N_e$  degrees of freedom.

At the same time, it is important to stress that the intent here is only to highlight the basic principles. Both the implementation and the physical insight required to achieve reliable simulations of materials in contemporary research demand specific knowledge and experience, as well as the use of complex simulation packages developed in large-scale academic projects, such as VASP and Quantum ESPRESSO. Details regarding the calculations for two benchmark materials, Silicon (Si) and Lithium Fluoride (LiF), can be found in Appendix A.

A first observation is that in the limit of a static lattice, and effectively within the more realistic Born-Oppenheimer approximation (see next chapter), the many-body wavefunction depends on the nuclear positions only parametrically. Consequently, in many treatments, the electron-nuclei interaction can be viewed as an external electrostatic potential that does not couple different electron degrees of freedom:

$$\hat{V}_{ext}(\mathbf{r}_1, \dots, \mathbf{r}_{N_e}) = \sum_{i=1}^{N_e} v_{ext}(\mathbf{r}_i) = - \sum_{i=1}^{N_e} \sum_{a=1}^{N_{at}} \frac{Z_a e^2}{|\mathbf{r}_i - \mathbf{R}_a|} \quad (1.31)$$

In this framework, the nuclei-nuclei interaction is treated as a constant additive term with respect to the electronic structure[5].

### 1.2.1. Hartree-Fock Ansatz

Before diving into the core of Density Functional Theory, we first formulate a variational treatment of the many-body Hamiltonian. This is useful to identify the different physical contributions to the total energy.

In general, the energy of a state  $\Psi$  is a functional:

$$E[\Psi] = \int d\mathbf{r} \Psi^* \hat{H} \Psi \geq E_{GS} \quad (1.32)$$

where the inequality ensures  $E[\Psi]$  is an upper bound to the ground state energy  $E_{GS}$ , known as the *Variational Theorem*.

The energy functional must in principle be minimized over the whole electron Hilbert Space. A powerful Ansatz capable of including the antisymmetric requirements (Pauli exclusion principle) is the *Slater determinant*. Given an orthonormal basis set of single-particle trial wavefunctions  $\{\phi_i\}$ :

$$\Psi_{HF}(\mathbf{r}_1, \dots, \mathbf{r}_N) = \frac{1}{\sqrt{N!}} \begin{vmatrix} \phi_1(\mathbf{r}_1) & \phi_2(\mathbf{r}_1) & \cdots & \phi_N(\mathbf{r}_1) \\ \phi_1(\mathbf{r}_2) & \phi_2(\mathbf{r}_2) & \cdots & \phi_N(\mathbf{r}_2) \\ \vdots & \vdots & \ddots & \vdots \\ \phi_1(\mathbf{r}_N) & \phi_2(\mathbf{r}_N) & \cdots & \phi_N(\mathbf{r}_N) \end{vmatrix} \quad (1.33)$$

Substituting this into the Hamiltonian, the Energy functional becomes:

$$E_{HF}[\{\phi_i\}] = T_s[\{\phi_i\}] + V_{ext}[\{\phi_i\}] + V_H[\{\phi_i\}] + V_x[\{\phi_i\}] \quad (1.34)$$

The first two terms correspond to the kinetic energy and external potential. The third term is the *Hartree* contribution:

$$V_H = \frac{1}{2} \sum_{i,j}^N \iint \frac{|\phi_i(\mathbf{r}_1)|^2 |\phi_j(\mathbf{r}_2)|^2}{|\mathbf{r}_1 - \mathbf{r}_2|} d\mathbf{r}_1 d\mathbf{r}_2 \quad (1.35)$$

This represents the *classical mean-field* Coulomb interaction: an electron moves in the electrostatic potential generated by the charge density of all electrons, including itself<sup>10</sup>.

---

<sup>10</sup>The Hartree potential corresponds to a classical charge distribution. It incorrectly includes a "self-interaction" of the electron with itself. In the full Hartree-Fock scheme, this spurious self-interaction is exactly cancelled by the diagonal terms of the Exchange potential.

The fourth term is the *Fock* or *Exchange* contribution:

$$V_x = -\frac{1}{2} \sum_{i,j}^N \iint \frac{\phi_i^*(\mathbf{r}_1)\phi_j(\mathbf{r}_1)\phi_i(\mathbf{r}_2)\phi_j^*(\mathbf{r}_2)}{|\mathbf{r}_1 - \mathbf{r}_2|} d\mathbf{r}_1 d\mathbf{r}_2 \quad (1.36)$$

This is a purely quantum-mechanical effect arising from the antisymmetric nature of the wavefunction.

Minimizing this energy leads to the Hartree-Fock equations:

$$\left[ -\frac{1}{2}\nabla^2 + v_{ext}(\mathbf{r}) + \int \frac{\rho(\mathbf{r}')}{|\mathbf{r} - \mathbf{r}'|} d\mathbf{r}' \right] \phi_i(\mathbf{r}) + \int v_x(\mathbf{r}, \mathbf{r}') \phi_i(\mathbf{r}') d\mathbf{r}' = \epsilon_i \phi_i(\mathbf{r}) \quad (1.37)$$

Where  $\int v_x(\mathbf{r}, \mathbf{r}') \phi_i(\mathbf{r}') d\mathbf{r}' = - \sum_{j=1}^N \int \frac{\phi_j(\mathbf{r})\phi_j^*(\mathbf{r}')}{|\mathbf{r}-\mathbf{r}'|} \phi_i(\mathbf{r}') d\mathbf{r}'$ .

Solving these equations yields the Hartree-Fock energy  $E_{HF}$ . The missing energy difference with respect to the exact solution is defined as the *Correlation Energy*:  $E_c = E_{GS} - E_{HF} \leq 0$ . This term arises because, in reality, electron motions are not independent as assumed in the mean-field Hartree-Fock treatment; instead, the motion of each electron is *dynamically correlated* with the instantaneous positions of all others to avoid Coulomb repulsion. The correction is naturally negative because this dynamical avoidance stabilizes the system, allowing it to relax into a lower energy state than the static mean-field approximation permits. This is a computationally demanding problem, primarily because the exact treatment of the *non-local* exchange term requires evaluating expensive integrals over all pairs of electrons.

### 1.2.2. Hohenberg-Kohn Theorems

The Hartree-Fock method demonstrated that a mean-field variational approach can capture essential physics, yet the complexity of the  $3N$ -dimensional many-body wavefunction  $\Psi$  remains a formidable barrier for realistic materials. The foundational breakthrough of Density Functional Theory (DFT) lies in the rigorous proof that the wavefunction is, in a certain way, redundant for determining ground-state properties. Hohenberg and Kohn established two theorems that recast the many-body problem entirely in terms of the electron density  $\rho(\mathbf{r})$ .

The **First Theorem** proves that for a system of interacting electrons in an external potential  $V_{ext}(\mathbf{r})$ , the ground-state density  $\rho(\mathbf{r})$  uniquely determines  $V_{ext}(\mathbf{r})$ . Since the Hamiltonian is fully specified by  $V_{ext}$  and the total electron number  $N = \int \rho(\mathbf{r}) d\mathbf{r}$ , it fol-

lows that the ground-state density uniquely determines the full many-body wavefunction and all ground-state observables.

The **Second Theorem** establishes a variational principle for the density. It defines a universal functional  $F[\rho]$ , independent of the external potential, that contains the kinetic and interaction energies. The total energy functional is:

$$E[\rho] = \int V_{ext}(\mathbf{r})\rho(\mathbf{r})d\mathbf{r} + F[\rho] \geq E_0 \quad (1.38)$$

Minimizing this functional with respect to  $\rho(\mathbf{r})$  (under the constraint of particle conservation) yields the exact ground-state energy  $E_0$  and density. This formally reduces the problem from  $3N$  spatial coordinates to just the 3 spatial variables of the density.

### 1.2.3. Kohn-Sham Equations

While the Hohenberg-Kohn theorems guarantee the existence of the functional  $E[\rho]$ , they do not provide its explicit form, particularly for the interacting kinetic energy and the complex electron-electron correlations. To make DFT practical, Kohn and Sham introduced a crucial ansatz: they replaced the real interacting system with an *auxiliary system* of non-interacting fermions that generates the exact same ground-state density as the real system.

It is important to stress that the single-particle wavefunctions in this scheme, known as **Kohn-Sham orbitals**  $\phi_i(\mathbf{r})$ , are mathematical constructs (to have a "single fictitious particle" problem) and do not correspond to the real electron wavefunctions. Their primary purpose is to construct the exact density:

$$\rho(\mathbf{r}) = \sum_{i=1}^N |\phi_i(\mathbf{r})|^2 \quad (1.39)$$

By separating the known contributions of this non-interacting reference system from the total energy, we can rewrite the energy functional as:

$$E_{KS}[\rho] = T_s[\{\phi_i\}] + E_H[\rho] + \int V_{ext}(\mathbf{r})\rho(\mathbf{r})d\mathbf{r} + E_{xc}[\rho] \quad (1.40)$$

Here,  $T_s = -\frac{1}{2} \sum_i \langle \phi_i | \nabla^2 | \phi_i \rangle$  is the exact kinetic energy of the non-interacting system, and  $E_H$  is the Hartree mean-field energy introduced previously. The last term, the **Exchange-Correlation energy**  $E_{xc}[\rho]$ , is defined as the contribution for all the "missing" many-body effects: the difference between the true and non-interacting kinetic energy, and the

non-classical electron-electron interactions (exchange and dynamic correlation).

Minimizing this energy with respect to the orbitals  $\phi_i^*$  leads to the Schrödinger-like **Kohn-Sham equations**:

$$H_{KS}(\mathbf{r})\phi_i(\mathbf{r}) = \left[ -\frac{1}{2}\nabla^2 + V_{eff}(\mathbf{r}) \right] \phi_i(\mathbf{r}) = \epsilon_i \phi_i(\mathbf{r}) \quad (1.41)$$

where the effective potential is given by  $V_{eff}(\mathbf{r}) = V_{ext}(\mathbf{r}) + \int \frac{\rho(\mathbf{r}')}{|\mathbf{r}-\mathbf{r}'|} d\mathbf{r}' + v_{xc}(\mathbf{r})$ . The exchange-correlation potential is defined as the functional derivative  $v_{xc}(\mathbf{r}) = \frac{\delta E_{xc}}{\delta \rho(\mathbf{r})}$ . Unlike the Hartree-Fock exchange potential, which is non-local,  $v_{xc}$  is a local multiplicative operator, significantly simplifying the computational effort while in principle including correlation effects.

However, since the effective potential  $V_{eff}[\rho]$  depends on the electron density, which in turn is constructed from the solutions of the equation itself, the problem is non-linear. Therefore, the Kohn-Sham equations must be solved self-consistently. This iterative procedure, commonly known as the Self-Consistent Field (SCF) cycle (fig:1.2), involves starting with a trial density, solving the eigenvalue problem to obtain new orbitals, and constructing a new density and effective potential until the results converge to a stable ground state.

Since the external potential  $V_{ext}(\mathbf{r})$  for a crystal is periodic, the total effective potential  $V_{eff}(\mathbf{r})$  shares the full periodicity and symmetry of the lattice. This allows us to invoke the **Bloch Theorem** derived in the previous section. The Kohn-Sham orbitals can thus be expanded in a Bloch basis indexed by the band index  $n$  and crystal momentum  $\mathbf{k}$ :

$$\phi_{n\mathbf{k}}(\mathbf{r}) = e^{i\mathbf{k}\cdot\mathbf{r}} u_{n\mathbf{k}}(\mathbf{r}) \quad (1.42)$$

In plane-wave-based implementations of DFT, the accuracy of the results is controlled by the choice of the energy cutoff  $E_{cut}$ , which determines the maximum kinetic energy of the plane waves used to expand the Kohn-Sham orbitals. Increasing  $E_{cut}$  systematically improves the description of the electronic wavefunctions and total energy, at the expense of higher computational cost; therefore, convergence with respect to this parameter must be carefully verified together with the Brillouin Zone sampling.

A more fundamental approximation arises from the unknown exact form of the exchange-correlation functional  $E_{xc}[\rho]$ . The Local Density Approximation (LDA) assumes  $E_{xc}$  depends only on the local electron density  $\rho(\mathbf{r})$ , while the Generalized Gradient Approximation (GGA) improves upon this by including a dependence on the density gradient  $\nabla\rho(\mathbf{r})$ . Hybrid functionals further incorporate a fraction of exact exchange, partially restoring

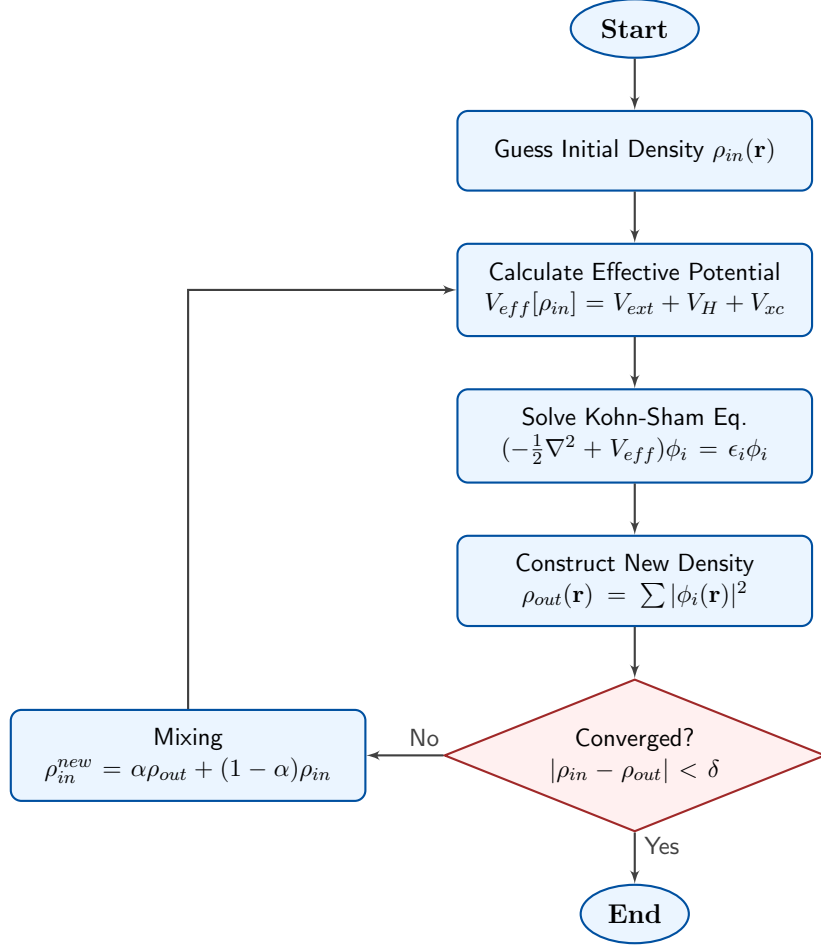


**Figure 1.2:** Schematic representation of the Self-Consistent Field (SCF) cycle in Density Functional Theory.

the non-local character of the interaction.

While LDA and GGA are generally reliable for structural and energetic properties, they systematically underestimate the band gaps of semiconductors and insulators. Nevertheless, they typically reproduce the qualitative features of the electronic band structure and remain widely used due to their favorable balance between accuracy and computational cost.

As benchmark systems throughout this work, we consider two prototypical materials crystallizing in the fcc structure: elemental silicon (Si), a covalent semiconductor, and lithium fluoride (LiF), a wide-gap ionic insulator. These two systems are characterized by markedly different electronic structures, spanning from a relatively small-gap semiconductor to a strongly insulating material.

The purpose of this choice is not to focus on material-specific physical mechanisms, but

rather to assess the generality and robustness of the tensor-based low-rank factorization strategy introduced in this thesis. In particular, we will show that a compact low-rank representation of the electron–phonon matrix elements can be achieved in both cases, despite their very different electronic spectra, and electron-phonon coupling.

Representative electronic band structures computed within density functional theory using VASP are shown in Fig. 1.3.

922

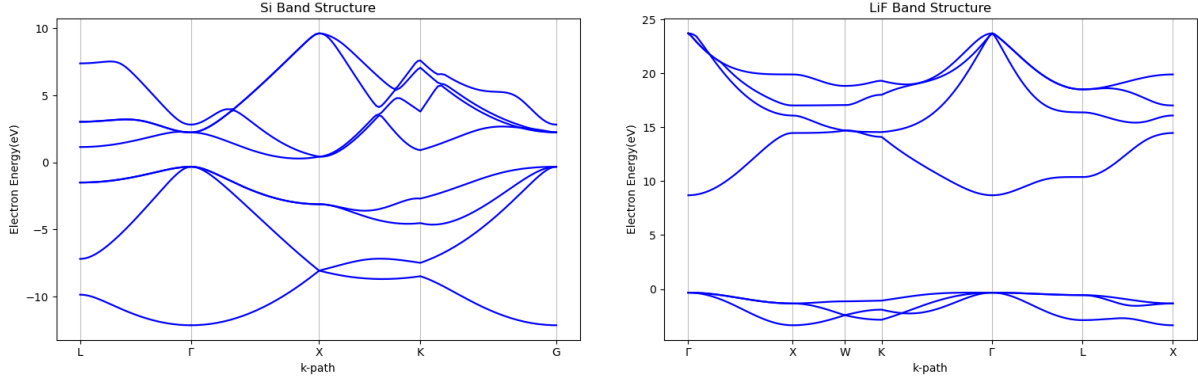


Figure 1.3: Electronic band structures of the two benchmark materials considered in this thesis, computed within density functional theory using VASP along standard high-symmetry paths of the fcc Brillouin zone. For Si (left), the four top valence bands and five conduction bands are shown. For LiF (right), the three top valence bands and four conduction bands are reported, with the valence manifold well separated from deeper bands.

### 1.3. Second Quantization

In Quantum Mechanics, particles are defined by a set of irreducible operators corresponding to physical observables (Momentum, Position, Spin, etc.) and their commutation relations. A fundamental distinction exists between classical and quantum mechanics regards *indistinguishability*[6, 7].

While classical particles can be individually tracked, identical quantum particles are indistinguishable. This physical reality imposes a symmetry constraint on the *Quantum Many-Body Wavefunction*: the probability density must be invariant with respect to the permutation of particle labels. Consequently, the wavefunction itself must be either symmetric or antisymmetric under such permutations.

The Slater Determinant (Eq. 1.33) is a specific example of an antisymmetric state constructed from single-particle orbitals. More generally, we can define a permutation operator  $\hat{P}_\sigma$  acting on a generic many-body state:

$$\hat{P}_\sigma |u_1, \dots, u_N\rangle \equiv |u_{\sigma_1}, \dots, u_{\sigma_N}\rangle \quad (1.43)$$

where  $\sigma = (\sigma_1, \dots, \sigma_N)$  represents a permutation of the indices. Due to indistinguishabil-

ity, the state must satisfy:

$$\hat{P}_\sigma |u_1, \dots, u_N\rangle = (\pm 1)^{|\sigma|} |u_1, \dots, u_N\rangle \quad (1.44)$$

Here,  $|\sigma|$  denotes the parity of the permutation. The (+) sign holds for *Bosons* (integer spin), which possess a symmetric wavefunction. The (−) sign holds for *Fermions* (half-integer spin), which possess an antisymmetric wavefunction. For fermions, this antisymmetry leads directly to the *Pauli Exclusion Principle*.

We have introduced the **Dirac Notation** above. The *Ket*  $|u\rangle$  represents a vector in the Hilbert space  $\mathcal{H}$ , characterized by a set of quantum numbers (denoted here by  $u$ ). The *Bra*  $\langle u|$  represents the corresponding vector in the dual space  $\mathcal{H}^\dagger$ .<sup>11</sup>

Indistinguishability implies that physical observables must also respect this symmetry. Any physically measurable operator  $\hat{O}$  must commute with the permutation operator:

$$[\hat{O}, \hat{P}_\sigma] = 0 \quad (1.45)$$

### 1.3.1. Creation and Annihilation Operators

Second Quantization is a fundamental formalism for describing indistinguishable particles. In this framework, all operators corresponding to physical observables are expressed in a basis of *creation* and *annihilation* (or destruction) operators. These operators act on a many-particle state by adding or removing a particle in a specific quantum state  $|u\rangle$ , while explicitly maintaining the required symmetric or antisymmetric nature of the wavefunction.

This symmetry requirement is encoded in the fundamental algebraic relations the operators must satisfy. For **Bosons** (integer spin, symmetric states), the operators obey *Canonical Commutation Relations* (CCR):

$$[\hat{b}_i, \hat{b}_j^\dagger] = \delta_{ij}, \quad [\hat{b}_i, \hat{b}_j] = 0, \quad [\hat{b}_i^\dagger, \hat{b}_j^\dagger] = 0 \quad (1.46)$$

where  $[A, B] = AB - BA$ .

For **Fermions** (half-integer spin, antisymmetric states), the operators obey *Canonical*

---

<sup>11</sup>For instance, in a crystalline solid, Bloch states are Kets  $|n\mathbf{k}\rangle$  defined by a band index  $n$  and crystal momentum  $\mathbf{k}$ . Projecting them onto the continuous position basis yields the familiar wavefunction from first quantization:  $\psi_{n\mathbf{k}}(\mathbf{r}) = \langle \mathbf{r}|n\mathbf{k}\rangle$ .

*Anti-commutation Relations* (CAR):

$$\{\hat{c}_i, \hat{c}_j^\dagger\} = \delta_{ij}, \quad \{\hat{c}_i, \hat{c}_j\} = 0, \quad \{\hat{c}_i^\dagger, \hat{c}_j^\dagger\} = 0 \quad (1.47)$$

where  $\{A, B\} = AB + BA$ . These relations are physically significant; for instance, the relation  $\{\hat{c}_i^\dagger, \hat{c}_i^\dagger\} = 2(\hat{c}_i^\dagger)^2 = 0$  is a mathematical statement of the Pauli Exclusion Principle, two fermions cannot be created in the same state.

Second quantization is powerful because it allows us to define canonical transformations that diagonalize complex Hamiltonians, often giving rise to new collective excitations (quasiparticles). The statistics of these new quasiparticles are determined entirely by whether their operators obey CCR or CAR. Furthermore, this formalism is essential for systems where particle number is not conserved, such as in electron-phonon scattering, which can be viewed as a process where an electron emits (creates) or absorbs (annihilates) a phonon while conserving total momentum.

In this framework, the wavefunction is a vector in *Fock Space*, defined as the direct sum of Hilbert spaces for all possible particle numbers. States are most conveniently labeled by *Occupation Numbers*. Given a discrete basis set  $\{|u_i\rangle\}$ , a state is defined by the set of integers  $\{n_i\}$  representing the number of particles in each state  $i$ . We define the *occupation number operator* as:

$$\hat{n}_i = \hat{c}_i^\dagger \hat{c}_i \quad (1.48)$$

The creation operator  $\hat{c}_i^\dagger$  increases the eigenvalue of  $\hat{n}_i$  by one, while the annihilation operator  $\hat{c}_i$  decreases it by one (annihilating the state if  $n_i = 0$ ).

### 1.3.2. Operators in Second Quantization

Physical observables in many-body quantum mechanics can be naturally classified according to the number of particles they act upon. In first quantization, one usually deal with *one-particle operators*, which act independently on each particle, and *two-particle operators*, which describe interactions between pairs of particles. Typical examples are the total momentum or density operator in the former case, and the Coulomb interaction in the latter.

In the framework of second quantization, this distinction is preserved, but operators are expressed in terms of fermionic creation and annihilation operators acting on a chosen single-particle basis, a rigorous derivation can be found in [7][6].

**One-particle operators.** A generic one-particle operator  $\hat{A}^{(1)}$ , corresponding in first quantization to a sum over particles,  $\hat{A}^{(1)} = \sum_{i=1}^N \hat{a}(i)$ , can be written in second quantization as

$$\hat{A}^{(1)} = \sum_{i,j} \langle i | \hat{a} | j \rangle \hat{c}_i^\dagger \hat{c}_j, \quad (1.49)$$

where  $\{|i\rangle\}$  denotes an orthonormal single-particle basis and  $\langle i | \hat{a} | j \rangle$  are the corresponding matrix elements of the single-particle operator.

**Two-particle operators.** Similarly, a two-particle interaction operator, which in first quantization takes the form  $\hat{V}^{(2)} = \sum_{i < j} \hat{v}(i, j)$ , is represented in second quantization as

$$\hat{V}^{(2)} = \frac{1}{2} \sum_{i,j,k,l} \langle i, j | \hat{v} | k, l \rangle \hat{c}_i^\dagger \hat{c}_j^\dagger \hat{c}_l \hat{c}_k. \quad (1.50)$$

The prefactor 1/2 avoids double counting of particle pairs and ensures the correct normalization of the interaction term.

This formalism provides a compact and systematic representation of many-body operators, which will be particularly convenient when dealing with interacting systems and diagrammatic expansions in the following sections.

### 1.3.3. Non-Interacting Electronic Hamiltonian in Second Quantization

In the previous chapter, we introduced the Bloch states  $|\psi_{n\mathbf{k}}\rangle$ , which are the eigenstates of the single-particle Hamiltonian in the periodic lattice, characterized by a band index  $n$  and crystal momentum  $\mathbf{k}$ . These states form a complete orthonormal basis set and diagonalize the non-interacting part of the electronic problem.

Therefore, utilizing the general form for 1-particle operators derived above, we can express the electronic Hamiltonian (kinetic energy plus ionic potential) directly in terms of the pre-calculated dispersion relation  $\varepsilon_{n\mathbf{k}}$ :

$$\hat{H}_0 = \sum_{n,\mathbf{k}} \varepsilon_{n\mathbf{k}} \hat{c}_{n\mathbf{k}}^\dagger \hat{c}_{n\mathbf{k}} \quad (1.51)$$

where:

- $\hat{c}_{n\mathbf{k}}^\dagger$  creates a Bloch electron in band  $n$  with wavevector  $\mathbf{k}$ .

- $\hat{c}_{n\mathbf{k}}$  annihilates the corresponding electron.
- $\varepsilon_{n\mathbf{k}}$  are the eigenvalues describing the band structure.

This diagonal form is extremely convenient as it essentially counts the energy contribution of each occupied Bloch mode. In the following, this term will be referred to as the *non-interacting* (or *single-particle*) electronic Hamiltonian. Although the band energies  $\varepsilon_{n\mathbf{k}}$  already include the effect of the periodic ionic potential at the mean-field level, the Hamiltonian is diagonal in the Bloch basis and plays the role of the unperturbed reference system. Indeed, it serves as the starting point for adding perturbations, such as electron-phonon interactions, where the scattering matrix elements will describe transitions between these Bloch states  $|n\mathbf{k}\rangle$  and  $|m\mathbf{k}'\rangle$ .



# 2 | Phonons

## 2.1. Lattice Vibrations

Overcoming the static lattice picture is fundamental in order to account for many properties of real matter, both at equilibrium and out of equilibrium, such as transport phenomena and the response to external fields. This is particularly important when dealing with temperature-dependent properties, for instance the specific heat, band-gap renormalization, and electrical conductivity.

In principle, this is not an easy task, since in the many-body Hamiltonian the ionic degrees of freedom are intrinsically coupled to the electronic ones. Nonetheless, in most cases one can rely on two main sources of approximation, namely the Born–Oppenheimer approximation and the harmonic approximation. These approximations make the problem tractable and, most importantly, allow one to employ results that remain valid within the static lattice framework [2, 8].

As in the previous chapter, the goal of this section is twofold: on the one hand, to introduce the physical aspects of lattice vibrations, and on the other hand, to clearly identify the mathematical objects that will be central to the transformations introduced in Chapter 4.

### 2.1.1. Born–Oppenheimer Approximation

This powerful approximation, which takes the name of the two physicists who first introduced it, stems from the fundamental observation that the typical electronic velocities in a solid are several orders of magnitude larger than the ionic ones. As a consequence, electrons can be considered as moving in a slowly varying external potential

$$V_{\text{ext}}(\mathbf{r}; \{\mathbf{R}_I\}),$$

generated by the ions.

According to the adiabatic theorem, since the variation of this potential is continuous and occurs on a much longer time scale than the electronic one, the two degrees of freedom

can be treated as effectively independent. The electronic wavefunction

$$\psi(\mathbf{r}_1, \dots, \mathbf{r}_{N_e})$$

is then taken to be an eigenstate of the electronic Hamiltonian corresponding to the instantaneous ionic configuration, and it continuously adapts to it:

$$H(\{\mathbf{R}_I\}) \psi_n = E_n(\{\mathbf{R}_I\}) \psi_n. \quad (2.1)$$

At the same time, the eigenvalues of the electronic problem define an effective potential energy surface for the ionic motion, given by

$$U_{\text{BO}}(\{\mathbf{R}_I\}) = E_0(\{\mathbf{R}_I\}) + V_{\text{Ion-Ion}}(\{\mathbf{R}_I\}). \quad (2.2)$$

In practice, this potential energy surface is either obtained from first-principles electronic structure calculations, such as density functional theory, or approximated by empirical interatomic potentials. This framework also underlies DFT calculations, where within the self-consistent loop a fixed ionic configuration is considered, the corresponding electronic problem is solved, and the ionic positions are subsequently updated.

### 2.1.2. Harmonic Approximation

If we assume that the atoms are arranged in bases attached to different Bravais lattice sites, their equilibrium positions are fully determined by a lattice vector identifying a particular primitive cell,  $\mathbf{R}_l$ , and a basis vector,  $\tau_k$ . The underlying assumption is that lattice vibrations are, in general, small and centered around the lattice sites, which correspond to the equilibrium positions of the Born–Oppenheimer potential  $U_{\text{BO}}$ , where no net force acts on the ions:

$$F_{kl\alpha} = -\frac{\partial U_{\text{BO}}}{\partial u_{kl\alpha}} = 0. \quad (2.3)$$

Here  $\alpha$  denotes a Cartesian direction, and  $u_{kl\alpha}$  represents the displacement of the ion in cell  $l$  and basis position  $k$  along the  $\alpha$  direction, fully characterizing its motion.

Under this assumption, one can perform a Taylor expansion of the potential energy around the equilibrium configuration and truncate it at second order, while higher-order terms

are usually referred to as *anharmonic effects*:

$$U_{\text{BO}} = U_0 + \sum_{kl\alpha} \frac{\partial U_{\text{BO}}}{\partial u_{kl\alpha}} \Big|_0 u_{kl\alpha} + \frac{1}{2} \sum_{kl\alpha, k'l'\beta} \frac{\partial^2 U_{\text{BO}}}{\partial u_{kl\alpha} \partial u_{k'l'\beta}} \Big|_0 u_{kl\alpha} u_{k'l'\beta} + o(u^3) \quad (2.4)$$

Since the system is in equilibrium, the first-order term vanishes, and the second-order contribution provides the leading term in the potential energy.

The Hessian matrix of the potential energy is known as the *interatomic force constant* (IFC) tensor,

$$\Phi_{kl\alpha, k'l'\beta} = \frac{\partial^2 U_{\text{BO}}}{\partial u_{kl\alpha} \partial u_{k'l'\beta}} \Big|_0 = - \frac{\partial F_{kl\alpha}}{\partial u_{k'l'\beta}} \Big|_0, \quad (2.5)$$

and can be regarded as a generalization of the elastic spring constant to three dimensions, describing the coupling between the displacements of different atoms.<sup>1</sup>

Due to the translational invariance of the crystal lattice, the IFCs do not depend on the absolute positions of the atoms, but only on their relative separation. It is therefore convenient to express them as functions of the relative lattice vector

$$\mathbf{R} = \mathbf{R}_{l'} - \mathbf{R}_l,$$

and write

$$\Phi_{kl\alpha, k'l'\beta} \equiv \Phi_{kk'\alpha\beta}(\mathbf{R}). \quad (2.7)$$

This representation automatically reflects the invariance of the IFC matrix under discrete translations along primitive lattice vectors.

Moreover, from the symmetry of mixed second derivatives of the potential energy, the IFC tensor, if the displacements of the two atoms are exchanged, satisfying the relation:

$$\Phi_{kk'\alpha\beta}(\mathbf{R}) = \Phi_{k'k\beta\alpha}(-\mathbf{R}). \quad (2.8)$$

---

<sup>1</sup>This do not apply to self interaction contribution. A practical consequence of the Acoustic Sum Rule (see later) is that the on-site, or self-interaction, terms of the IFC matrix are not independent. They can be obtained as the negative sum of all force constants coupling a given atom to the rest of the lattice:

$$\Phi_{lk\alpha, lk\beta} = - \sum_{(l'k') \neq (lk)} \Phi_{lk\alpha, l'k'\beta}. \quad (2.6)$$

### 2.1.3. Dynamical Matrix

Within this framework, one can write down the classical equation of motion for an ion.<sup>2</sup> This results in a system of coupled differential equations:

$$M_k \ddot{u}_{kl\alpha} = F_{kl\alpha} = -\frac{\partial U_{\text{BO}}}{\partial u_{kl\alpha}} \simeq -\sum_{k'l'\beta} \Phi_{kl\alpha, k'l'\beta} u_{k'l'\beta}. \quad (2.9)$$

Given the periodicity of the lattice and of the interatomic force constants, one can look for *polarized* plane-wave solutions:

$$u_{kl\alpha}(\mathbf{q}, t) = \frac{1}{\sqrt{M_k}} e^{i(\mathbf{q} \cdot \mathbf{R}_l - \omega t)} e_{k\alpha}(\mathbf{q}). \quad (2.10a)$$

Substituting this Ansatz into the equations of motion leads to an eigenvalue problem:

$$\sum_{k'\beta} D_{k\alpha, k'\beta}(\mathbf{q}) e_{k'\beta, \nu}(\mathbf{q}) = \omega_\nu^2(\mathbf{q}) e_{k\alpha, \nu}(\mathbf{q}), \quad (2.10b)$$

where the dynamical matrix is defined as the mass-weighted Fourier transform of the interatomic force constants,

$$D_{kk'\alpha\beta}(\mathbf{q}) = \frac{1}{\sqrt{M_k M_{k'}}} \sum_{\mathbf{R}} \Phi_{kk'\alpha\beta}(\mathbf{R}) e^{i\mathbf{q} \cdot \mathbf{R}}. \quad (2.10c)$$

From the form of the solutions, one sees that once the eigenvectors  $\mathbf{e}_{k\nu}(\mathbf{q})$  are determined, they can be inserted into the plane-wave expression to construct collective displacement patterns characterized by a well-defined wavelength and polarization. These normal modes can be quantized and correspond to collective excitation of the crystal lattice, resulting in quasiparticles known as *phonons*, each identified by a branch index  $\nu$  and a phonon wavevector  $\mathbf{q}$ , which uniquely determine the corresponding frequency  $\omega_\nu(\mathbf{q})$  appearing in the phonon dispersion relation.

The eigenvectors are generally complex and are conventionally chosen to satisfy orthonormality relations. In particular, they are orthonormal with respect to different branch

---

<sup>2</sup>This is motivated by the fact that, from the uncertainty principle  $\Delta r \sim \hbar/(Mv_I)$ , for a typical silicon ion at 300 K (where  $v_I \approx 500$  m/s) one obtains  $\Delta r \approx 0.03$  Å. This value is about two orders of magnitude smaller than a typical interatomic distance ( $\sim 2\text{--}3$  Å), thus justifying a classical treatment of the ionic motion.

indices,

$$\sum_k^{N_I} \mathbf{e}_{k\nu}^* \cdot \mathbf{e}_{k\nu'} = \sum_k^{N_I} \sum_{\alpha}^3 e_{\alpha k\nu}^* e_{\alpha k\nu'} = \delta_{\nu\nu'}, \quad (2.11a)$$

and complete with respect to the atomic indices,

$$\sum_{\nu}^{3N_I} e_{\alpha k\nu}^* e_{\beta k'\nu} = \delta_{kk'} \delta_{\alpha\beta}. \quad (2.11b)$$

The Born–von Kármán boundary conditions introduce a quantization of the allowed wavevectors, as discussed in Eq. (1.12a), and in general eigenvectors corresponding to different wavevectors are not orthogonal. For each  $\mathbf{q}$  there are  $3N_I$  normal modes, three of which are referred to as *acoustic* modes and correspond to collective in-phase motion of the atoms. Their name reflects the fact that, in the vicinity of the  $\Gamma$  point, their dispersion relation is linear, as for sound waves, and they are therefore responsible for sound propagation in solids. The remaining modes, which exist only in crystals with more than one atom in the basis, correspond to out-of-phase atomic motion and retain a finite frequency even in the long-wavelength limit. In polar materials, such modes can induce a macroscopic polarization and thus couple to electromagnetic fields.

Phonons also play a central role in the thermal properties of solids. Historically, the prediction of low-energy collective excitations within the Debye model represented a major breakthrough in the understanding of realistic temperature-dependent behavior and laid the foundations for the microscopic theory of conventional superconductivity within the Bardeen–Cooper–Schrieffer framework. At the same time, in materials where ions carry a net charge, the interaction between electrons and lattice vibrations can give rise to another important quasiparticle, the *polaron*. This consists of an electron or a hole dressed by a surrounding cloud of phonons, which may extend over long or short length scales and plays a key role in several physical phenomena.

#### 2.1.4. Symmetries

From the definition of the displacement modes in Eq. 2.10a, we can directly see how phonons transform under symmetry operations. Translations leave the system invariant, essentially introducing only a different initial phase.

For point-group operations, instead, we can explicitly examine how they act on a given

displacement:

$$\hat{\mathcal{R}} u_{kl\alpha}(\mathbf{q}, t) = \frac{1}{\sqrt{M_k}} e^{i(\mathbf{q} \cdot \hat{\mathcal{R}}^{-1} \mathbf{R}_l - \omega t)} \hat{\mathcal{R}} e_{k\alpha}(\mathbf{q}) = \frac{1}{\sqrt{M_k}} e^{i(\hat{\mathcal{R}} \mathbf{q} \cdot \mathbf{R}_l - \omega t)} e_{k\alpha}(\hat{\mathcal{R}} \mathbf{q}) = u_{kl\alpha}(\hat{\mathcal{R}} \mathbf{q}, t).$$

Here we used the invariance of the scalar product under rotations, as in Eq. 1.25. Since the spatial modulation corresponds to a rotated wavevector, consistency of the displacement field implies that the polarization vectors transform accordingly,

$$\hat{\mathcal{R}} e_{k\alpha}(\mathbf{q}) = e_{k\alpha}(\hat{\mathcal{R}} \mathbf{q}),$$

up to possible phase factors or linear combinations in the presence of degeneracies.

As for electrons, from the commutation relation in Eq. 1.21, here applied to the ionic Hamiltonian, we know that phonon modes related by point-group operations must have the same frequency.<sup>3</sup> Therefore,

$$\omega_\nu(\mathbf{q}) = \omega_\nu(\hat{\mathcal{R}} \mathbf{q}). \quad (2.12)$$

As a consequence, also in the phonon case it is possible to introduce the *star of wavevectors*, allowing one to restrict calculations to the irreducible part of the Brillouin zone. Moreover, phonon frequencies are periodic with respect to reciprocal lattice vectors, as follows from the periodicity of the dynamical matrix, which is easy to verify. However, unlike the electronic case, this periodicity does not generally extend to the polarization vectors.

In addition to spatial symmetries, phonon modes also obey time-reversal symmetry. Since lattice dynamics is governed by real equations of motion derived from a real Born–Oppenheimer potential, the analysis presented above for electrons can be directly extended to phonons. In particular, a phonon mode with wavevector  $\mathbf{q}$  and frequency  $\omega_\nu(\mathbf{q})$  has a time-reversed counterpart at  $-\mathbf{q}$  with the same frequency. This implies the symmetry

$$\omega_\nu(\mathbf{q}) = \omega_\nu(-\mathbf{q}), \quad (2.13)$$

which holds in the absence of magnetic fields or other sources of time-reversal symmetry breaking. As in the electronic case, this symmetry further reduces the number of inequivalent wavevectors that must be considered.

---

<sup>3</sup>In the presence of degeneracies,  $\omega_\nu(\mathbf{q}) = \omega_{\nu'}(\mathbf{q})$ , the corresponding eigenmodes may transform into linear combinations of each other.

### 2.1.5. Acoustic Sum Rule

A direct consequence of the character of phonon modes is the so-called *acoustic sum rule* (ASR). In the long-wavelength limit  $\mathbf{q} \rightarrow 0$ , the acoustic phonon modes correspond to rigid translations of the entire crystal. Since a uniform translation does not change the total energy of the system, the corresponding phonon frequencies must vanish, as already observed.

By contrast, optical modes at  $\mathbf{q} \rightarrow 0$  describe internal vibrations of the basis atoms within the unit cell, characterized by out-of-phase motion of the atoms. In this limit, the center of mass of each unit cell remains fixed, implying that the mass-weighted sum of atomic displacements vanishes. Expressed in terms of the phonon eigenvectors, this condition reads

$$\sum_k \sqrt{M_k} \mathbf{e}_{k\nu}(\mathbf{q} = 0) = 0, \quad \nu > 3. \quad (2.14)$$

The acoustic sum rule can be formulated directly in terms of the dynamical matrix or, equivalently, of the interatomic force constants. Previous conditions requires that the total force acting on any atom vanishes when all atoms are displaced by the same amount. In terms of the IFC matrix, this condition reads

$$\sum_{lk} \Phi_{lk\alpha,l'k'\beta} = \sum_{l'k'} \Phi_{lk\alpha,l'k'\beta} = 0, \quad (2.15)$$

which must hold for all atoms and Cartesian directions  $\alpha, \beta$ .

Equivalently, in reciprocal space, the ASR implies that the dynamical matrix evaluated at the Brillouin-zone center satisfies

$$\sum_k \sqrt{M_k M_{k'}} D_{k\alpha,k'\beta}(\mathbf{q} = \mathbf{0}) = \sum_{k'} \sqrt{M_k M_{k'}} D_{k\alpha,k'\beta}(\mathbf{q} = \mathbf{0}) = 0, \quad (2.16)$$

Enforcing the acoustic sum rule can be relevant both first-principles and interpolation, that will be introduced later on, since it ensure the existence of three zero-frequency eigenvalues corresponding to the acoustic modes. Small numerical violations of translational invariance may otherwise lead to gaps, negative frequencies or incorrect slopes in the acoustic phonon branches near the  $\Gamma$  point, compromising the correct description.

## 2.2. Phonons in Density Functional Theory

In the framework of the Born–Oppenheimer approximation, phonons can be treated as a perturbation of the external potential  $V_{\text{ext}}$  introduced in the previous chapter. To determine vibrational properties, one typically assumes a linear response of the electronic ground state to ionic displacements.

Since the electronic density depends self-consistently on the ionic positions, the calculation of phonon frequencies is intimately coupled to the self-consistent field (SCF) cycle. There are two primary approaches to this problem: the **Finite Difference** method (also known as the Frozen Phonon method) and **Density Functional Perturbation Theory** (DFPT) [9, 10].

### 2.2.1. Finite Difference Method

In the Finite Difference (or Direct) approach, atoms in a supercell are explicitly displaced one by one by a small finite amount  $\lambda$  from their equilibrium positions. The response of the system is calculated by running a standard SCF calculation for each displaced configuration to obtain the Hellmann-Feynman forces.

$$\Phi_{kl\alpha,k'l'\beta} = -\frac{\partial F_{kl\alpha}}{\partial u_{k'l'\beta}} \approx -\frac{F_{kl\alpha}(\psi_{\lambda}^{u_{k'l'\beta}}) - F_{kl\alpha}(\psi_{-\lambda}^{u_{k'l'\beta}})}{2\lambda} \quad (2.17)$$

where  $F_{kl\alpha}(\psi_{\lambda}^{u_{k'l'\beta}})$  represents the force calculated on an atom in cell  $l$  in the supercell and basis atom  $k$  in cartesian direction *alpha* for the electronic configuration resulting from a displacement by  $\lambda$  of an atom and direction of the corresponding indeces  $l'k'\beta$ , solving an entire self-consistent problem 1.2 for each displacement. In practice, only the symmetry-irreducible atoms are displaced. The forces for the remaining atoms are reconstructed using the crystal symmetries (space group operations). The primary advantage of this technique is its simplicity and compatibility with any exchange-correlation functional or complex electronic structure method (e.g., hybrids, DFT+U) provided forces can be calculated. Intuitively, the Finite Difference approach is limited by the simulation cell size. Collective excitations with wavelengths larger than the unit cell cannot be described using only periodic boundary conditions on the primitive cell. Therefore, a convergence with respect to the **supercell** size must be achieved to capture the long-range interatomic force constants. Once convergence is achieved and the Force Constants are obtained in real space, they can be Fourier transformed to obtain the Dynamical Matrix at any arbitrary  $\mathbf{q}$ -point via Fourier Interpolation.

Representative phonon dispersion relations obtained within the Finite Difference approach are shown in Fig. 2.1 for the two benchmark materials introduced in Chapter 1, namely Si and LiF.

For the polar material LiF, the long-range dipole–dipole interaction leads to a non-analytic contribution to the dynamical matrix in the long-wavelength limit. Capturing this effect directly within the finite-difference approach would require very large supercells; instead, an analytical LO–TO splitting correction is applied, as discussed in the literature [8].

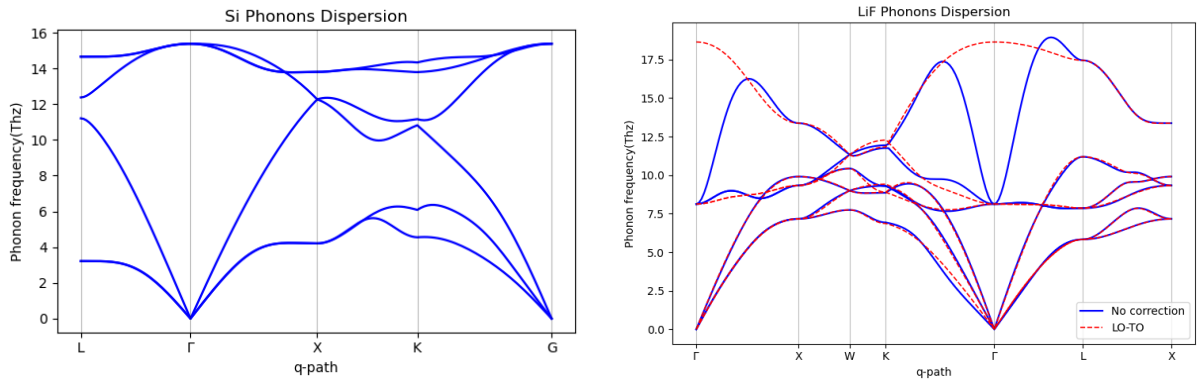


Figure 2.1: Phonon dispersion relations for Si (left) and LiF (right) obtained using the Finite Difference method within density functional theory. In both cases, interatomic force constants are computed using a  $4 \times 4 \times 4$  supercell and subsequently Fourier-interpolated to arbitrary wavevectors. For LiF, both the uncorrected dispersion and the result including the analytical LO–TO splitting correction are shown, accounting for the long-range dipole–dipole interaction characteristic of polar materials.

### 2.2.2. Density Functional Perturbation Theory (DFPT)

Density Functional Perturbation Theory provides an elegant alternative that avoids the use of commensurate supercells. Instead of numerical differentiation of the forces, it uses perturbation theory to compute the analytical linear response of the electron density to an ionic displacement.

In this framework, we start from the standard Kohn-Sham equations introduced in Eq. 1.41. By taking the linear variation of this equation with respect to an ionic displacement  $u_{lk\alpha}$  in an unit cell , we obtain the **Sternheimer Equations**:

$$\left( \hat{H}_{\text{KS}} - \varepsilon_n \right) \frac{\partial \phi_n}{\partial u_{lk\alpha}} = - \left( \frac{\partial \hat{V}_{\text{eff}}}{\partial u_{lk\alpha}} - \frac{\partial \varepsilon_n}{\partial u_{lk\alpha}} \right) \phi_n \quad (2.18)$$

This is a self-consistent linear system: the variation of the effective potential  $\frac{\partial \hat{V}_{\text{eff}}}{\partial u_{lk\alpha}}$  on the right-hand side depends on the variation of the charge density  $\frac{\partial \rho}{\partial u_{lk\alpha}}$ , which in turn depends on the solution  $\frac{\partial \phi_n}{\partial u_{lk\alpha}}$ . Note that the term  $\frac{\partial \varepsilon_n}{\partial u_{lk\alpha}}$  ensures orthogonality and acts as a Lagrange multiplier to keep the solution physical.

Once the derivative of the KS orbitals  $\frac{\partial \phi_n}{\partial u_{lk\alpha}}$  is computed by solving Eq. 2.18, we can construct the first-order perturbed wavefunctions:

$$\phi_{lk\alpha,n}^\lambda = \phi_n + \lambda \frac{\partial \phi_n}{\partial u_{lk\alpha}} \quad (2.19)$$

where  $\lambda$  is a small parameter. The second-order response (the Hessian matrix) can then be computed using a formula analogous to the finite difference approach, but using these analytically perturbed orbitals:

$$\Phi_{lk\alpha,l'k'\beta} \approx -\frac{F_{lk\alpha}[\{\phi_{l'k'\beta}^\lambda\}] - F_{lk\alpha}[\{\phi_{l'k'\beta}^{-\lambda}\}]}{2\lambda} \quad (2.20)$$

This hybrid approach allows for the precise calculation of harmonic properties without the numerical noise associated with displacing atoms in real space or the computational cost of large supercells.

## 2.3. Phonon Quantization

We now turn to the quantum mechanical treatment of lattice vibrations as discussed in [11, 12]. In the harmonic approximation, the Hamiltonian for the ionic system is given by the sum of the kinetic energy and the potential energy expanded to second order, maintaining consistent indexing over supercell  $l$ , basis element  $k$  and cartesian direction  $\alpha$ :

$$\hat{H}_{\text{ph}} = \sum_{lk\alpha} \frac{\hat{p}_{lk\alpha}^2}{2M_k} + \frac{1}{2} \sum_{lk\alpha,l'k'\beta} \Phi_{lk\alpha,l'k'\beta} \hat{u}_{lk\alpha} \hat{u}_{l'k'\beta} \quad (2.21)$$

In the quantum picture, the atomic displacements  $u_{lk\alpha}$  and conjugate momenta  $p_{lk\alpha}$  are promoted to Hermitian operators  $\hat{u}_{lk\alpha}$  and  $\hat{p}_{lk\alpha}$ . These operators must satisfy the fundamental canonical commutation relations:

$$[\hat{u}_{lk\alpha}, \hat{p}_{l'k'\beta}] = i\hbar\delta_{ll'}\delta_{kk'}\delta_{\alpha\beta}, \quad [\hat{u}_{lk\alpha}, \hat{u}_{l'k'\beta}] = 0, \quad [\hat{p}_{lk\alpha}, \hat{p}_{l'k'\beta}] = 0 \quad (2.22)$$

To decouple this Hamiltonian, we perform a canonical transformation to reciprocal space, introducing the *annihilation* ( $\hat{b}_{\mathbf{q}\nu}$ ) and *creation* ( $\hat{b}_{\mathbf{q}\nu}^\dagger$ ) operators for a phonon mode with

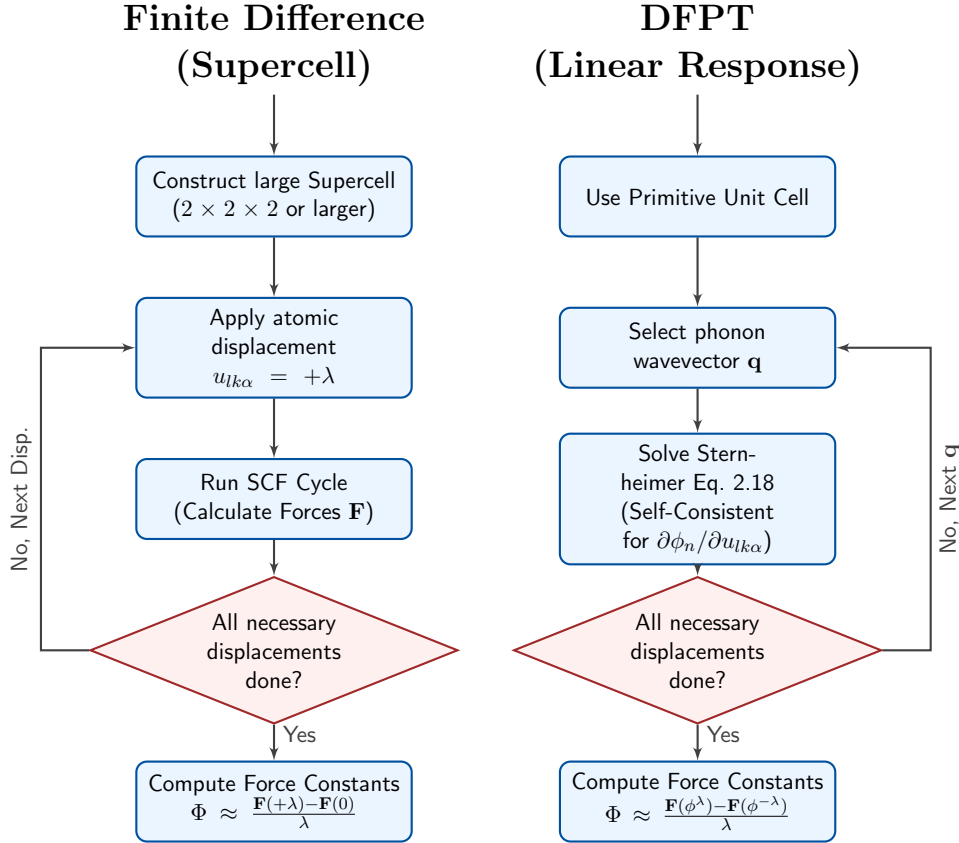


Figure 2.2: Workflow comparison between the Finite Difference (Supercell) approach and Density Functional Perturbation Theory (DFPT) for calculating vibrational properties.

wavevector  $\mathbf{q}$  and branch index  $\nu$ . The displacement operator is expanded in terms of the normal mode eigenvectors  $e_{k\alpha,\nu}(\mathbf{q})$  derived in the previous section:

$$\hat{u}_{lk\alpha} = \sum_{\mathbf{q}\nu} \sqrt{\frac{\hbar}{2NM_k\omega_\nu(\mathbf{q})}} \left( \hat{b}_{\mathbf{q}\nu} e^{i\mathbf{q}\cdot\mathbf{R}_l} + \hat{b}_{\mathbf{q}\nu}^\dagger e^{-i\mathbf{q}\cdot\mathbf{R}_l} \right) e_{k\alpha,\nu}(\mathbf{q}) \quad (2.23)$$

Similarly, the momentum operator is transformed as:

$$\hat{p}_{lk\alpha} = -i \sum_{\mathbf{q}\nu} \sqrt{\frac{\hbar M_k\omega_\nu(\mathbf{q})}{2N}} \left( \hat{b}_{\mathbf{q}\nu} e^{i\mathbf{q}\cdot\mathbf{R}_l} - \hat{b}_{\mathbf{q}\nu}^\dagger e^{-i\mathbf{q}\cdot\mathbf{R}_l} \right) e_{k\alpha,\nu}(\mathbf{q}) \quad (2.24)$$

Substituting these expressions into the Hamiltonian effectively diagonalizes the system. Using the orthogonality relations of the polarization vectors and the lattice summation rules, the complex system of coupled ions decouples into a sum of independent harmonic

oscillators:

$$\hat{H}_{\text{ph}} = \sum_{\mathbf{q}\nu} \hbar\omega_{\nu}(\mathbf{q}) \left( \hat{b}_{\mathbf{q}\nu}^{\dagger} \hat{b}_{\mathbf{q}\nu} + \frac{1}{2} \right) \quad (2.25)$$

### 2.3.1. Bosonic Nature of Phonons

The particle statistics of the phonon quasiparticles are determined by the commutation relations of the operators  $\hat{b}_{\mathbf{q}\nu}$  and  $\hat{b}_{\mathbf{q}\nu}^{\dagger}$ . By inverting the Fourier transforms above and utilizing the fundamental commutation rules for position and momentum (Eq. 2.22), one can derive:

$$[\hat{b}_{\mathbf{q}\nu}, \hat{b}_{\mathbf{q}'\nu'}^{\dagger}] = \delta_{\mathbf{q}\mathbf{q}'} \delta_{\nu\nu'} \quad (2.26)$$

and

$$[\hat{b}_{\mathbf{q}\nu}, \hat{b}_{\mathbf{q}'\nu'}] = 0, \quad [\hat{b}_{\mathbf{q}\nu}^{\dagger}, \hat{b}_{\mathbf{q}'\nu'}^{\dagger}] = 0 \quad (2.27)$$

These are exactly the **Canonical Commutation Relations (CCR)** characteristic of **Bosons**. Unlike electrons (fermions), which obey anti-commutation relations due to the Pauli exclusion principle, phonons can occupy the same quantum state in arbitrary numbers.

The number of phonons in a specific mode is given by the eigenvalue of the number operator  $\hat{n}_{\mathbf{q}\nu} = \hat{b}_{\mathbf{q}\nu}^{\dagger} \hat{b}_{\mathbf{q}\nu}$ . Physically,  $\hat{b}_{\mathbf{q}\nu}^{\dagger}$  creates a collective lattice excitation with energy  $\hbar\omega_{\nu}(\mathbf{q})$ , while  $\hat{b}_{\mathbf{q}\nu}$  annihilates one.

## 2.4. The Electron-Phonon Interaction

Having established the independent descriptions of electrons and lattice vibrations, we now turn to the coupling between these two dynamical systems. It is important to note that our framework remains grounded in the Born-Oppenheimer and harmonic approximations. In this picture, atoms are initially treated as distinguishable particles oscillating around equilibrium positions defined by the potential energy surface. However, the quantization of these collective harmonic displacements gives rise to a field of indistinguishable bosonic quasiparticles, the phonons.

Physically, this interaction arises because the motion of ions disrupts the perfect periodicity of the lattice potential experienced by the electrons [11]. In a general Quantum Field Theory context, this is described as a coupling mechanism where the fermionic matter field (electrons) exchanges energy and momentum with the bosonic field (phonons).

This coupling is responsible for a vast array of physical phenomena. At a fundamental

level, the lattice deformation dynamically modifies the ionic potential, causing the bare electrostatic interaction to become screened. Beyond this, the interaction has a profound impact on macroscopic properties, governing band structure renormalization and transport phenomena. Crucially, it also drives the formation of complex quasiparticles like polarons and provides the attractive glue required for Cooper pair formation in conventional superconductors.

Our immediate goal is to derive the interaction Hamiltonian,  $\hat{H}_{\text{el-ph}}$ , to first order in the displacements and discuss its calculation within DFT. However, unlike the independent-particle approximation used previously, calculating observables for the coupled system often demands a rigorous Many-Body Treatment. While analytical approaches provide valuable insights, they frequently rely on perturbative approximations that may not always hold. This limitation motivates the introduction of Quantum Monte Carlo methods, which allow for the precise computation of quantities such as correlators, as we will introduce in the following chapter.

### 2.4.1. Interaction Hamiltonian

The general many-body Hamiltonian describing the interaction between the electrons and the ionic lattice is given by the sum of the potential energy contributions from all  $N_e$  electrons:

$$\hat{H}_{\text{el-ion}} = \sum_{i=1}^{N_e} V_{\text{el-ion}}(\mathbf{r}_i, \{\mathbf{R}\}) \quad (2.28)$$

To derive the interaction term, we explicitly relax the static lattice assumption, an approximation that was implicitly retained even in the standard Born-Oppenheimer treatment of phonons, where the electronic energy is evaluated at fixed ionic positions. We assume that the ions undergo small displacements  $\mathbf{u}_{l\kappa}$  around their equilibrium dynamically interacting with the electrons. We formally expand the one-body electron-ion potential in a Taylor series with respect to these displacements:

$$V_{\text{el-ion}}(\mathbf{r}, \{\mathbf{R}\}) \approx V_{\text{el-ion}}(\mathbf{r}, \{\mathbf{R}^0\}) + \sum_{l\kappa\alpha} \left. \frac{\partial V_{\text{el-ion}}(\mathbf{r})}{\partial u_{l\kappa\alpha}} \right|_{\{\mathbf{R}^0\}} \hat{u}_{l\kappa\alpha} + \dots \quad (2.29)$$

The zeroth-order term,  $V_{\text{el-ion}}(\mathbf{r}, \{\mathbf{R}^0\})$ , represents the static periodic potential defining the electronic band structure and is absorbed into the unperturbed electronic Hamiltonian  $\hat{H}_{\text{el}}$ . The first-order term represents the perturbation responsible for electron-phonon scattering.

In the first quantization formalism, this interaction Hamiltonian is a sum over single-particle operators acting on each electron  $i$ :

$$\hat{H}_{\text{int}} = \sum_{i=1}^{N_e} \sum_{l\kappa\alpha} \nabla_{l\kappa\alpha} V_{\text{el-ion}}(\mathbf{r}_i) \cdot \hat{u}_{l\kappa\alpha} \quad (2.30)$$

To move to the second quantization formalism, we utilize the identity that maps a one-body operator  $\hat{O}$  to  $\int d^3r \hat{\psi}^\dagger(\mathbf{r}) \hat{O}(\mathbf{r}) \hat{\psi}(\mathbf{r})$ <sup>4</sup>. Introducing the electron density operator  $\hat{\rho}(\mathbf{r}) = \hat{\psi}^\dagger(\mathbf{r}) \hat{\psi}(\mathbf{r})$ , the interaction Hamiltonian becomes:

$$\hat{H}_{\text{int}} = \sum_{l\kappa\alpha} \int d^3r \hat{\rho}(\mathbf{r}) \nabla_{l\kappa\alpha} V_{\text{el-ion}}(\mathbf{r}) \cdot \hat{u}_{l\kappa\alpha} \quad (2.31)$$

To obtain the canonical form used in field theory, we transform the fields into the basis of Bloch eigenstates and the displacement operators into phonon normal modes. We use the expansions:

$$\hat{\psi}(\mathbf{r}) = \sum_{n\mathbf{k}} \langle \mathbf{r} | n\mathbf{k} \rangle \hat{c}_{n\mathbf{k}}, \quad \hat{u}_{l\kappa\alpha} = \sum_{\mathbf{q}\nu} \sqrt{\frac{\hbar}{2N_p M_\kappa \omega_{\mathbf{q}\nu}}} e^{i\mathbf{q}\cdot\mathbf{R}_l} \mathbf{e}_{\kappa\alpha,\nu}(\mathbf{q}) (\hat{b}_{\mathbf{q}\nu} + \hat{b}_{-\mathbf{q}\nu}^\dagger) \quad (2.32)$$

Substituting these expressions into Eq. 2.31 yields the fundamental **Electron-Phonon Hamiltonian**:

$$\hat{H}_{\text{el-ph}} = \frac{1}{\sqrt{N_p}} \sum_{\mathbf{k}, \mathbf{q}} \sum_{mn\nu} g_{mn,\nu}(\mathbf{k}, \mathbf{q}) \hat{c}_{m\mathbf{k}+\mathbf{q}}^\dagger \hat{c}_{n\mathbf{k}} (\hat{b}_{\mathbf{q}\nu} + \hat{b}_{-\mathbf{q}\nu}^\dagger) \quad (2.33)$$

This Hamiltonian describes the fundamental vertex of the interaction: an electron in state  $|n\mathbf{k}\rangle$  scatters to state  $|m\mathbf{k} + \mathbf{q}\rangle$  by either absorbing a phonon ( $\hat{b}_{\mathbf{q}\nu}$ ) or emitting a phonon ( $\hat{b}_{-\mathbf{q}\nu}^\dagger$ ). Momentum is conserved up to a reciprocal lattice vector  $\mathbf{G}$  (where  $\mathbf{k}' = \mathbf{k} + \mathbf{q} + \mathbf{G}$ ).

The physics of the interaction is entirely contained in the **coupling matrix element**  $g_{mn,\nu}(\mathbf{k}, \mathbf{q})$ :

$$g_{mn,\nu}(\mathbf{k}, \mathbf{q}) = \sum_{\kappa\alpha} \sqrt{\frac{\hbar}{2M_\kappa \omega_{\mathbf{q}\nu}}} \mathbf{e}_{\kappa\alpha,\nu}(\mathbf{q}) \cdot \langle m\mathbf{k} + \mathbf{q} | \nabla_{l\kappa\alpha} V(\mathbf{r}) | n\mathbf{k} \rangle \equiv \langle m\mathbf{k} + \mathbf{q} | \partial_{\mathbf{q}\nu} V(\mathbf{r}) | n\mathbf{k} \rangle \quad (2.34)$$

---

<sup>4</sup>This is the same of the one introduced in chapter 1 for creation and destruction operator but in a continuous basis using *Field operators*

where  $\nabla_{l\alpha}V$  is the change in the self-consistent effective potential felt by the electrons due to the lattice distortion, for this reason is often referred as **Deformation Potential**, in the last equation we have dropped the *el – ion* subscript and as we will show better in chapter 4 we have defined a generalized Fourier transform of the potential.

### 2.4.2. Screening and Linear Response

From a real many-body perspective, the potential gradient in the matrix element cannot simply be the gradient of the bare ionic potential. The electron gas is a polarizable medium; when an ion moves, the surrounding electron density rearranges almost instantaneously to screen the bare ionic perturbation.

In a general field-theoretic description, this is represented by the inverse dielectric function  $\epsilon^{-1}$ :

$$\nabla_{\mathbf{u}} V_{\text{eff}} = \epsilon^{-1} \nabla_{\mathbf{u}} V_{\text{bare}} \quad (2.35)$$

This effective screened potential is the quantity that must be inserted into the matrix element. Calculating this requires determining how the electron density responds to the lattice perturbation. This can be done, for instance, at first order in **Linear Response Theory**, considering an external perturbation given by the ions that couples linearly with the electron density. The potential can be expressed from the bare ionic potential through the electron dielectric function  $\epsilon(\mathbf{r}, \mathbf{r}')$ :

$$V_{\text{eff}}(\mathbf{r}; \{\tau_{kp}\}) = \int d^3 r' \epsilon^{-1}(\mathbf{r}, \mathbf{r}') \sum_{k \mathbf{R}_p} V_k^{\text{ion}}(\mathbf{r}' - \tau_{kp}) \quad (2.36)$$

Where  $k$  is a site index within each cell.

### 2.4.3. Electron-Phonon Coupling in Density Functional Theory

To connect our general derivation to DFT, which provides a practical computational scheme for this problem, we identify the "screened" potential with the self-consistent Kohn-Sham potential,  $V_{\text{KS}}$ , introduced in Eq. 1.40.

Thus, while the form of the Hamiltonian in Eq. 2.33 is general, the explicit calculation of the coupling vertex is typically performed considering the first-order variation of the Kohn-Sham potential with respect to ionic displacements:

$$g_{mn,\nu}(\mathbf{k}, \mathbf{q}) = \langle m\mathbf{k} + \mathbf{q} | \partial_{\mathbf{q}\nu} V_{\text{KS}} | n\mathbf{k} \rangle \quad (2.37)$$

This variation includes the response of the Hartree and Exchange-Correlation terms to the density variation and is the key quantity that will be exploited in Chapter 4 for Wannier interpolation.

Similar to phonon calculations, the same two approaches are valid here. The first is equivalent to the finite difference method, in which one evaluates the derivative of the Kohn-Sham potential for each possible mode in a supercell, and then takes the Fourier transform to pass to momentum space:

$$\partial_{\mathbf{q}\nu} V_{\text{KS}} \approx \sum_{l\kappa\alpha} e^{i\mathbf{q}\cdot\mathbf{R}_l} \mathbf{e}_{\kappa\alpha,\nu}(\mathbf{q}) \frac{V_{\text{KS}}(\{\mathbf{R} + \Delta\mathbf{u}_{l\kappa\alpha}\}) - V_{\text{KS}}(\{\mathbf{R} - \Delta\mathbf{u}_{l\kappa\alpha}\})}{2\Delta u} \quad (2.38)$$

As in the phonon case, the limit of this approach is the need for large supercells to capture long-wavelength modes, a limit that is easily overcome by DFPT.

As introduced previously for phonon calculations, DFPT avoids the use of supercells by solving the linearized Kohn-Sham (Sternheimer) equations self-consistently (Eq. 2.18), where the variation of the effective potential is already present. The equation can be expressed in reciprocal space to match the quantity required in the  $g_{mn,\nu}(\mathbf{k}, \mathbf{q})$  calculation [11, 13].

In practice, for a specific phonon wavevector  $\mathbf{q}$ , the self-consistent cycle proceeds iteratively. One starts by considering the bare ionic potential variation  $\partial_{\mathbf{q}\nu} V_{\text{ext}}$  as the external perturbation. In each step of the cycle, the Sternheimer equation is solved to obtain the first-order variation of the Kohn-Sham orbitals,  $\Delta\psi_{n\mathbf{k}}$ . These perturbed orbitals are then used to construct the linear variation of the charge density,  $\Delta n(\mathbf{r})$ . This density response, in turn, updates the variation of the Hartree and exchange-correlation potentials via their functional derivatives. The cycle repeats until the total potential variation  $\Delta V_{\text{SCF}}$  converges. The final result is the fully screened deformation potential, which is directly inserted into the expression for the coupling matrix element.

While DFPT is the standard approach, other methods are possible and may offer advantages in specific cases. For instance, **Stochastic displacement** and **One Shot** approaches [14] allow for the direct calculation of specific observables, such as Band Gap Renormalization, without explicitly constructing the full electron-phonon matrix elements.

# 3 | Diagrammatic Monte Carlo

## 3.1. Quantum Many-Body Theory

The purpose of this section is to give a concise overview of quantum many-body theory using the language of quantum field theory. The central object in this framework is the Green function, which encodes the properties of an interacting quantum system through its correlation functions. Its perturbative expansion, naturally represented in terms of Feynman diagrams, provides a systematic way to account for interactions and constitutes the basis of diagrammatic Monte Carlo techniques [6, 15].

### 3.1.1. Time Evolution

The full electron–phonon Hamiltonian can be seen as a free term  $H_0 = H_e + H_{ph}$ , defined in Eqs. 1.51 and 2.25 respectively, plus the interaction term  $H_I = H_{el-ph}$ . This separation, which already determines the difficulty of solving the eigenvalue problem in the time-independent Schrödinger equation, becomes relevant also when considering the time-dependent one.

The most common way to introduce time evolution in quantum mechanics is by considering the so-called *Schrödinger picture*, where the operators corresponding to observables are immutable quantities,  $\hat{O}_S = \hat{O}$ , and the state evolves according to the *Schrödinger equation*:

$$i\hbar \frac{\partial}{\partial t} |\Psi_S(t)\rangle = \hat{H} |\Psi_S(t)\rangle \quad \Rightarrow \quad |\Psi_S(t)\rangle = e^{-\frac{i}{\hbar} \hat{H} t} |\Psi_S(0)\rangle. \quad (3.1)$$

Here  $S$  stands for Schrödinger.

An opposite, yet equivalent, picture is the Heisenberg one, where the state does not evolve,  $|\Psi_H\rangle = |\Psi_S(0)\rangle$ , and the operators, with initial condition  $\hat{O}_H(0) = \hat{O}_S = \hat{O}$ , evolve according to an equivalent law that can be deduced by imposing the invariance of matrix elements:

$$\langle \Psi_S(t) | \hat{O}_S | \Psi_S(t) \rangle = \langle \Psi_H | \hat{O}_H(t) | \Psi_H \rangle \quad \Rightarrow \quad \hat{O}_H(t) = e^{\frac{i}{\hbar} \hat{H} t} \hat{O} e^{-\frac{i}{\hbar} \hat{H} t}. \quad (3.2)$$

It is important to notice that the Hamiltonian exponential is itself an operator, which reduces to a simple phase only in diagonal cases. More precisely, by deriving Eq. (3.2), one finds the Heisenberg equation of motion:

$$\frac{\partial}{\partial t} \hat{O}_H(t) = e^{\frac{i}{\hbar} \hat{H}t} [\hat{O}, \hat{H}] e^{-\frac{i}{\hbar} \hat{H}t}. \quad (3.3)$$

For the free electronic Hamiltonian, written in diagonal form,

$$\hat{H}_e = \sum_{n\mathbf{k}} \varepsilon_{n\mathbf{k}} \hat{c}_{n\mathbf{k}}^\dagger \hat{c}_{n\mathbf{k}}, \quad (3.4)$$

the Heisenberg evolution reads

$$\hat{c}_{n\mathbf{k}}(t) = e^{\frac{i}{\hbar} \hat{H}_e t} \hat{c}_{n\mathbf{k}} e^{-\frac{i}{\hbar} \hat{H}_e t}. \quad (3.5)$$

Using the commutator identity  $[AB, C] = A[B, C] + [A, C]B$  and the canonical anticommutation relations, one finds

$$\begin{aligned} [\hat{H}_e, \hat{c}_{n\mathbf{k}}] &= \sum_{n'\mathbf{k}'} \varepsilon_{n'\mathbf{k}'} [\hat{c}_{n'\mathbf{k}'}^\dagger \hat{c}_{n'\mathbf{k}'}, \hat{c}_{n\mathbf{k}}] \\ &= \sum_{n'\mathbf{k}'} \varepsilon_{n'\mathbf{k}'} \left( \hat{c}_{n'\mathbf{k}'}^\dagger [\hat{c}_{n'\mathbf{k}'}, \hat{c}_{n\mathbf{k}}] + [\hat{c}_{n'\mathbf{k}'}^\dagger, \hat{c}_{n\mathbf{k}}] \hat{c}_{n'\mathbf{k}'} \right) \\ &= \sum_{n'\mathbf{k}'} \varepsilon_{n'\mathbf{k}'} (0 - \delta_{nn'} \delta_{\mathbf{k}\mathbf{k}'} \hat{c}_{n'\mathbf{k}'}) = -\varepsilon_{n\mathbf{k}} \hat{c}_{n\mathbf{k}}. \end{aligned} \quad (3.6)$$

Therefore, from the Heisenberg equation  $i\hbar \partial_t \hat{c}_{n\mathbf{k}}(t) = [\hat{c}_{n\mathbf{k}}(t), \hat{H}_e]$ , one obtains

$$i\hbar \partial_t \hat{c}_{n\mathbf{k}}(t) = \varepsilon_{n\mathbf{k}} \hat{c}_{n\mathbf{k}}(t), \quad (3.7)$$

whose solution is

$$\hat{c}_{n\mathbf{k}}(t) = e^{-\frac{i}{\hbar} \varepsilon_{n\mathbf{k}} t} \hat{c}_{n\mathbf{k}}. \quad (3.8)$$

In other cases, however, the commutator may not be simple, and the nature of the operator itself is not guaranteed. In particular, an operator acting as a creator on the vacuum at time  $t = 0$  may acquire a more complex action after time evolution, for instance the action on the vacuum can result in a linear combination of eigenstates.

For this reason, when dealing with Hamiltonians consisting of a free term that makes the problem diagonal, multiplied by an interaction term, one introduces an intermediate

treatment known as the *interaction (or Dirac) picture*. In this picture, operators evolve according to the Heisenberg picture dictated only by the non-interacting Hamiltonian, while the states evolve with the interaction term:

$$\hat{O}_I(t) = e^{\frac{i}{\hbar} \hat{H}_0 t} \hat{O} e^{-\frac{i}{\hbar} \hat{H}_0 t}, \quad |\Psi_I(t)\rangle = e^{-\frac{i}{\hbar} \hat{H}_I t} |\Psi_I(0)\rangle \equiv U_I(t, t') |\Psi_I(t')\rangle. \quad (3.9)$$

In the last identity, we introduced the evolution operator in the interaction picture,  $U_I(t, t')$ . From its fundamental properties and from the original time evolution equation, one can show that it satisfies an equation of motion equivalent to the Schrödinger equation:

$$i\hbar \partial_t U_I(t, t') = [\hat{H}_I]_{H_0}(t) U_I(t, t'), \quad (3.10)$$

where  $[\hat{H}_I]_{H_0}(t)$  is the interaction Hamiltonian evolved in the Heisenberg picture with respect to the non-interacting Hamiltonian  $\hat{H}_0$ . Intuitively, this intermediate picture is convenient because, for instance, creation and destruction operators preserve their nature. More rigorously, starting from the initial condition  $U_I(t, t) = I$  and iterating Eq. (3.10), one obtains the so-called Dyson series:

$$U_I(t, t') = 1 + \sum_{n=1}^{\infty} \left(-\frac{i}{\hbar}\right)^n \int_{t'}^t dt_1 \int_{t'}^{t_1} dt_2 \cdots \int_{t'}^{t_{n-1}} dt_n [\hat{H}_I]_{H_0}(t_1) [\hat{H}_I]_{H_0}(t_2) \cdots [\hat{H}_I]_{H_0}(t_n), \quad (3.11)$$

which can be compactly written introducing the time-ordered exponential,

$$U_I(t, t') \equiv T \exp \left[ -\frac{i}{\hbar} \int_{t'}^t d\tau [\hat{H}_I]_{H_0}(\tau) \right]. \quad (3.12)$$

The fundamental result connecting the interaction picture and its application in many-body theory is the theorem introduced by Gell-Mann and Low in [16]. Here we refer to [17] for a more didactic explanation. The theorem explicitly connects the interacting ground state  $|E\rangle$  of  $\hat{H}$  with the non-interacting one  $|E_0\rangle$  of  $\hat{H}_0$ .

The theorem first considers an adiabatic switching of the perturbation through a time-dependent Hamiltonian:

$$\hat{H}_\epsilon(t) = \hat{H}_0 + e^{-\epsilon|t|} \hat{H}_I, \quad (3.13)$$

consisting of an unperturbed system where the perturbation is time-dependent and acts over a time scale  $\tau = 1/\epsilon$ .

In adiabatic theories one expects the wavefunction to change continuously with the pertur-

bation and to adapt to the instantaneous spectrum of the Hamiltonian. Considering the evolution from  $\pm\infty$  to 0, the system is evolved from  $\hat{H}_0$  to the full interacting Hamiltonian  $\hat{H}$ . The theorem states that, if the following limits exist,

$$|\Psi_{\pm}\rangle = \lim_{\epsilon \rightarrow 0^+} \frac{U_{\epsilon,I}(0, \pm\infty) |E_0\rangle}{\langle E_0 | U_{\epsilon,I}(0, \pm\infty) |E_0\rangle}, \quad (3.14)$$

then  $|\Psi_{\pm}\rangle$  are eigenvectors of the interacting Hamiltonian  $\hat{H}$ .

It is important to notice, however, that the theorem does not ensure by itself that these states correspond to the ground state of  $\hat{H}$ . If one assumes that  $|E_0\rangle$  is non-degenerate and then there is no degeneracy removal by the perturbation for any finite  $\epsilon$ , and further assumes the absence of level crossing during the adiabatic evolution, then the two limits are related by a phase,

$$|\Psi_+\rangle = e^{i\delta} |\Psi_-\rangle, \quad (3.15)$$

and define the ground state of the interacting Hamiltonian.

### 3.1.2. Green Function

One of the key quantities for the study of many-body systems is the *Green function*. Here we consider its time-ordered version, from which many equilibrium properties can be deduced, for instance those related to single-particle operator averages, quasi-particle formalism, and also properties at finite temperature (see later). Its usage extends also to non-equilibrium systems, with the introduction of *advanced* and *retarded* Green functions, which are particularly relevant for transport and optical response properties [18].

In the case of the time-ordered Green function, one first introduces the *time-ordering operator*  $\mathcal{T}$ , defined as an operator that, acting on any set of creation and destruction operators time-evolved in the Heisenberg picture with respect to the full Hamiltonian  $\hat{H}$ , produces a time-ordered sequence of operators:

$$\mathcal{T} [\hat{A}_1(t_1) \hat{A}_2(t_2) \cdots \hat{A}_N(t_N)] = (\pm 1)^{\sigma} \hat{A}_{\sigma_1}(t_{\sigma_1}) \cdots \hat{A}_{\sigma_N}(t_{\sigma_N}), \quad (3.16)$$

where the operators are ordered such that  $t_{\sigma_1} > \cdots > t_{\sigma_N}$ ,  $\sigma$  is the permutation required to achieve the ordering, and the sign  $\pm$  refers to bosons or fermions, respectively. The main advantage of considering time-ordered averages is that operators can be freely exchanged, accounting only for a sign change in the case of an odd permutation for fermions.

In the electron–phonon case one can consider, as a starting point, the time-ordered Green

function for electrons:

$$\begin{aligned} G_{mn\mathbf{k}\mathbf{k}'}(t, t') &= -i\langle \text{GS} | \mathcal{T} \hat{c}_{m\mathbf{k}}(t) \hat{c}_{n\mathbf{k}'}^\dagger(t') | \text{GS} \rangle \\ &= -i\theta(t - t') \langle \text{GS} | \hat{c}_{m\mathbf{k}}(t) \hat{c}_{n\mathbf{k}'}^\dagger(t') | \text{GS} \rangle + i\theta(t' - t) \langle \text{GS} | \hat{c}_{n\mathbf{k}'}^\dagger(t') \hat{c}_{m\mathbf{k}}(t) | \text{GS} \rangle. \end{aligned} \quad (3.17)$$

In this definition the operators are evolved with respect to the full Hamiltonian  $\hat{H}$  in the Heisenberg picture, and the effect of time ordering has been made explicit through the Heaviside step function  $\theta(t - t')$ .

To understand why one often refers to the Green function as a *quantum correlator*, let us consider the case  $t > t'$ . Writing explicitly the Heisenberg time evolution and using the fact that the ground state is an eigenstate of the Hamiltonian, one finds

$$\begin{aligned} G_{mn\mathbf{k}\mathbf{k}'}(t, t') &= -i\langle \text{GS} | \hat{c}_{m\mathbf{k}}(t) \hat{c}_{n\mathbf{k}'}^\dagger(t') | \text{GS} \rangle \\ &= -ie^{\frac{i}{\hbar}E_{\text{GS}}(t-t')} \langle \text{GS} | \hat{c}_{m\mathbf{k}} e^{-\frac{i}{\hbar}\hat{H}(t-t')} \hat{c}_{n\mathbf{k}'}^\dagger | \text{GS} \rangle. \end{aligned} \quad (3.18)$$

From this expression, the Green function can be interpreted either as the overlap between an excited state  $|n\mathbf{k}'\rangle$  created on top of the ground state, evolved for a time  $(t - t')$ , and another excited state  $|m\mathbf{k}\rangle$ , or equivalently as a matrix element encoding the probability amplitude for a particle created in the first state to be found in the second excited state of the many body system after a  $(t - t')$  evolution.

The connection between Green functions and single-particle observables becomes explicit when considering a generic one-body operator, previously introduced as

$$\hat{A}^{(1)} = \sum_{i,j} \langle i | \hat{a} | j \rangle \hat{c}_i^\dagger \hat{c}_j. \quad (3.19)$$

Using the properties of the time-ordered Green function, the ground-state average of a generic single-particle operator

$$\hat{A}^{(1)} = \sum_{i,j} \langle i | \hat{a} | j \rangle \hat{c}_i^\dagger \hat{c}_j \quad (3.20)$$

can be written explicitly as

$$\langle \text{GS} | \hat{A}^{(1)} | \text{GS} \rangle = \sum_{i,j} \langle i | \hat{a} | j \rangle \langle \text{GS} | \hat{c}_i^\dagger \hat{c}_j | \text{GS} \rangle. \quad (3.21)$$

By introducing the limit  $t' \rightarrow t^+$  and using the definition of the time-ordered Green function, one obtains

$$\langle \text{GS} | \hat{c}_i^\dagger \hat{c}_j | \text{GS} \rangle = \langle \text{GS} | \mathcal{T} \hat{c}_i^\dagger(t^+) \hat{c}_j(t) | \text{GS} \rangle = -i G_{ji}(t, t^+), \quad (3.22)$$

so that

$$\langle \text{GS} | \hat{A}^{(1)} | \text{GS} \rangle = -i \sum_{i,j} \langle i | \hat{a} | j \rangle G_{ji}(t, t^+). \quad (3.23)$$

As a particular case, choosing  $\hat{a} = \mathbf{1}$ , the single-particle operator reduces to the density operator, and one recovers

$$\langle \text{GS} | \hat{n} | \text{GS} \rangle = \sum_i \langle \text{GS} | \hat{c}_i^\dagger \hat{c}_i | \text{GS} \rangle = -i \sum_i G_{ii}(t, t^+), \quad (3.24)$$

showing explicitly that the particle density is given by the equal-time limit of the Green function.

As a simple but useful example, being the building Block of Feynman diagrams, one can consider the Green function of free fermions, described by the Hamiltonian  $\hat{H}_0 = \sum_{n\mathbf{k}} \varepsilon_{n\mathbf{k}} \hat{c}_{n\mathbf{k}}^\dagger \hat{c}_{n\mathbf{k}}$ . In this case the time evolution of the operators as arleady seen is,  $\hat{c}_{n\mathbf{k}}(t) = e^{-\frac{i}{\hbar} \varepsilon_{n\mathbf{k}} t} \hat{c}_{n\mathbf{k}}$ , and the time-ordered Green function reads

$$\begin{aligned} G_{n\mathbf{k}}^{(0)}(t, t') &= -i\theta(t - t') e^{-\frac{i}{\hbar} \varepsilon_{n\mathbf{k}}(t-t')} (1 - n_{n\mathbf{k}}) \\ &\quad + i\theta(t' - t) e^{-\frac{i}{\hbar} \varepsilon_{n\mathbf{k}}(t-t')} n_{n\mathbf{k}}, \end{aligned} \quad (3.25)$$

where  $n_{n\mathbf{k}}$  is the occupation number of the state  $(n, \mathbf{k})$  in the ground state, and we indicate simply one state because the off-diagonal terms are 0.

Although Green functions are often introduced in real space, working in momentum space for a periodic lattice system, as done here, is completely equivalent and particularly convenient when the free Hamiltonian is diagonal in the  $(n, \mathbf{k})$  basis. Finally, in systems invariant under time translations, as we will assume from now on, the Green function depends only on the time difference  $\tau = (t - t')$ , and it is often useful to introduce its Fourier transform to frequency space.

In a similar way, one introduces the Green function for free phonons, which will be used in the following. We consider the non-interacting phonon Hamiltonian,

$$\hat{H}_{\text{ph}} = \sum_{\mathbf{q}\nu} \hbar\omega_\nu(\mathbf{q}) \left( \hat{b}_{\mathbf{q}\nu}^\dagger \hat{b}_{\mathbf{q}\nu} + \frac{1}{2} \right), \quad (3.26)$$

for which the Heisenberg time evolution of the bosonic operators is governed only by  $\hat{H}_{\text{ph}}^1$ . One then finds

$$\hat{b}_{\nu\mathbf{q}}(t) = e^{-i\omega_{\nu\mathbf{q}}t} \hat{b}_{\nu\mathbf{q}}, \quad \hat{b}_{\nu\mathbf{q}}^\dagger(t) = e^{+i\omega_{\nu\mathbf{q}}t} \hat{b}_{\nu\mathbf{q}}^\dagger. \quad (3.27)$$

The time-ordered Green function for free phonons is defined as

$$D_{\nu\mathbf{q}}^{(0)}(t, t') = -i \langle GS | \mathcal{T} [\hat{b}_{\nu\mathbf{q}}(t) \hat{b}_{\nu\mathbf{q}}^\dagger(t')] | GS \rangle, \quad (3.28)$$

which, by explicitly performing the time ordering, gives and the explicit time dependence of the operators and the bosonic commutation relations, one finally obtains the free phonon propagator

$$D_{\nu\mathbf{q}}^{(0)}(t - t') = -i \left[ \theta(t - t') e^{-i\omega_{\nu\mathbf{q}}(t-t')} + \theta(t' - t) e^{+i\omega_{\nu\mathbf{q}}(t-t')} \right]. \quad (3.29)$$

### 3.1.3. Finite Temperature

The thermal properties of a quantum system, especially in second quantization, are naturally described within the *grand-canonical ensemble*, representing a system in contact with a thermal reservoir at temperature  $T$ , with which it can exchange particles. In the many-body case this description is particularly well suited, since the formalism is built in terms of operators creating and destroying particles in Fock space.

The ground state is now replaced by a classical thermal mixture of many-body states, including the zero-temperature ground state, with populations described by the *density operator*

$$\hat{\rho} = \frac{1}{Z} e^{-\beta(\hat{H} - \sum_i \mu_i \hat{N}_i)}, \quad (3.30a)$$

$$Z = \text{tr} \left[ e^{-\beta(\hat{H} - \sum_i \mu_i \hat{N}_i)} \right], \quad (3.30b)$$

where  $\beta = (k_B T)^{-1}$  and  $Z$  is the grand-canonical partition function. At finite temperature the state of the system is therefore fixed not only by the Hamiltonian, but also by the temperature  $T$  and by the chemical potentials  $\mu_i$ , which control the occupation of the single-particle states  $|n\mathbf{k}\rangle$ .

The thermal average of an operator is defined as

---

<sup>1</sup>Since in Eq. 3.3 the bosonic operators  $\hat{b}^{(\dagger)}$  commute with  $\hat{H}_{\text{el}}$ , which depends solely on fermionic degrees of freedom.

$$\langle \hat{O} \rangle = \text{tr}(\hat{\rho} \hat{O}). \quad (3.31)$$

Within this formalism it is extremely convenient to introduce an alternative notion of time evolution adapted to thermal equilibrium. Defining the grand-canonical Hamiltonian <sup>2</sup>

$$\hat{K} = \hat{H} - \sum_i \mu_i \hat{N}_i \equiv \hat{K}_0 + \hat{H}_I, \quad (3.32)$$

one can formally interpret the density operator as an evolution operator in *imaginary time*, performing the substitution  $it/\hbar \rightarrow \tau$  with  $\tau \in [0, \hbar\beta]$ . In this way one obtains

$$\hat{\rho} \propto e^{-\beta \hat{K}} = e^{-\beta \hat{K}_0} U_I(-i\hbar\beta, 0), \quad (3.33a)$$

$$Z = \text{tr}[e^{-\beta \hat{K}}] = Z_0 \langle U_I(-i\hbar\beta, 0) \rangle_0, \quad (3.33b)$$

where  $U_I(\tau, 0)$  is the interaction-picture evolution operator at imaginary time and  $\langle \cdots \rangle_0$  denotes a thermal average with respect to  $\hat{K}_0$  and  $Z_0$  the relative partition function.

In complete analogy with the zero-temperature case, one can therefore define *thermal Green functions* as imaginary-time ordered correlators. All properties of time ordering and perturbative expansions discussed previously and in the following carry over to this framework, with the only difference that operators now evolve along the imaginary-time axis and  $\tau$  is restricted to the interval  $[-\hbar\beta, +\hbar\beta]$ . These thermal correlators play a central role in many theoretical developments, in particular because of the *fluctuation-dissipation theorem*, which links equilibrium fluctuations, expressed through correlation functions, to the linear response of the system to external perturbations.

As an example, the free fermionic thermal Green function in imaginary time reads

$$G_{n\mathbf{k}}^{(0)}(\tau) = -[(1 - f_{n\mathbf{k}})\theta(\tau) - f_{n\mathbf{k}}\theta(-\tau)]e^{-(\varepsilon_{n\mathbf{k}} - \mu)\tau}, \quad 0 \leq \tau \leq \hbar\beta, \quad (3.34)$$

where  $f_{n\mathbf{k}}$  is the Fermi–Dirac distribution. It is possible to show that, at the boundaries of

---

<sup>2</sup>In the occupation-number basis for a single fermionic mode  $(n\mathbf{k})$ ,  $\{|0\rangle, |1\rangle\}$  with  $\hat{n} \equiv \hat{c}_{n\mathbf{k}}^\dagger \hat{c}_{n\mathbf{k}}$ , the grand-canonical operator factorizes mode by mode, and one obtain the usual *Fermi-Dirac* distribution. Restricting to one mode,  $\hat{K} = (\varepsilon_{n\mathbf{k}} - \mu)\hat{n}$ , hence  $\hat{\rho} = Z^{-1}e^{-\beta(\varepsilon_{n\mathbf{k}} - \mu)\hat{n}}$  with  $Z = \text{tr} e^{-\beta(\varepsilon_{n\mathbf{k}} - \mu)\hat{n}} = \langle 0|e^0|0\rangle + \langle 1|e^{-\beta(\varepsilon_{n\mathbf{k}} - \mu)}|1\rangle = 1 + e^{-\beta(\varepsilon_{n\mathbf{k}} - \mu)}$ . Therefore,

$$\langle \hat{n} \rangle = \text{tr}(\hat{\rho} \hat{n}) = \frac{0 \cdot 1 + 1 \cdot e^{-\beta(\varepsilon_{n\mathbf{k}} - \mu)}}{1 + e^{-\beta(\varepsilon_{n\mathbf{k}} - \mu)}} = \frac{1}{e^{\beta(\varepsilon_{n\mathbf{k}} - \mu)} + 1} \equiv f_{n\mathbf{k}}.$$

the imaginary-time interval, the Green function is periodic for fermions and anti-periodic for bosons. Therefore one can introduce a Fourier representation in terms of discrete *Matsubara frequencies*, which, as a consequence of the (anti-)periodicity, are given by

$$\omega_n = \frac{(2n+1)\pi}{\hbar\beta} \quad (\text{fermions}), \quad \omega_n = \frac{2n\pi}{\hbar\beta} \quad (\text{bosons}). \quad (3.35)$$

This allows one to work equivalently in frequency space. Analytic continuation from Matsubara frequencies to the real axis then provides access to real-time response functions.

In the following we will freely move between the zero-temperature real-time formalism and the finite-temperature imaginary-time formalism, depending on the physical context, exploiting the close analogy between the two cases. At the same time, we will mostly use the imaginary time notation for simplicity. A more comprehensive exposition of these results at finite temperature can be found in [6].

### 3.1.4. Reduction Formula

The time-ordered Green function, both at zero and at finite temperature, is non-trivial in the interacting case. This is mainly because the Heisenberg time evolution of the operators appearing inside the expectation value is as complex as solving the many-body problem itself. Two theorems play a central role in this context: the first follows from the Gell-Mann and Low theorem, while the second, named after the Italian physicist Giancarlo Wick, allows one to construct a systematic perturbative expansion of Green functions, which is naturally represented in terms of Feynman diagrams.

As a direct consequence of the Gell-Mann and Low theorem, one can show that, under the action of the time-ordering operator, the following identity holds, usually referred to as the **reduction formula**:

$$\langle \text{GS} | \mathcal{T} \hat{O}_1^H(t_1) \cdots \hat{O}_n^H(t_n) | \text{GS} \rangle = \frac{\langle \text{GS}_0 | \mathcal{T} \hat{S} \hat{O}_1^I(t_1) \cdots \hat{O}_n^I(t_n) | \text{GS}_0 \rangle}{\langle \text{GS}_0 | \hat{S} | \text{GS}_0 \rangle}. \quad (3.36)$$

Here  $|\text{GS}\rangle$  and  $|\text{GS}_0\rangle$  denote the interacting and non-interacting ground states, respectively,  $\hat{O}^H(t)$  are operators evolved in the Heisenberg picture with respect to the full Hamiltonian  $\hat{H}$ , while  $\hat{O}^I(t)$  are the corresponding operators in the interaction picture. The operator

$$\hat{S} = U_I(+\infty, -\infty) \quad (3.37)$$

is the scattering operator, for which the Dyson expansion 3.11 holds. This identity allows

one to express interacting time-ordered correlators in terms of interaction-picture operators and provides the starting point for the diagrammatic perturbation theory of Green functions. It is important to notice that here we are dealing with the *single particle* Green Function, as we have defined it, in the general theory one can encounter also the two, three... particle Green Function, the Reduction Formula, is general enough to hold even in that cases.

For our purposes, we derive the reduction formula in the case of the electronic one-particle Green function; the general proof does not differ substantially. We start from the definition

$$G_{mn\mathbf{k}\mathbf{k}'}(\tau) = -i\langle \text{GS} | \mathcal{T} \hat{c}_{m\mathbf{k}}(\tau) \hat{c}_{n\mathbf{k}'}^\dagger(0) | \text{GS} \rangle.$$

We now apply the Gell-Mann and Low theorem to express the interacting ground state, assuming that we are in a regime where it can be adiabatically connected to the non-interacting one. In particular, we assume that the states  $|\Psi_+\rangle$  and  $|\Psi_-\rangle$  coincide with  $|\text{GS}\rangle$  up to a normalization constant. One then obtains

$$\begin{aligned} \langle \text{GS} | \mathcal{T} \hat{c}_{m\mathbf{k}}(\tau) \hat{c}_{n\mathbf{k}'}^\dagger(0) | \text{GS} \rangle &\stackrel{(a)}{=} \frac{\langle \Psi_+ | \mathcal{T} \hat{c}_{m\mathbf{k}}(\tau) \hat{c}_{n\mathbf{k}'}^\dagger(0) | \Psi_- \rangle}{\langle \Psi_+ | \Psi_- \rangle} \\ &\stackrel{(b)}{=} \frac{\langle \text{GS}_0 | \mathcal{T} U_I(+\infty, 0) \hat{c}_{m\mathbf{k}}(\tau) \hat{c}_{n\mathbf{k}'}^\dagger(0) U_I(0, -\infty) | \text{GS}_0 \rangle}{\langle \text{GS}_0 | U_I(+\infty, 0) U_I(0, -\infty) | \text{GS}_0 \rangle} \\ &\stackrel{(c)}{=} \frac{\langle \text{GS}_0 | \mathcal{T} U_I(+\infty, 0) U_I(0, \tau) \hat{c}_{m\mathbf{k}}^{H_0}(\tau) U_I(\tau, 0) \hat{c}_{n\mathbf{k}'}^{H_0\dagger}(0) U_I(0, -\infty) | \text{GS}_0 \rangle}{\langle \text{GS}_0 | U_I(+\infty, 0) U_I(0, -\infty) | \text{GS}_0 \rangle} \\ &\stackrel{(d)}{=} \frac{\langle \text{GS}_0 | \mathcal{T} U_I(+\infty, 0) U_I(0, \tau) U_I(\tau, 0) U_I(0, -\infty) \hat{c}_{m\mathbf{k}}^{H_0}(\tau) \hat{c}_{n\mathbf{k}'}^{H_0\dagger}(0) | \text{GS}_0 \rangle}{\langle \text{GS}_0 | U_I(+\infty, 0) U_I(0, -\infty) | \text{GS}_0 \rangle} \\ &\stackrel{(e)}{=} \frac{\langle \text{GS}_0 | \mathcal{T} \hat{S} \hat{c}_{m\mathbf{k}}^{H_0}(\tau) \hat{c}_{n\mathbf{k}'}^{H_0\dagger}(0) | \text{GS}_0 \rangle}{\langle \text{GS}_0 | \hat{S} | \text{GS}_0 \rangle} \end{aligned}$$

In step (a) the denominator accounts for the different normalization of the interacting states. In step (b) we explicitly introduce the Gell-Mann and Low theorem, assuming that the limit  $\epsilon \rightarrow 0$  has already been taken and is well defined. In step (c) we express the operator evolution in the interaction picture and use the properties of the time-evolution operator: (i)  $U_I^\dagger(t, t') = U_I(t', t)$  and (ii)  $U_I(t, t) = \mathbf{1}$ . In step (d) we exploit the fact that, since the Dyson expansion of the propagators is expressed in terms of creation and destruction operators, the time-ordering operator allows one to freely reorder them. Finally, in step (e) we use the composition property of the evolution operator,  $U_I(t, t'') U_I(t'', t') = U_I(t, t')$ .

Starting from the reduction formula, the interacting time-ordered electronic Green function can be written in terms of interaction-picture operators as

$$G_{mn\mathbf{kk}'}(\tau) = -i \frac{\langle \text{GS}_0 | \mathcal{T} \left[ \hat{S} \hat{c}_{m\mathbf{k}}^{H_0}(\tau) \hat{c}_{n\mathbf{k}'}^{H_0\dagger}(0) \right] | \text{GS}_0 \rangle}{\langle \text{GS}_0 | \hat{S} | \text{GS}_0 \rangle}, \quad \hat{S} \equiv U_I(+\infty, -\infty). \quad (3.38)$$

For the moment we neglect the denominator, and we will discuss its role later. In this approximation, the Green function is proportional to the numerator, namely to a time-ordered correlator with insertions of the scattering operator  $\hat{S}$ .

Using the Dyson expansion (3.11), the scattering operator can be written as

$$\hat{S} = 1 + \sum_{n=1}^{\infty} \left( -\frac{i}{\hbar} \right)^n \frac{1}{n!} \int_{-\infty}^{+\infty} d\tau_1 \cdots d\tau_n \mathcal{T} \left[ [\hat{H}_I]_{H_0}(\tau_1) \cdots [\hat{H}_I]_{H_0}(\tau_n) \right]. \quad (3.39)$$

Inserting this expansion into the Green function yields a perturbative series. The zeroth-order term gives the free-electron Green function

$$G_{n\mathbf{k}}^{(0)}(\tau) = -i \langle \text{GS}_0 | \mathcal{T} \hat{c}_{n\mathbf{k}}^{H_0}(\tau) \hat{c}_{n\mathbf{k}}^{H_0\dagger}(0) | \text{GS}_0 \rangle. \quad (3.40)$$

The first-order contribution reads

$$G_{mn\mathbf{kk}'}^{(1)}(\tau) = -\frac{i}{\hbar} \int_{-\infty}^{+\infty} d\tau_1 \left( -i \right) \langle \text{GS}_0 | \mathcal{T} \left[ [\hat{H}_I]_{H_0}(\tau_1) \hat{c}_{m\mathbf{k}}^{H_0}(\tau) \hat{c}_{n\mathbf{k}'}^{H_0\dagger}(0) \right] | \text{GS}_0 \rangle. \quad (3.41)$$

In our case the interaction is the electron–phonon Hamiltonian

$$\hat{H}_{\text{el-ph}} = \frac{1}{\sqrt{N_p}} \sum_{\mathbf{k}, \mathbf{q}} \sum_{mn\nu} g_{mn,\nu}(\mathbf{k}, \mathbf{q}) \hat{c}_{m\mathbf{k}+\mathbf{q}}^\dagger \hat{c}_{n\mathbf{k}} \left( \hat{b}_{\mathbf{q}\nu} + \hat{b}_{-\mathbf{q}\nu}^\dagger \right), \quad (3.42)$$

so that the first-order term involves a single phonon operator inside the expectation value. Since  $\langle \text{GS}_0 | \hat{b} | \text{GS}_0 \rangle = 0$  (and similarly for  $\hat{b}^\dagger$ ), this contribution vanishes for orthogonality of the initial and final state, and the first non-trivial correction arises at second order.

The second-order term is

$$\begin{aligned}
G_{mn\mathbf{k}\mathbf{k}'}^{(2)}(\tau) &= \left(-\frac{i}{\hbar}\right)^2 \frac{1}{2} \int_{-\infty}^{+\infty} d\tau_1 \int_{-\infty}^{+\infty} d\tau_2 (-i) \\
&\quad \times \left\langle \text{GS}_0 \left| \mathcal{T} \left[ \hat{H}_{\text{el-ph}}^{H_0}(\tau_1) \hat{H}_{\text{el-ph}}^{H_0}(\tau_2) \hat{c}_{m\mathbf{k}}^{H_0}(\tau) \hat{c}_{n\mathbf{k}'}^{H_0\dagger}(0) \right] \right| \text{GS}_0 \right\rangle \right. \\
&= \left(-\frac{i}{\hbar}\right)^2 \frac{1}{2} \frac{(-i)}{N_p} \int_{-\infty}^{+\infty} d\tau_1 \int_{-\infty}^{+\infty} d\tau_2 \sum_{\substack{\mathbf{k}_1, \mathbf{q}_1 \\ \mu_1, \lambda_1, \nu_1}} \sum_{\substack{\mathbf{k}_2, \mathbf{q}_2 \\ \mu_2, \lambda_2, \nu_2}} g_{\mu_1 \lambda_1, \nu_1}(\mathbf{k}_1, \mathbf{q}_1) g_{\mu_2 \lambda_2, \nu_2}(\mathbf{k}_2, \mathbf{q}_2) \\
&\quad \times \left\langle \text{GS}_0 \left| \mathcal{T} \left[ \left( \hat{b}_{\mathbf{q}_1 \nu_1}^{H_0}(\tau_1) + \hat{b}_{-\mathbf{q}_1 \nu_1}^{H_0\dagger}(\tau_1) \right) \left( \hat{b}_{\mathbf{q}_2 \nu_2}^{H_0}(\tau_2) + \hat{b}_{-\mathbf{q}_2 \nu_2}^{H_0\dagger}(\tau_2) \right) \right] \right| \text{GS}_0 \right\rangle \right. \\
&\quad \times \left. \left\langle \text{GS}_0 \left| \mathcal{T} \left[ \hat{c}_{\mu_1, \mathbf{k}_1 + \mathbf{q}_1}^{H_0\dagger}(\tau_1) \hat{c}_{\lambda_1, \mathbf{k}_1}^{H_0}(\tau_1) \hat{c}_{\mu_2, \mathbf{k}_2 + \mathbf{q}_2}^{H_0\dagger}(\tau_2) \hat{c}_{\lambda_2, \mathbf{k}_2}^{H_0}(\tau_2) \hat{c}_{m\mathbf{k}}^{H_0}(\tau) \hat{c}_{n\mathbf{k}'}^{H_0\dagger}(0) \right] \right| \text{GS}_0 \right\rangle \right) \tag{3.43}
\end{aligned}$$

which already contains a separated product of many fermionic and bosonic operators. To evaluate these expectations systematically one needs Wick's theorem: it allows one to rewrite time-ordered averages of products of creation and destruction operators as sums of contractions, where the expectation of many operators can be reduced to product of couples of operators, generating the diagrammatic expansion in terms of free electron and free phonon propagators.

### 3.1.5. From Wick Theorem to Feynman Diagrams

The missing ingredient to express the Green function in a diagrammatic expansion is provided by Wick's theorem, which states that the time-ordered product of canonical operators has a non-vanishing expectation value only if it can be fully contracted. In other words, a necessary condition is that the product contains an even number of operators acting on the same subspace (electrons or phonons one). For this reason, only even orders in the perturbative series survive.

The central object introduced by Wick's theorem is the *contraction*. Although its definition is not completely straightforward, in the time-ordered case the contraction of two

operators is a number, corresponding to the expectation value of their time-ordered product on the reference state. For two generic operators  $A_i(t_i)$  and  $A_j(t_j)$  one has

$$\overline{A_i(t_i) A_j(t_j)} = \langle \text{GS} | \mathcal{T} A_i(t_i) A_j(t_j) | \text{GS} \rangle. \quad (3.44)$$

Two operators can be contracted inside an expectation value involving many operators; in this case the resulting number can be extracted, up to a sign accounting for the permutation required to bring the operators next to each other. From this definition it follows that contractions involving two destruction operators or two creation operators vanish, due to the orthogonality of the resulting states. Non-zero contractions are instead obtained for mixed products of creation and destruction operators, which introduce Kronecker deltas in momentum and band (or mode) indices, thus selecting only non-orthogonal contributions.

According to Wick's theorem, any non-vanishing term in the perturbative expansion, such as the second-order contribution ( $n = 2$ ), can be written as a sum of products of pairwise contractions. More generally, the expectation value of a time-ordered product of an even number of operators reduces to the sum of all possible complete contractions, *i.e.* a sum of products of pairwise expectations, closely analogous to the definition of non-interacting Green functions. Products containing an odd number of operators vanish identically.

As a first example, we consider the phonon part of the expectation value. Since phonon operators commute with fermionic ones, the mixed average factorizes, and one obtains

$$\begin{aligned} & \left\langle \text{GS}_0 \left| \mathcal{T} \left[ (\hat{b}_{\mathbf{q}_1\nu_1}^{H_0}(\tau_1) + \hat{b}_{-\mathbf{q}_1\nu_1}^{H_0\dagger}(\tau_1)) (\hat{b}_{\mathbf{q}_2\nu_2}^{H_0}(\tau_2) + \hat{b}_{-\mathbf{q}_2\nu_2}^{H_0\dagger}(\tau_2)) \right] \right| \text{GS}_0 \right\rangle \\ &= \delta_{\mathbf{q}_1, -\mathbf{q}_2} \delta_{\nu_1, \nu_2} D_{\nu_1 \mathbf{q}_1}^{(0)}(\tau_1 - \tau_2), \end{aligned} \quad (3.45)$$

where  $D_{\nu \mathbf{q}}^{(0)}(\tau)$  is the free phonon Green function. The Kronecker deltas enforce momentum and branch conservation at the phonon vertices.

For the electronic part, one explicitly applies Wick's theorem by considering all possible contractions between creation and destruction operators. The elementary time-ordered contractions are

$$\langle \text{GS}_0 | \mathcal{T} \hat{c}_{n\mathbf{k}}^{H_0}(\tau) \hat{c}_{m\mathbf{k}'}^{H_0\dagger}(\tau') | \text{GS}_0 \rangle = -i \delta_{mn} \delta_{\mathbf{k}, \mathbf{k}'} G_{n\mathbf{k}}^{(0)}(\tau - \tau'), \quad (3.46)$$

while contractions between two creation operators or two destruction operators vanish. When operators are evaluated at the same time, contractions give rise to occupation factors,

$$\langle \text{GS}_0 | \hat{c}_{n\mathbf{k}}^{H_0\dagger}(\tau) \hat{c}_{m\mathbf{k}'}^{H_0}(\tau) | \text{GS}_0 \rangle = n_F(\varepsilon_{n\mathbf{k}}), \quad (3.47)$$

where  $n_F$  is the Fermi–Dirac distribution.

Inserting the phonon and electronic contractions into the second-order term (3.43), one finds it as a sum of several contributions corresponding to different pairings of operators, for instance:

$$\begin{aligned} \left\langle \text{GS}_0 \left| \mathcal{T} \left[ \overbrace{\hat{c}_{\mu_1, \mathbf{k}_1 + \mathbf{q}_1}^{H_0 \dagger}(\tau_1)}^{} \overbrace{\hat{c}_{\lambda_1, \mathbf{k}_1}^{H_0}(\tau_1)}^{} \overbrace{\hat{c}_{\mu_2, \mathbf{k}_2 + \mathbf{q}_2}^{H_0 \dagger}(\tau_2)}^{} \overbrace{\hat{c}_{\lambda_2, \mathbf{k}_2}^{H_0}(\tau_2)}^{} \hat{c}_{m\mathbf{k}}^{H_0}(\tau) \hat{c}_{n\mathbf{k}'}^{H_0 \dagger}(0) \right] \right| \text{GS}_0 \right\rangle \\ = i \delta_{\mu_1 m} \delta_{\lambda_1 \mu_2} \delta_{\lambda_2 n} \delta_{\mathbf{k}_1 + \mathbf{q}_1, \mathbf{k}} \delta_{\mathbf{k}_1, \mathbf{k}_2 + \mathbf{q}_2} \delta_{\mathbf{k}_2, \mathbf{k}'} \\ \times G_{m\mathbf{k}}^{(0)}(\tau - \tau_1) G_{m'\mathbf{k}_1}^{(0)}(\tau_1 - \tau_2) G_{n\mathbf{k}'}^{(0)}(\tau_2 - 0). \end{aligned} \quad (3.48)$$

The Kronecker deltas, together with the phonon contraction  $\delta_{\mathbf{q}_1, -\mathbf{q}_2} \delta_{\nu_1 \nu_2}$ , impose momentum conservation at the two vertices and select the allowed band transitions:

$$\mathbf{q}_2 = -\mathbf{q}_1, \quad \mathbf{q} \equiv \mathbf{q}_1, \quad \mathbf{k}_1 = \mathbf{k} + \mathbf{q}, \quad \mathbf{k}_2 = \mathbf{k}, \quad \mathbf{k}' = \mathbf{k}. \quad (3.49a)$$

$$\mu_1 = m, \quad \mu_2 = \lambda_1 \equiv m', \quad \lambda_2 = n. \quad (3.49b)$$

Therefore only the sum over phonon modes ( $\mathbf{q}\nu$ ) and over the intermediate band  $m'$  survives, and the initial and final electronic momenta are equal.

In a similar way one can obtain all possible non-vanishing contractions, and their sum gives the second-order contribution  $G^{(2)}$ . A convenient way to organize and visualize these terms is provided by Feynman diagrams, where straight lines represent free electron propagators  $G^{(0)}$ , wiggly lines represent free phonon propagators  $D^{(0)}$ , and closed fermionic loops correspond to occupation factors  $n_F$ . Moreover, the time-ordering operator  $\mathcal{T}$  ensures the correct chronological ordering of vertices along the fermionic lines.

Referring to the diagrams shown in Fig. 3.3, the terms labelled (b), (d), and (e) vanish because they require the phonon wave vector to assume the value  $\mathbf{q} = 0$ . A phonon with zero momentum corresponds either to a rigid translation of the crystal or to a uniform strain, neither of which is included in the electron–phonon Hamiltonian. Accordingly, sums over phonon momenta are implicitly understood to exclude the  $\mathbf{q} = 0$  contribution. Additionally, it is possible to show that the effect of the denominator in the Reduction Formula is to cancel terms with disconnected part, such as (e) and (k) (linked-cluster theorem). After removing these terms the second-order Green function reduces to the connected self-energy insertion diagram, up to an equivalent relabeling of internal momenta), resulting in an overall prefactor coming from the Dyson expansion (absorbed in

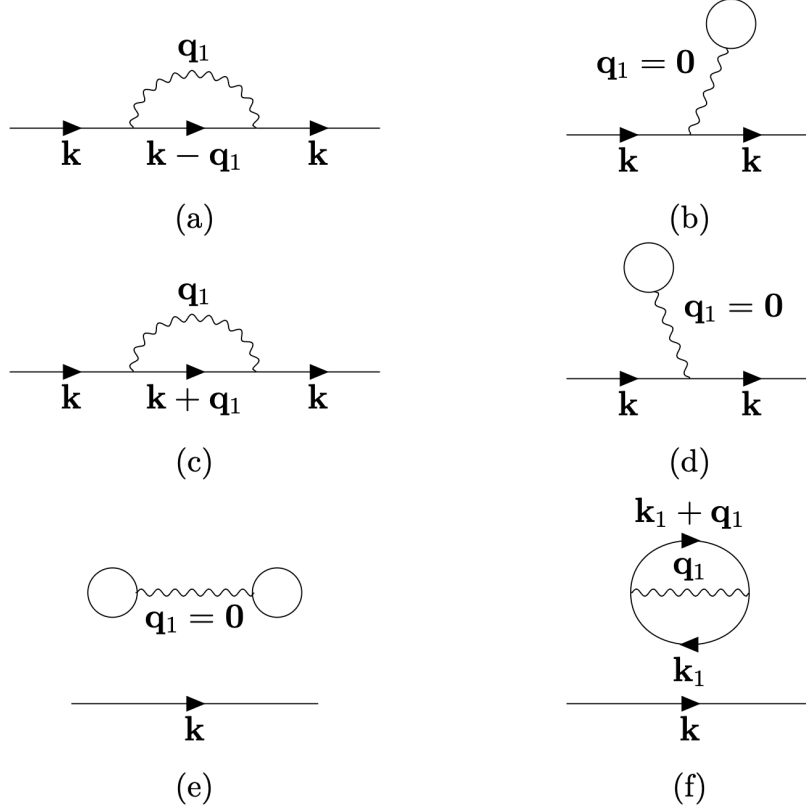


Figure 3.1: Representative diagram topologies contributing to the electron–phonon perturbation series at second order. with initial momentum  $\mathbf{k}$ . Reproduced from S.Ragni Master Thesis Ref. [12].

the Feynman rules):

$$G_{mn\mathbf{k}}^{(2)}(\tau) \propto \frac{1}{N_p} \sum_{\mathbf{q}\nu} \sum_{m'} \int_{-\infty}^{+\infty} d\tau_1 \int_{-\infty}^{+\infty} d\tau_2 g_{mm',\nu}(\mathbf{k} + \mathbf{q}, -\mathbf{q}) g_{m'n,\nu}(\mathbf{k}, \mathbf{q}) \\ \times G_{m\mathbf{k}}^{(0)}(\tau - \tau_1) G_{m',\mathbf{k}+\mathbf{q}}^{(0)}(\tau_1 - \tau_2) D_{\nu\mathbf{q}}^{(0)}(\tau_1 - \tau_2) G_{n\mathbf{k}}^{(0)}(\tau_2 - 0). \quad (3.50)$$

In light of the Feynman diagram interpretation, the first matrix element represents the absorption of a phonon and the corresponding electronic transition  $m'\mathbf{k} + \mathbf{q} \rightarrow m\mathbf{k}$ . It is given by

$$g_{mm',\nu}(\mathbf{k} + \mathbf{q}, -\mathbf{q}) = \langle m\mathbf{k} | \partial_{-\mathbf{q}\nu} V(\mathbf{r}) | m'\mathbf{k} + \mathbf{q} \rangle = \left( \langle m'\mathbf{k} + \mathbf{q} | \partial_{\mathbf{q}\nu} V(\mathbf{r}) | m\mathbf{k} \rangle \right)^*, \quad (3.51)$$

where we have used the property of the displacement potential  $\partial_{-\mathbf{q}\nu} V(\mathbf{r}) = \partial_{\mathbf{q}\nu}^* V(\mathbf{r})$  and subsequently taken the complex conjugate.

The second term instead represents the initial scattering from the electronic state  $n\mathbf{k}$  to  $m'\mathbf{k} + \mathbf{q}$ , and is given by

$$g_{m'n,\nu}(\mathbf{k}, \mathbf{q}) = \langle m'\mathbf{k} + \mathbf{q} | \partial_{\mathbf{q}\nu} V(\mathbf{r}) | n\mathbf{k} \rangle. \quad (3.52)$$

### 3.2. From Perturbation Expansion to Monte Carlo Simulation of the Holstein Model

In the following we specialize the general many-body formalism introduced above to the Holstein polaron problem, which provides the standard setting for diagrammatic Monte Carlo benchmarks. In this framework a single electron propagates on a lattice and interacts locally with a bath of phonons, resulting in the model Hamiltonian reads

$$\hat{H} = \sum_{\mathbf{k}} \varepsilon(\mathbf{k}) \hat{c}_{\mathbf{k}}^\dagger \hat{c}_{\mathbf{k}} + \omega_0 \sum_{\mathbf{q}} \hat{b}_{\mathbf{q}}^\dagger \hat{b}_{\mathbf{q}} + \frac{g}{\sqrt{N}} \sum_{\mathbf{k}, \mathbf{q}} \hat{c}_{\mathbf{k}-\mathbf{q}}^\dagger \hat{c}_{\mathbf{k}} \left( \hat{b}_{\mathbf{q}}^\dagger + \hat{b}_{-\mathbf{q}} \right), \quad (3.53)$$

where  $\varepsilon(\mathbf{k})$  is the electronic dispersion (usually a tight-binding band  $\varepsilon(\mathbf{k}) = -2t \sum_{i=1}^3 \cos(k_i)$ ),  $\omega_0$  is a dispersionless phonon frequency, and  $g$  is a momentum- independent coupling constant.

We work in imaginary time and focus on the single-particle Green function, since its diagrammatic expansion naturally defines the configuration weights sampled by DiagMC. Moreover, in the single-polaron limit (one electron in an otherwise empty band) fermionic occupation factors vanish identically, and the free propagators reduce to simple exponentials for ordered imaginary times:

$$G_{m\mathbf{k}}^{(0)}(\Delta\tau) = -e^{-\varepsilon_{m\mathbf{k}} \Delta\tau}, \quad D_{\nu\mathbf{q}}^{(0)}(\Delta\tau) = -e^{-\omega_{\nu\mathbf{q}} \Delta\tau}. \quad (3.54)$$

While the Holstein model assumes  $\omega_{\nu\mathbf{q}} = \omega_0$  and a constant  $g$ , the same diagrammatic structure can accommodate more realistic inputs, including phonon dispersions and fully momentum- and mode-dependent couplings  $g_{mm'\nu}(\mathbf{k}, \mathbf{q})$ . This is particularly relevant for the present work, where the long-term goal is to incorporate electron–phonon parameters obtained from *ab initio* calculations into the diagrammatic Monte Carlo framework.

The chapter is devoted to explaining how the Green Function perturbation expansion, results in a problem of sampling an infinite- dimensional configuration space of Feynman Diagrams, how it can be sampled in practice and how the resulting chain of diagrams can be used to compute representative observables. The exposition is grounded in the seminal

works of Mishchenko and Prokof'ev [19],[20] and Reference Master Thesis of Ragni [12], with particular attention paid to keeping explicit the full dependence on momentum, phonon mode, and electronic band indices, which is essential for the purposes of the present work.

### 3.2.1. Monte Carlo Integration

From the perturbative expansion it follows that the Green function, not only at second order but in general, thanks to the theorems discussed above, can be expressed as a sum over diagrams. Accordingly, it admits an integral representation of the form

$$G_{mn\mathbf{k}\mathbf{k}'}(\tau) = \sum_{n=0}^{\infty} \sum_{\zeta_n} \int_{-\infty}^{+\infty} d\tau_1 \cdots \int_{-\infty}^{+\infty} d\tau_n D_{\zeta_n}^{(n)}(\tau, \{y\}; \tau_1, \dots, \tau_n), \quad (3.55)$$

where  $\zeta_n$  denotes a set of indices labeling the internal degrees of freedom, such as phonon momenta  $\mathbf{q}$ , phonon modes  $\nu$ , and intermediate electronic band indices  $m'$ , together with a topology index accounting for diagrams of the same order but different structure.

Computing the Green function thus amounts to evaluating this family of high-dimensional integrals for different values of the external variables, namely band indices and crystal momentum, which are collectively denoted by  $\{y\}$  keeping external time  $\tau$  apart, following standard notation in the literature.

A powerful approach to perform this task, at least in relatively simple cases, is provided by **Monte Carlo integration**. The basic idea is that the integral of a function  $f(x)$ , which in our case plays the role of the integrand defining  $G$ , can be interpreted as an average by introducing a probability density  $\rho(x)$ :

$$\int_{-\infty}^{+\infty} dx f(x) = \int_{-\infty}^{+\infty} dx \frac{f(x)}{\rho(x)} \rho(x) = \left\langle \frac{f(x)}{\rho(x)} \right\rangle_{\rho}. \quad (3.56)$$

If one is able to sample the distribution  $\rho(x)$ , *i.e.* to generate a set of random variables  $\{x_i\}$  distributed according to  $\rho$ , one can introduce the *sample mean*, which is an unbiased estimator of the average. In particular, the sample mean is a random variable whose expectation value coincides with the exact average and which, in the limit of a large number of samples, converges to it according to the law of large numbers:

$$\frac{1}{N} \sum_{i=1}^N \frac{f(x_i)}{\rho(x_i)} \xrightarrow[N \rightarrow \infty]{\mathbb{P}} \left\langle \frac{f(x)}{\rho(x)} \right\rangle_{\rho}. \quad (3.57)$$

In order for this procedure to be effective, one must sample correctly the *sample space* of the random variable  $x$  according to the target distribution  $\rho(x)$ . In practice, this means that, for instance, by constructing a histogram of the sampled values, the fraction of samples  $N_i/N_{\text{tot}}$  falling in a bin of width  $\Delta x$  around  $x_i$  approximates  $\rho(x_i) \Delta x$ .

How does this translate to the computation of the Green function? In this case, we can consider a configuration space, whose elements are given by the set of variables  $(n, \zeta_n, \tau_1, \tau_2, \dots)$ , together with the external parameters  $(\tau, \{y\})$ , which unequivocally define a diagram . One can then think of introducing a suitable normalization constant  $C$  in front of Eq. (3.55), allowing one to define a *diagram weight*, formally analogous to a probability density, of a certain configuration:

$$W(n, \zeta_n, \tau_1, \dots, \tau_n; \tau, \{y\}) = \frac{1}{C} D_{\zeta_n}^{(n)}(\tau, \{y\}; \tau_1, \dots, \tau_n) \quad (3.58)$$

Albeit this definition is problematic at this stage<sup>3</sup>, since the normalization constant corresponds to the integral of the Green function itself over all external times, it represents a powerful shift of perspective. If one is indeed able to sample the space of all Feynman diagrams according to such a high-dimensional distribution, the evaluation of integrals depending on the Green function can be reformulated as a stochastic averaging problem.

In this framework, the sampling proceeds through two classes of updates: (i) updates at fixed external parameters, corresponding to a given Green function, and (ii) updates that effectively change the final time (with either fixed or updated external parameters). In close analogy with the simple Monte Carlo example discussed above, physical observables can then be expressed as averages over the sampled diagram configurations.

### 3.2.2. Green Function Histogram

In order to show, through a first example, how one can exploit a Markov chain of diagrams generated according to the diagrammatic weight  $W$ , let us assume for a moment that such a sampling is available. We show that the histogram collecting the statistics of the total imaginary time length  $\tau$  provides an unbiased estimator of the Green function.

Our Markov chain generates a set of  $N$  final times  $\{\tau_i\}_{i=1}^N$  drawn according to the marginal distribution induced by the diagram weights. The histogram of the Green function for  $\tau \in [0, \tau_{\max}]$  is constructed by introducing  $M$  bins of width  $\Delta\tau = \tau_{\max}/M$ , and defining

---

<sup>3</sup>One issue is the non-homogeneous number of integration variables appearing at different diagram orders. This can be formally addressed by viewing all configurations as embedded in a common configuration space, with trivial contributions from variables not present at a given order.

for each bin a *bin counter*

$$B_m = \sum_{i=1}^N \chi_{[t_m - \frac{\Delta\tau}{2}, t_m + \frac{\Delta\tau}{2}]}(\tau_i), \quad (3.59)$$

where  $\chi_I$  is the indicator function of the interval  $I$ .

The average value of the Green function over the  $m$ -th bin is

$$\overline{G(\tau, \{y\})}_m = \frac{1}{\Delta\tau} \int_{t_m - \frac{\Delta\tau}{2}}^{t_m + \frac{\Delta\tau}{2}} d\tau G(\tau, \{y\}) = G(\bar{\tau}_m, \{y\}), \quad \bar{\tau}_m \in \left[ t_m - \frac{\Delta\tau}{2}, t_m + \frac{\Delta\tau}{2} \right], \quad (3.60)$$

where we used the mean value theorem for integrals.

The same quantity can be rewritten by using the indicator function, as an integral over the whole interval:

$$\begin{aligned} \overline{G(\tau, \{y\})}_m &= \frac{1}{\Delta\tau} \int_0^{\tau_{\max}} d\tau \chi_{[t_m - \frac{\Delta\tau}{2}, t_m + \frac{\Delta\tau}{2}]}(\tau) G(\tau, \{y\}) \approx \\ &\approx \frac{C}{\Delta\tau N} \sum_{i=1}^N \chi_{[t_m - \frac{\Delta\tau}{2}, t_m + \frac{\Delta\tau}{2}]}(\tau_i) = \frac{C}{\Delta\tau N} B_m. \end{aligned} \quad (3.61)$$

In the second step we multiplied and divided by  $C$ , and interpreted  $G(\tau, \{y\})/C$  as the marginal probability density of sampling a configuration with external time  $\tau$  (cf. Eq. 3.58). We then used the definition of sample mean and the bin counter.

Comparing the two expressions we obtain

$$G(\bar{\tau}_m, \{y\}) \approx \frac{C}{\Delta\tau N} B_m. \quad (3.62)$$

The remaining element is the normalization constant  $C$ . A convenient estimator can be obtained by introducing a *reference normalization* in which the configuration corresponds to a known contribution, e.g. the non-interacting Green function  $G^{(0)}(\tau, \{y\})$ . We define

$$\begin{aligned} I_0(\{y\}) &\equiv \int_0^{\tau_{\max}} d\tau G^{(0)}(\tau, \{y\}) \\ &= C \int_0^{\tau_{\max}} d\tau \sum_{n=0}^{\infty} \sum_{\zeta_n} \int d\tau_1 \cdots d\tau_n \frac{1}{C} D_{\zeta_n}^{(n)}(\tau, \{y\}; \tau_1, \dots, \tau_n) \delta_{n,0} \\ &= C \langle \delta_{n,0} \rangle, \end{aligned} \quad (3.63)$$

where  $\delta_{n,0}$  denotes the indicator selecting the zero-order contribution. On the other hand, in the Monte Carlo simulation the same expectation value is estimated by the sample mean of the indicator:

$$\langle \delta_{n,0} \rangle \approx \frac{1}{N} \sum_{i=1}^N \delta_{n_i,0} = \frac{N_0}{N}, \quad (3.64)$$

where  $N_0$  is the number of Monte Carlo steps spent at zero order. Equating the two expressions yields the estimator

$$C \approx I_0(\{y\}) \frac{N}{N_0}. \quad (3.65)$$

Plugging this result into Eq. (3.61) finally gives the histogram estimator

$$G(\bar{\tau}_m, \{y\}) \approx \frac{I_0(\{y\})}{\Delta\tau} \frac{B_m}{N_0}. \quad (3.66)$$

The bin counter thus provides an unbiased estimator of the Green function averaged over the corresponding time interval. In the limit  $\Delta\tau \ll 1$ , one obtains a more pointwise estimate of  $G(\tau, \{y\})$ . This, however, comes with an immediate *trade-off*: for a fixed total number of Monte Carlo samples, decreasing the bin width reduces the population of each bin, thereby increasing statistical fluctuations.

This point is particularly important since the bin counter is itself a random variable, which concentrates around its mean value (as implicitly assumed in Eq. (3.61)) only in the large-sample limit. For finite statistics, its variance and the associated error bars depend crucially on the properties of the algorithm generating the diagrammatic Markov chain, such as autocorrelation times and update efficiency, as will be discussed later. This consideration motivates the introduction of improved estimators for the Green function, which can significantly reduce statistical noise.

Furthermore, the procedure leading to the estimation of the normalization constant  $C$  may appear to resolve the apparently puzzling issue of sampling the diagrammatic configuration space. In the discussion above, we have implicitly assumed the ability to sample the diagrammatic distribution and subsequently estimate its normalization. In practice, however, the logic is reversed.

In the following section we introduce the Markov Chain Monte Carlo approach as a constructive method to generate a meaningful sequence of diagrammatic configurations without any prior knowledge of the normalization constant  $C$ . The normalization is then recovered a posteriori from the statistical properties of the generated chain, as illustrated

by the zero-order estimator discussed above.

An explicit example of the histogram estimator is shown in Fig. 3.2, where the binned Green function for the Holstein Model is compared with a direct estimator, together with a characterization of the statistical performance of the simulation.

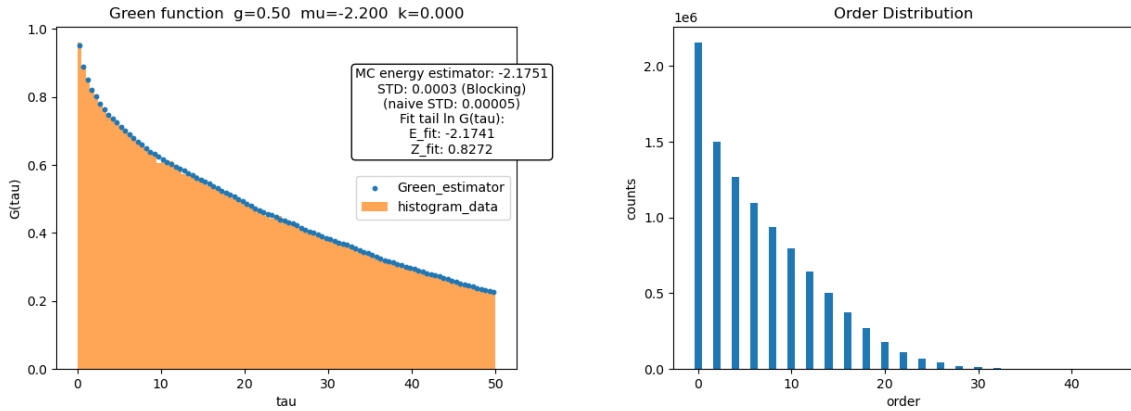


**Figure 3.2:** Example of the Green function histogram method applied to a diagrammatic Monte Carlo simulation for the Holstein Model. The histogram-based estimator is shown together with a direct estimator and a quantitative assessment of statistical uncertainties (left), while the distribution of diagrammatic orders visited during the simulation is reported on the right. Results are in good agreement with previous diagrammatic Monte Carlo studies [12].

### 3.2.3. Markov Chain Monte Carlo and Detailed Balance

The example discussed in the previous section should have highlighted why generating samples of the random vector

$$X = (\tau, \{y\}, n, \zeta_n, \tau_1, \tau_2, \dots),$$

with  $\zeta_n$  representing all possible topologies, phonon momenta, band and mode indices  $(\mathbf{q}_1, \dots, \mathbf{q}_n, \nu_1, \dots, \nu_n, m_1, \dots, m_n)$ , according to the diagram weight in Eq. (3.58), is a highly non-trivial task.

A *Markov chain* provides a constructive procedure to generate a sequence of realizations of the random vector,  $X \rightarrow X_1, \dots, X_j, \dots$ , converging to the representative population defined by the diagram weight, in such a way that the probability of the  $k$ -th step depends

solely on the previous configuration:

$$P(X_j^{(k)} \mid X^{(k-1)}, \dots, X^{(1)}) = P(X_j^{(k)} \mid X^{(k-1)}). \quad (3.67)$$

The generated sequence corresponds to a *random walk* in configuration space, dictated by a transition probability matrix  $P_{ij} = P(X_i \mid X_j)$ . What is crucial is that the structure of the transition matrix ensures **ergodicity**, namely that for sufficiently long “times” the chain is able to visit all configurations ( $\exists n$  such that  $[P^n]_{ij} > 0$  for all  $i, j$  [21]).

From a practical point of view, depending on the initial condition or on the configuration reached at a given step  $k$ , the chain may become temporarily trapped in a region of configuration space characterized by large mutual transition probabilities, while transitions to other regions remain rare events. This aspect is particularly relevant from a numerical perspective: although the process is Markovian, the chain may effectively *stabilize* in certain regions of configuration space, potentially breaking ergodicity or, more generally, introducing correlations between samples and increasing the number of steps required to reach a representative stationary regime.

The existence and the correct form of the stationary distribution are ensured by the condition of **detailed balance**, while its uniqueness is guaranteed, in general, by ergodicity. Detailed balance imposes that, at equilibrium, the total probability flux between any pair of configurations is symmetric, namely that the probability of being in configuration  $j$  and transitioning to  $i$  equals that of being in  $i$  and transitioning to  $j$ :

$$P_{ij}W(X_j) = P_{ji}W(X_i) \quad \Rightarrow \quad \frac{P_{ij}}{P_{ji}} = \frac{W(X_i)}{W(X_j)}. \quad (3.68)$$

A key advantage of this formulation is that transition probabilities can be constructed solely from ratios of diagram weights, without requiring explicit knowledge of their normalization.

A further step toward a practical implementation is provided by the Metropolis–Hastings algorithm, which expresses each transition probability as the product of a **proposal probability**  $T_{ij} > 0$ , suggesting an update from configuration  $j$  to  $i$ , and an **acceptance probability**  $A_{ij}$ . If the proposed update is *rejected*, the current configuration  $X_j$  is repeated in the chain.

In this framework the transition probabilities take the form  $P_{ij} = T_{ij}A_{ij}$ , and inserting this expression into Eq. (3.68) one finds that the acceptance probability must be chosen

as

$$A_{ij} = \min\left(1, \frac{T_{ji}W(X_i)}{T_{ij}W(X_j)}\right). \quad (3.69)$$

The main advantages of this algorithm are, first, that the normalization constant is not required, and second, that the ratio of two diagram weights can often be evaluated in a simple analytical form, as will be shown later. The proposal distribution  $T$  can in principle be chosen arbitrarily, provided it is easy to sample from; even uniform proposals are admissible. However, some care is required: in practice it is desirable for the proposal distribution to resemble the target weight  $W$  as closely as possible, in order to achieve a high acceptance rate. In the ideal limit  $T = W$ , all proposed updates are accepted and the algorithm reduces to direct sampling.

### 3.2.4. Blocking Analysis

Monte Carlo estimators obtained from diagrammatic sampling are unbiased estimators of the relevant observables. Nevertheless, for a finite number of samples  $N$ , they are affected by statistical fluctuations, whose standard deviation vanishes only in the limit  $N \rightarrow \infty$ .

Given a sequence of measurements  $\{O_i\}_{i=1}^N$  generated by a Markov Chain Monte Carlo process, successive samples are in general correlated. Treating the  $O_i$  as independent random variables therefore leads to an underestimation of the statistical error. To account for these correlations we employ the **blocking analysis**.

For a given block size  $b$ , the data are partitioned into  $N_b = \lfloor N/b \rfloor$  consecutive blocks, and block averages are defined as

$$\bar{O}_k^{(b)} = \frac{1}{b} \sum_{i=(k-1)b+1}^{kb} O_i, \quad k = 1, \dots, N_b. \quad (3.70)$$

The variance of the block-averaged data is then

$$\sigma_b^2 = \frac{1}{N_b - 1} \sum_{k=1}^{N_b} \left( \bar{O}_k^{(b)} - \langle \bar{O}^{(b)} \rangle \right)^2, \quad \langle \bar{O}^{(b)} \rangle = \frac{1}{N_b} \sum_{k=1}^{N_b} \bar{O}_k^{(b)}. \quad (3.71)$$

As the block size  $b$  is increased, correlations between different blocks are progressively reduced. For block sizes much larger than the autocorrelation time,  $\sigma_b$  converges to a plateau, which provides a reliable estimate of the true statistical error of the Monte Carlo estimator. The location of this plateau also yields an estimate of the correlation time of the Markov chain.

An example of this procedure, applied to the energy estimator obtained from diagrammatic Monte Carlo sampling, is shown in the insert Fig. 3.2. The comparison with the naive variance estimate illustrates that neglecting correlations may lead to an underestimation of the statistical error by up to one/two order of magnitude.

### 3.3. Momentum and Band-Resolved Implementation

The many-body formalism introduced above, together with the definition of the Diagrammatic Monte Carlo algorithm, is now completed by deriving the explicit expression of the diagram ratio entering the acceptance probability in Eq. 3.69, or equivalently an algorithmic procedure. This quantity determines the weight of configuration updates and therefore constitutes the core ingredient of the Monte Carlo procedure.

In this section we derive the ratio explicitly, retaining the full momentum and quantum-number dependence of all propagators and interaction vertices. Following the derivation in [20] we introduce two estimators, an improved one for the Green Function and a second for Polaron Ground State Energy. Our goal is to construct an algorithm capable of handling general momentum-resolved electron–phonon couplings. Technical details of the code implementation are provided in Appendix B.

#### 3.3.1. Electron–Phonon Diagram Anatomy

Before diving into the precise diagram updates employed in the MCMC algorithm, it is useful to briefly reflect on the structure of the Feynman diagrams under examination, in particular when a full momentum dependence is retained. Considering a perturbative order  $2n$ , the corresponding diagram is composed of  $n$  free phonon propagators,  $2n + 1$  free electron propagators, and  $2n$  electron–phonon vertices. Among these vertices,  $n$  correspond to phonon creation events and  $n$  to phonon absorption events. Each creation and absorption pair is related by the momentum carried by the phonon, while the two events may occur at distant imaginary times, giving rise to an exponential decay in the diagram weight governed by the phonon propagator. These events can be interleaved with other vertices, as illustrated in Fig. 3.3.

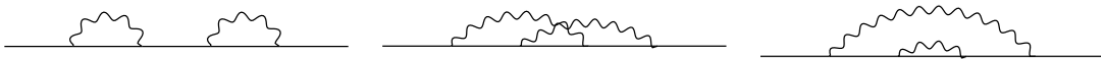


**Figure 3.3:** Examples of different diagram topologies contributing to the Green function at fixed perturbative order.

The general form of the electron–phonon creation and annihilation vertices is summarized in Fig. 3.4. For the initial and final vertices, constraints on the external band indices and crystal momentum must be enforced if one wishes to keep them fixed. If instead the algorithm is allowed to explore different configurations of the external parameters  $\{y\}$ , these constraints can be relaxed.

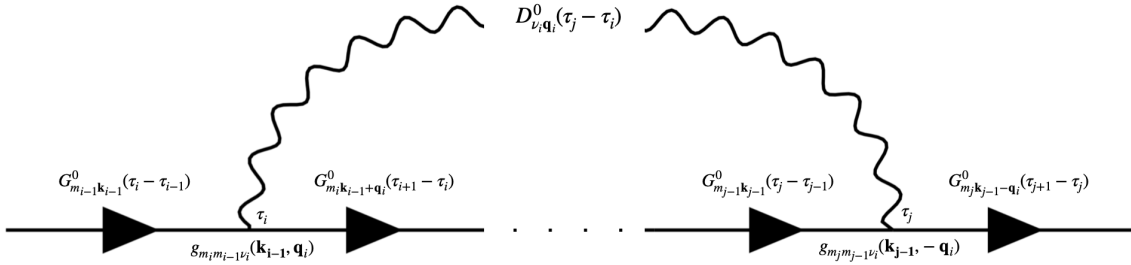


**Figure 3.4:** Schematic representation of electron–phonon vertices in imaginary time. Straight lines denote free electron propagators  $G^{(0)}$ , wiggly lines denote free phonon propagators  $D^{(0)}$ , and black triangles indicate electron–phonon interaction vertices with explicit momentum and band dependence.

The full diagram is specified by a configuration

$$\mathcal{C} = \{\gamma, \tau_1, \dots, \tau_n; \mathbf{q}_1, \dots, \mathbf{q}_n; \nu_1, \dots, \nu_n; m_1, \dots, m_{n-1}; \mathbf{k}_1, \dots, \mathbf{k}_n\},$$

where  $\gamma$  denotes the diagram topology, together with the external parameters  $(m, n, \mathbf{k}, \tau)$ . The corresponding diagram weight factorizes as

$$\begin{aligned} \mathcal{D}(\mathcal{C}) \propto & \left[ \prod_{\ell=0}^{2n} G_{m_\ell \mathbf{k}_\ell}^{(0)}(\tau_{\ell+1} - \tau_\ell) \right] \left[ \prod_{i=1}^n D_{\nu_i \mathbf{q}_i}^{(0)}(\tau_i - \tau_{\pi(i)}) \right] \\ & \times \left[ \prod_{i=1}^n g_{m_i m_{i-1} \nu_i}(\mathbf{k}_{i-1}, \mathbf{q}_i) g_{m_{\pi(i)} m_{\pi(i)-1} \nu_{\pi(i)}}(\mathbf{k}_{\pi(i)-1}, -\mathbf{q}_{\pi(i)}) \right], \end{aligned} \quad (3.72)$$

where  $\pi(i)$  identifies the vertex paired with  $i$  by a phonon line. And considering ordered imaginary time, :

$$G_{m_\ell \mathbf{k}_\ell}^{(0)}(\tau_{\ell+1} - \tau_\ell) = -ie^{-\varepsilon_{n_\ell \mathbf{k}_\ell}(\tau_{\ell+1} - \tau_\ell)} \quad D_{\nu_i \mathbf{q}_i}^{(0)}(\tau_i - \tau_{\pi(i)}) = -ie^{-\omega_{\nu_i \mathbf{q}_i}(\tau_i - \tau_{\pi(i)})}$$

An important aspect for the implementation is that, by storing all vertices together with the information on the preceding and following electron propagators, and by keeping

track of the pairing index  $j = \pi(i)$  that links phonon creation and annihilation vertices, the full diagram weight can be reconstructed efficiently. This representation enables the implementation of all Monte Carlo updates discussed in Appendix B.

A subtle aspect of the Metropolis–Hastings algorithm concerns its practical implementation, in particular the construction of the proposal step. In general, a proposal consists in suggesting a new configuration, which may correspond to a change in diagram topology, perturbative order, internal vertex positions, their associated momenta or imaginary times, as well as the final propagation time or external parameters.

Given the complex internal structure of each diagram in Eq. (3.72), it is convenient to introduce different types of updates, each modifying a specific aspect of the diagram configuration. These updates can be selected at random, possibly with assigned probabilities. Their choice is directly related to the ergodicity of the algorithm and to the set of configurations that can be effectively explored.

Here we propose a minimal set of four updates that ensures sufficient exploration of the configuration space, including diagrams of different order, topology, and final imaginary time:

- **Stretch Diagram:** all internal and external times are rescaled by a common factor  $\alpha = \bar{\tau}/\tau$ .
- **Change Final Time:** only the length of the last electron propagator is modified.
- **Add Phonon Line:** a new pair of phonon creation and annihilation vertices is inserted into the diagram.
- **Remove Phonon Line:** an existing phonon line is removed, decreasing the perturbative order of the diagram.

Many extensions of this basic set are possible and can be used to improve the efficiency of the algorithm, such as updates that modify only the momentum carried by a given vertex or that change the diagram topology while keeping the order fixed.

In the following, we assume a uniform probability of selecting one of the four updates listed above. For each update, a specific proposal distribution is defined for the parameters involved. Once the ratio of diagram weights can be computed explicitly or defining an algorithm, the corresponding Metropolis acceptance probability follows directly.

**Stretch Diagram.** A new final time  $\bar{\tau}$  is sampled uniformly from the working interval  $\bar{\tau} \in [0, \tau_{\max}]$ , and the scaling factor  $\alpha = \bar{\tau}/\tau$  is introduced. Since the proposal probabilities

in the forward and backward directions are equal,  $T_{ij} = T_{ji} = 1/\tau_{\max}$ , the acceptance probability is determined solely by the ratio of diagram weights.

From the diagrammatic structure one finds

$$A = \min \left[ 1, \exp \left\{ (1 - \alpha) \left( \sum_{\ell=0}^{2n} \varepsilon_{m_\ell \mathbf{k}_\ell} (\tau_{\ell+1} - \tau_\ell) + \sum_{i=1}^n \omega_{\nu_i \mathbf{q}_i} (\tau_i - \tau_{\pi(i)}) \right) \right\} \right]. \quad (3.73)$$

**Change Final Time.** A new final time  $\bar{\tau}$  is sampled uniformly in the interval  $\bar{\tau} \in [\tau_{2n}, \tau_{\max}]$ , where  $\tau_{2n}$  denotes the time of the last internal vertex. Also in this case the proposal probabilities satisfy  $T_{ij} = T_{ji} = 1/(\tau_{\max} - \tau_{2n})$ .

The acceptance probability follows directly from the change in the last electron propagator,

$$A = \min[1, \exp\{-\varepsilon_{m\mathbf{k}}(\bar{\tau} - \tau)\}]. \quad (3.74)$$

### Add/Remove Phonon Line Transition Probabilities

In this class of updates, the role of the transition probability is particularly important, since the addition and removal of a phonon line are mutually inverse processes and must therefore be treated consistently in order to satisfy detailed balance. If one wishes to remove a phonon line from a diagram of order  $2n$ , the update consists in selecting one of the  $n$  existing phonon lines uniformly at random, which gives the proposal probability

$$T_{\text{rem}} = \frac{1}{n}. \quad (3.75)$$

Conversely, when proposing to add a phonon line, several internal variables must be sampled. In the present implementation, the phonon mode  $\nu$ , the electron band index after the creation vertex, and the electron band index after the annihilation vertex are sampled uniformly from the available bands. The phonon momentum  $\mathbf{q}$  is sampled uniformly over the chosen momentum grid. The creation time  $\tau_i$  is drawn uniformly in the interval  $[0, \tau_{\max}]$ , while the annihilation time  $\tau_f > \tau_i$  is sampled from an exponential distribution. This choice is motivated by the exponential decay of the free phonon propagator  $D^{(0)}$  in imaginary time and leads to a significant improvement in the acceptance rate. Introducing a reference decay rate  $\omega_d$ , the proposal probability for adding a phonon line reads

$$T_{\text{add}} = \frac{1}{N_\nu} \frac{1}{N_{\text{bands}}^2} \frac{1}{\tau_{\max}} \frac{e^{-(\tau_f - \tau_i)\omega_d}}{K}, \quad (3.76)$$

where  $K$  is the normalization constant of the exponential distribution, which can be evaluated analytically at each Monte Carlo step.

### Add/Remove Diagram Weight Ratio

In the momentum-dependent and inter-band formulation, the addition of a phonon line constitutes a highly non-local update in the diagram structure. Inserting a phonon creation vertex at imaginary time  $\tau_i$  and the corresponding annihilation vertex at  $\tau_f > \tau_i$  modifies not only the local vertex structure, but also all electron propagators lying between the two vertices. According to our convention, the emission of a phonon with momentum  $\mathbf{q}$  changes the electron momentum after the creation vertex, and this momentum shift propagates along the electron line until the annihilation vertex, where the original momentum is restored. As a consequence, all electron propagators and interaction vertices between  $\tau_I$  and  $\tau_F$  are affected by the update, through a uniform shift of their electron momentum arguments by  $\mathbf{q}$ .

In the inter-band case, the band indices require additional care. At each newly inserted vertex, the incoming band index is fixed by the preceding electron propagator, while the outgoing band index is sampled as part of the update<sup>4</sup>. Consequently, the band index of the electron propagator immediately following the creation vertex is changed, as well as the band index of the propagator following the annihilation vertex. Any additional vertices lying between  $\tau_i$  and  $\tau_f$  inherit the updated momentum structure through the modified electron propagators.

Two further contributions arise at the boundaries of the update, since the insertion of the creation and annihilation vertices splits the electron propagators containing  $\tau_I$  and  $\tau_F$  into two segments, which must be treated separately in the evaluation of the diagram weight. Within this construction, the diagram weight ratio is obtained by explicitly traversing the diagram between  $\tau_I$  and  $\tau_F$  and collecting all changes in electron propagators, phonon propagators, and electron–phonon vertex factors induced by the update. In appendix B we express by formula the analytical details of this update.

For these reasons, the diagram weight ratio  $W_{\text{add}}/W$  is not written as a closed analytical expression. Instead, it is computed constructively by traversing the diagram between  $\tau_I$  and  $\tau_F$  and collecting all local changes induced by the update, including the phonon propagator, the two electron–phonon vertex factors, the modified electron propagators

---

<sup>4</sup>If the annihilation vertex is the last vertex in the diagram, the final band index may instead be fixed to match the external Green function under consideration. Moreover, if no other vertices lie between the creation and annihilation vertices, the incoming band index at the annihilation vertex coincides with the outgoing band index of the creation vertex.

along the interval, and the two boundary contributions.

A more detailed description is given in Appendix B; we omit it here to avoid overloading the presentation. What is important to stress is that updates of this kind, performed millions of times during a DiagMC simulation, require the evaluation of new electron energies, phonon frequencies, and—most critically—the electron–phonon coupling. These quantities must be computed for momentum combinations that cannot be anticipated *a priori*, but instead arise dynamically during the Markov chain evolution and therefore need to be evaluated on demand.

The reverse update, namely the removal of a phonon line, undoes exactly the same set of modifications. In this case the diagram is traversed between the two vertices connected by the selected phonon line, and all momentum- and band-dependent changes are reverted. Since the removal update does not require sampling new internal variables, its proposal probability depends only on the number of available phonon lines. The Metropolis–Hastings acceptance probability is finally obtained by combining the diagram weight ratio with the ratio of proposal probabilities. In particular, when adding a phonon line to a diagram of order  $2n$ , the reverse move removes a phonon line from a diagram of order  $2(n + 1)$ , yielding the proposal probability

$$T_{\text{rem}} = \frac{1}{n + 1}, \quad (3.77)$$

and the corresponding factor  $T_{\text{rem}}/T_{\text{add}}$  entering the acceptance ratio.

### 3.3.2. Improved Estimator for the Green Function

The histogram estimator discussed above suffers from a systematic trade-off between time resolution and statistical noise due to the finite bin width  $\Delta\tau$ . This limitation can be removed by constructing an *exact* estimator for the Green function.

Let  $G(\tau, \{y\})$  admit the diagrammatic expansion

$$G(\tau, \{y\}) = \sum_{n, \zeta_n} \int d\boldsymbol{\tau}_n D_{\zeta_n}^{(n)}(\tau, \{y\}; \boldsymbol{\tau}_n), \quad (3.78)$$

and consider a Markov chain sampling diagram configurations  $(n, \zeta_n, \boldsymbol{\tau}_n, \tau)$  with probability density proportional to  $D_{\zeta_n}^{(n)}(\tau, \{y\}; \boldsymbol{\tau}_n)$ .

For a fixed target time  $\tau_0$ , we define the estimator

$$\mathcal{G}_{\tau_0} = \begin{cases} \frac{D_{\zeta_n}^{(n)}(\tau_0, \{y\}; \boldsymbol{\tau}_n)}{D_{\zeta_n}^{(n)}(\tau, \{y\}; \boldsymbol{\tau}_n)} \frac{1}{|\mathcal{I}_{\tau_0}|}, & \tau \in \mathcal{I}_{\tau_0}, \\ 0, & \text{otherwise,} \end{cases} \quad (3.79)$$

where  $\mathcal{I}_{\tau_0}$  is a finite interval containing  $\tau_0$  over which the diagram is well defined. The normalization factor  $|\mathcal{I}_{\tau_0}|$  compensates for the uniform integration over  $\tau$ .

The unbiased nature of the estimator follows directly from the definition of the Monte Carlo average. Indeed, taking the expectation value of Eq. (3.79) with respect to the sampling weight  $W(\mathcal{C}) = D_{\zeta_n}^{(n)}(\tau, \{y\}; \boldsymbol{\tau}_n)/C$ , one finds

$$\begin{aligned} \langle \mathcal{G}_{\tau_0} \rangle_{\text{MC}} &= \sum_{n, \zeta_n} \int d\boldsymbol{\tau}_n \int d\tau \frac{1}{C} D_{\zeta_n}^{(n)}(\tau, \{y\}; \boldsymbol{\tau}_n) \mathcal{G}_{\tau_0} \\ &= \frac{1}{C |\mathcal{I}_{\tau_0}|} \sum_{n, \zeta_n} \int d\boldsymbol{\tau}_n \int_{\mathcal{I}_{\tau_0}} d\tau D_{\zeta_n}^{(n)}(\tau_0, \{y\}; \boldsymbol{\tau}_n) \\ &= \frac{1}{C} \sum_{n, \zeta_n} \int d\boldsymbol{\tau}_n D_{\zeta_n}^{(n)}(\tau_0, \{y\}; \boldsymbol{\tau}_n) = C G(\tau_0, \{y\}), \end{aligned} \quad (3.80)$$

where in the second step the ratio of diagrammatic weights cancels the explicit  $\tau$ -dependence, and the integration over  $\tau$  simply yields the factor  $|\mathcal{I}_{\tau_0}|$ .

with the same normalization constant  $C$  introduced in the histogram approach. Therefore, once  $C$  is estimated (e.g. via the zero-order sector), Eq. (3.79) provides a pointwise, unbiased estimator of the Green function, free of binning errors.

In practice, at each MCMC step, this estimator can be interpreted as a controlled reweighting in the current external time variable, used to collect statistics of the Green Function estimator for other times in the interval  $\mathcal{I}_{\tau_0}$  around the current one. While efficient for nearby values of  $\tau$ , it becomes unreliable if configurations typical at  $\tau$  carry exponentially small weight at  $\tau_0$ . In such cases, the variance grows rapidly and the histogram estimator remains preferable.

### 3.3.3. Energy Estimator

Information about the ground-state properties of the polaron is encoded in the long-imaginary-time behavior of the Green function, as shown by *Mishchenko et al.* in [20]. In

particular, for large  $\tau$ , the propagator behaves as

$$G(\tau, \mathbf{k}) \sim Z_{\mathbf{k}} e^{-E_0(\mathbf{k})\tau} \quad (3.81)$$

so that the ground-state energy can be extracted from the logarithmic derivative

$$E(\mathbf{k}) = - \lim_{\tau \rightarrow \infty} \frac{\partial}{\partial \tau} \ln G(\tau, \mathbf{k}). \quad (3.82)$$

Rather than computing numerical derivatives of noisy Monte Carlo data, it is more convenient to construct a direct estimator. Following the approach of the reference literature, one considers the ratio

$$\frac{G(\mathbf{k}, (1 + \lambda)\tau)}{G(\mathbf{k}, \tau)} \xrightarrow{\tau \rightarrow \infty} e^{-E(\mathbf{k})\lambda\tau} \quad (3.83)$$

and expands for small  $\lambda$ . Comparing this expansion with the corresponding ratio of diagram weights leads to the estimator

$$E(\mathbf{k}) = \left\langle -\frac{2n}{\tau} + \sum_i \varepsilon(\mathbf{k}_i) \frac{\Delta\tau_i}{\tau} + \sum_j \omega(\mathbf{q}_j) \frac{\Delta\tau_j}{\tau} \right\rangle_{\text{MC}} \quad (3.84)$$

where  $n$  is the number of phonon propagators in the current diagram,  $\Delta\tau_i$  are the electron propagation lengths, and  $\Delta\tau_j$  are the phonon propagation lengths.

Since it depends only on quantities already stored in the diagram configuration, the Monte Carlo average can be evaluated with negligible computational overhead at each step of the simulation.

### 3.3.4. Results: Breathing Electron–Phonon Coupling

In order to benchmark the momentum-dependent implementation introduced above, we consider a one-dimensional breathing-mode extension of the Holstein Hamiltonian. Compared to the standard Holstein model, the only modification consists in introducing a coupling that depends explicitly on the phonon momentum  $q$ , while remaining independent of the electronic momentum, band index, and phonon branch. The interaction vertex takes the form

$$g(q) = -2ig \sin\left(\frac{qa}{2}\right) \quad (3.85)$$

where  $q$  is sampled on a regular Brillouin-zone grid,  $a$  is the lattice spacing, and we consider a single tight-binding electronic band with dispersion  $\varepsilon_k = -2t \cos(ka)$  and a dispersionless phonon mode of frequency  $\omega_0$ .

Physically, this model describes a situation in which the electron couples to relative displacements of neighboring lattice sites, rather than to an on-site distortion. In real space the interaction is proportional to the difference of adjacent ionic positions, which in momentum space gives rise to the characteristic  $\sin(qa/2)$  dependence. As a consequence, long-wavelength phonons couple weakly ( $q \rightarrow 0$ ), while short-wavelength modes near the Brillouin-zone boundary dominate the interaction. It represents a good test for a momentum-resolved implementation. Semi-analytical results for the ground-state energy are available within the Momentum Average (MA) approximation [22, 23], which we use as a benchmark.

From the general diagram anatomy discussed previously, each phonon line connects a creation and an annihilation vertex, contributing a factor  $g(q)g(-q) = |g(q)|^2$ . For this reason, in the present single-band case, the complex phase of  $g(q)$  does not affect the diagram weight, and we may equivalently use

$$|g(q)| = 2g \left| \sin\left(\frac{qa}{2}\right) \right|. \quad (3.86)$$

This simplification follows directly from the diagram structure and is typical for band-independent or purely intraband couplings. In multi-band problems, however, the full complex matrix elements must be retained, and their phase structure can contribute to a sign problem.

We define the dimensionless coupling strength as

$$\lambda = \frac{g^2}{\omega_0 t}, \quad (3.87)$$

and set  $t = 1$  and  $\omega_0/t = 0.5$  throughout.

As shown in Fig. 3.5, the inclusion of the momentum-dependent coupling leads to a significant deviation from the phase-independent ( $a = 0$ ) Holstein case. The DiagMC results are in very good agreement with the Momentum Average calculations over the full range of couplings considered, providing a first nontrivial benchmark of the momentum-resolved implementation. This agreement confirms that the algorithm correctly accounts for momentum-dependent vertices and propagators, at least in the single-band case where no additional phase-induced sign problem is present.

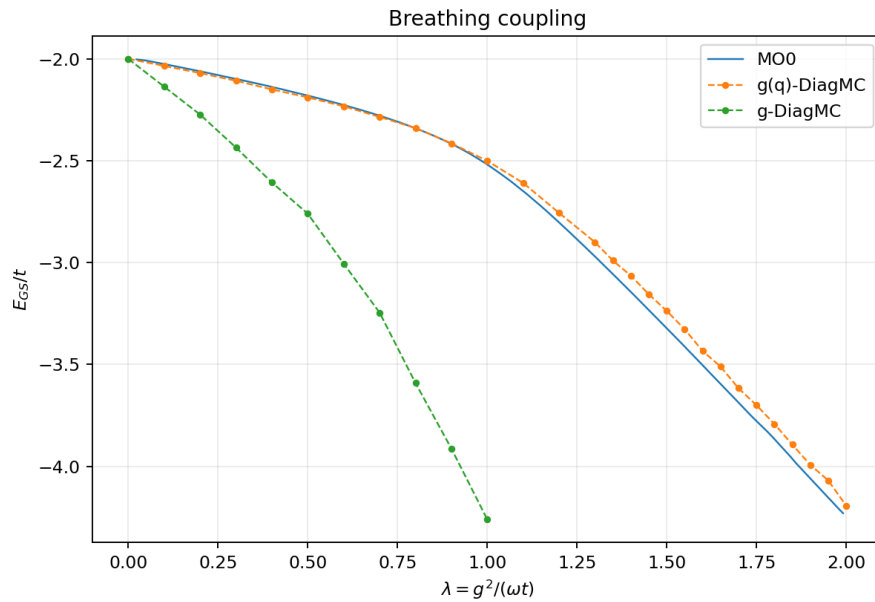


Figure 3.5: Ground-state energy  $E_{GS}/t$  as a function of  $\lambda = g^2/(\omega_0 t)$  for the 1D breathing-mode model. The diagrammatic Monte Carlo results with full momentum-dependent coupling (orange) are compared with Momentum Average (MA(0)) calculations (blue). For reference, the phase-independent ( $a = 0$ ) Holstein limit is shown in green. Parameters:  $t = 1$ ,  $\omega_0/t = 0.5$ .



# 4 | Tensor Decomposition and Interpolation

## 4.1. Generalized Fourier Interpolation

The introduction of Diagrammatic Monte Carlo (DMC) in the previous chapter highlights a critical requirement: the algorithm performs a *continuous sampling* of imaginary time and, crucially, of momentum variables at the resolution imposed by Brillouin-zone quantization (Eq. 1.14). As a consequence, realistic simulations of materials require access to the electronic dispersion  $\varepsilon_n(\mathbf{k})$ , phonon frequencies  $\omega_\nu(\mathbf{q})$ , and electron–phonon coupling matrix elements  $g_{mn,\nu}(\mathbf{k}, \mathbf{q})$  on momentum grids that are far denser than those that can be computed and stored directly within first-principles calculations.

Although Density Functional Theory (DFT) provides a reliable route to compute these quantities, the computational cost rapidly becomes prohibitive when dense sampling of the Brillouin zone is required, especially for phonons and electron–phonon interactions. The only viable strategy is therefore to *interpolate* these quantities starting from a coarse grid. However, this approach introduces two fundamental issues:

- 1. Smoothness and gauge issues.** As raw outputs of DFT calculations, electron–phonon matrix elements are not smooth functions of momentum. Due to the arbitrary gauge of Bloch states, both their amplitude and phase may exhibit rapid variations or discontinuities, which make direct interpolation unreliable. This is illustrated in Fig. 4.1, where the phase of the coupling varies strongly along otherwise smooth phonon branches. From a real-space/momentum Fourier-duality perspective, this lack of smoothness in reciprocal space implies slowly decaying, long-range components in real space, rendering direct interpolation inefficient unless a representation with fast real-space decay is introduced.
- 2. Memory–performance bottleneck.** Storing electron–phonon matrix elements on a grid dense enough to reach the resolution required by DMC would demand

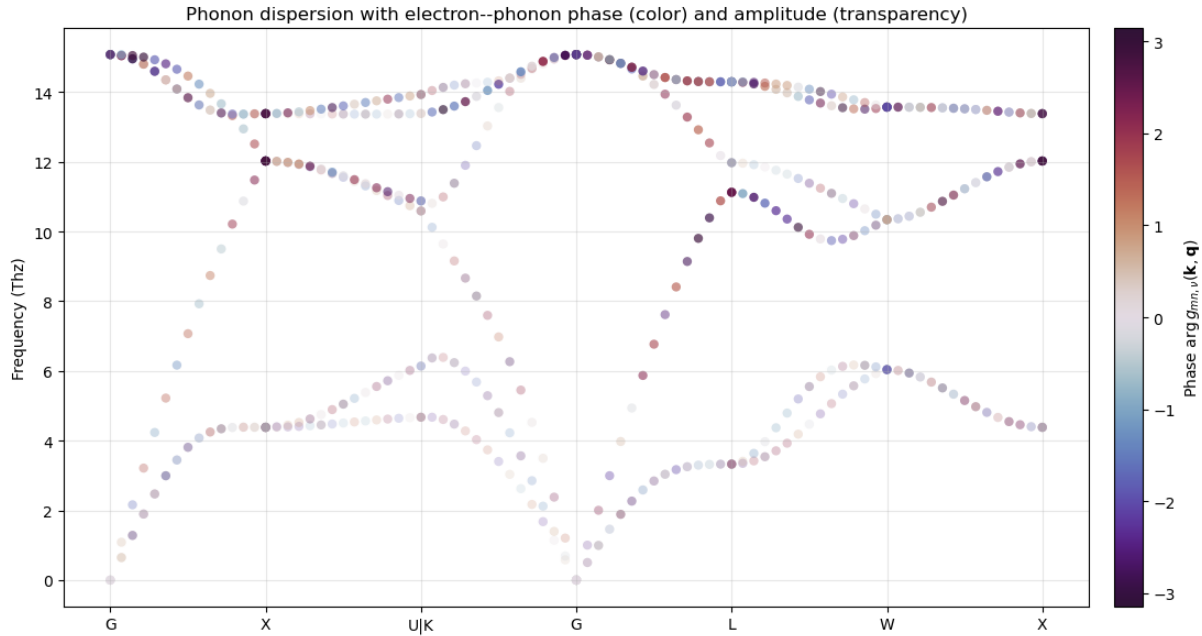


Figure 4.1: Phonon dispersion along high-symmetry directions, where each point is colored according to the phase  $\arg[g_{mn,\nu}(\mathbf{k}, \mathbf{q})]$  of the electron–phonon coupling and rendered with a transparency proportional to its magnitude  $|g_{mn,\nu}(\mathbf{k}, \mathbf{q})|$ .

memory on the order of terabytes<sup>1</sup>. Conversely, evaluating these matrix elements *on-the-fly* during Monte Carlo updates would introduce a severe computational overhead, becoming the dominant bottleneck of the algorithm.

To resolve these issues, this chapter shows how a generalized Fourier transformation based on **Wannier functions** maps electronic, phononic, and electron–phonon quantities to a localized real-space representation. By exploiting the rapid spatial decay of the corresponding Fourier coefficients, accurate and smooth interpolation becomes possible, as established in Refs. [24, 25].

At this stage, the remaining critical limitation is the cost of evaluating interpolated matrix elements during the Monte Carlo sampling. Even within a Wannier representation, a single Add/Remove update may require the evaluation of many electron–phonon vertices. Recently, a compression strategy based on matrix factorization was proposed in Ref. [26] and successfully applied to first-principles DiagMC simulations in Ref. [27]. In this work, we follow the same general philosophy, but adapt it to a different first-principles ecosystem (DFT calculations performed entirely in VASP or in Quantum ESPRESSO and interpolation

<sup>1</sup>For a Born–von Kármán supercell of linear size  $L$ , the momentum spacing is  $\Delta q = 2\pi/L$ , giving  $N_q \simeq (L/a)^3$  points in the first Brillouin zone. For  $L = 100 \text{ \AA}$  and  $a = 4 \text{ \AA}$ ,  $N_q \simeq 1.6 \times 10^4$ . Taking  $N_k \simeq N_q$ ,  $N_b = 10$ , and  $N_\nu = 10$ , storing complex  $g_{mn,\nu}(\mathbf{k}, \mathbf{q})$  requires  $\sim 2.6 \times 10^{12}$  numbers, corresponding to  $\sim 40 \text{ TB}$  in double precision.

via EPW[28] plus Wannier90[29]) and reformulate the problem from a *tensorial* perspective.

By explicitly treating the electron–phonon coupling as a high-rank tensor, we introduce a tensor-based compression strategy and propose an alternative Tucker decomposition, which naturally generalizes matrix-based approaches and allows for a more efficient separation of electronic and phonons degrees of freedom. This formulation further accelerates the evaluation of matrix elements during the Monte Carlo sampling, keeping low memory requirements.

#### 4.1.1. Wannier Function

In chapter 1 we have introduced the Bloch Representation of the electron wavefunction:

$$\psi_{n\mathbf{k}}(\mathbf{r}) = \langle \mathbf{r} | n\mathbf{k} \rangle = e^{i\mathbf{k}\cdot\mathbf{r}} u_{n\mathbf{k}}(\mathbf{r}) \quad (4.1)$$

which is generally delocalized over different atomic sites. We can introduce the Fourier transform of the state to a set of  $N_e$  vectors of the *Bravais Lattice* in real space as:

$$|n\mathbf{R}_e\rangle = \sum_{\mathbf{k}} e^{-i\mathbf{k}\cdot\mathbf{R}_e} |n\mathbf{k}\rangle \quad (4.2)$$

Where the usual duality between direct and reciprocal space fixes the set of vectors we are considering, and most importantly we know from Fourier duality that coefficients corresponding to large  $\mathbf{R}_e$  will result in rapid oscillation in momentum space.

Once represented in the position basis  $w_n(\mathbf{r} - \mathbf{R}_e) = \langle \mathbf{r} | n\mathbf{R}_e \rangle$ , the coefficients represent the so-called **Wannier Functions**, named after the Swiss physicist who first introduced them as an alternative to Bloch States. While the latter are in general delocalized over many ionic sites, Wannier Functions are localized around the site  $\mathbf{R}_e$ , and are orthonormal and transform into each other through the application of translational operations. They are not in general Hamiltonian eigenstates, but for a given band, they represent a complete orthonormal basis of the band subspace.

More precisely, the transformation as highlighted before is mathematically well defined if the band is isolated; if instead it mixes with other bands, in this case one has to consider a subset of  $J$  bands that are isolated, namely they can be degenerate and mix within the set but they have to be separated above and below by some energy gap, and they define an invariant subspace of the Hilbert Space. In this case one can still define Wannier Functions with the properties mentioned above introducing a generic rotation of the band

indices, through an  $N_{Wannier} \times N_{Bloch}$  matrix  $U_{nj}(\mathbf{k})$  which is orthogonal:

$$U(\mathbf{k})U^\dagger(\mathbf{k}) = \mathbb{I} \quad (4.3)$$

In this case one defines a generalized version of the Fourier Transformation mentioned above which is not simply a unitary transformation between states corresponding to a single band but between two subspaces of bands, and in general now the Wannier Band index  $j$  has not a real physical interpretation:

$$|j\mathbf{R}_e\rangle = \sum_{\mathbf{k}n} e^{-i\mathbf{k}\cdot\mathbf{R}_e} U_{nj}(\mathbf{k}) |n\mathbf{k}\rangle \quad (4.4a)$$

$$|n\mathbf{k}\rangle = \frac{1}{N_e} \sum_{j\mathbf{R}_e} e^{i\mathbf{k}\cdot\mathbf{R}_e} U_{jn}^\dagger(\mathbf{k}) |j\mathbf{R}_e\rangle \quad (4.4b)$$

Also here one obtains different Wannier orbitals  $w_j(\mathbf{r} - \mathbf{R}_e)$  projecting on position space, centered on ion site  $\mathbf{R}_e$ ; it is possible to measure their spreading around the site considering the average spatial variance among different Wannier bands:

$$\Omega = \sum_j [\langle \mathbf{0}j | r^2 | \mathbf{0}j \rangle - \langle \mathbf{0}j | r | \mathbf{0}j \rangle^2] \quad (4.5)$$

This localization becomes fundamental when one considers the transformation of electronic single particle Hamiltonian Matrix elements (in particular the KS one in DFT), which is directly related to the band structure in momentum space:

$$H_{mn}^{el}(\mathbf{k}) = \langle m\mathbf{k} | H^{el} | n\mathbf{k} \rangle = \delta_{mn} \varepsilon_n(\mathbf{k}) \quad (4.6)$$

And which can be transformed in Wannier considering the matrix element between two Wannier states, and then transformed in Bloch space using 4.4a:

$$H_{ij}^{el}(\mathbf{R}'_e, \mathbf{R}_e) = \langle i\mathbf{R}'_e | H^{el} | j\mathbf{R}_e \rangle = \sum_{n\mathbf{k}} e^{-i\mathbf{k}\cdot(\mathbf{R}_e - \mathbf{R}'_e)} U_{im}^\dagger(\mathbf{k}) H_{mn}^{el}(\mathbf{k}) U_{nj}(\mathbf{k}) \quad (4.7)$$

Depending on the localization 4.5 of the Wannier orbitals this matrix element may show fast decay with the distance  $|\mathbf{R}'_e - \mathbf{R}_e|$ , and since they are the Fourier Coefficients of the electron eigenstates, if they show fast decay they can be used to perform a Fourier interpolation with controlled error. Exploiting the translational invariance of Wannier orbitals, one can show that also the matrix elements are invariant with respect to translation of

both vectors, thus one often center  $\mathbf{R}'_e$  in  $\mathbf{0}_e$  and consider  $H_{ij}^{el}(\mathbf{R}_e) \equiv H_{ij}^{el}(\mathbf{0}_e, \mathbf{R}_e)$  only.

### 4.1.2. Maximally Localized Wannier Functions

To perform the desired interpolation, one cannot settle for just any set of Wannier functions; one must achieve a specific, optimal localization. The standard in the field of Quantum Chemistry and Condensed Matter Physics is represented by the *Maximally Localized Wannier Functions* (MLWFs), introduced by Marzari and Vanderbilt [4].

The key idea is to exploit the **Gauge Invariance** of the Bloch states introduced in the first chapter:

$$\psi_{n\mathbf{k}}(\mathbf{r}) \rightarrow e^{i\varphi_n(\mathbf{k})}\psi_{n\mathbf{k}}(\mathbf{r}) \quad (4.8)$$

Since the Bloch state is defined only up to a periodic phase in reciprocal space, the resulting Wannier state inherits this freedom. The technique introduced by Marzari relies on the insight that the spatial variance  $\Omega$  (Eq. 4.5) is actually a *functional* of this gauge. The goal is to minimize this functional to find the “smoothest” possible gauge that achieves maximal localization in real space, a process that is often referred to as *Wannierization*.

This minimization procedure is the engine behind the standard library `wannier90` and is interfaced with many DFT codes such as VASP. It not only calculates the necessary transformation matrices but allows us to directly perform the interpolation of the band structure (and other observables) starting from a DFT calculation on a coarse  $\mathbf{k}$ -grid.

In practice, a robust method to achieve a good Wannierization (or at least a high-quality initial guess for the minimization) is via the **projection technique**. One projects  $N_B$  delocalized Bloch states onto a set of  $N_W$  trial orbitals  $|\chi_\alpha\rangle$ . These can be of various types: in materials where bands have specific characters, such as *s* and *p* orbitals in the silicon valence band, one can start with *hydrogen-like* orbitals localized at the atomic sites. This offers the distinct advantage of constructing a Wannier orbital that reflects the spatial character of the chemical bonding.

Otherwise, for general cases, one can employ analytic localized functions (e.g., Gaussians) centered on atomic sites.

Formally, we project the Bloch orbitals onto this localized basis set to define the overlap matrix  $A_{mi}(\mathbf{k})$ :

$$A_{mi}(\mathbf{k}) = \langle \psi_{m\mathbf{k}} | \chi_i \rangle \quad (4.9a)$$

Using this, we construct a set of Bloch-like orbitals  $|\phi_{n\mathbf{k}}\rangle$  which are smooth in  $\mathbf{k}$ -space

but generally not orthonormal:

$$|\phi_{i\mathbf{k}}\rangle = \sum_{m=1}^{N_B} |\psi_{m\mathbf{k}}\rangle A_{mi}(\mathbf{k}) \quad (4.9b)$$

To restore orthonormality while preserving the character of the projection, we first define the overlap matrix of the projected orbitals:

$$S_{ij}(\mathbf{k}) = \langle \phi_{i\mathbf{k}} | \phi_{j\mathbf{k}} \rangle = (A(\mathbf{k})^\dagger A(\mathbf{k}))_{ij} \quad (4.10)$$

We then construct the unitary transformation matrix  $U(\mathbf{k})$  that generates the orthonormal Wannier gauge:

$$U_{ij}(\mathbf{k}) = \sum_l A_{il}(\mathbf{k}) (S(\mathbf{k})^{-1/2})_{lj} \quad (4.11)$$

The resulting matrix  $U(\mathbf{k})$  is used in Eq. 4.4a to define the Wannier functions which are guaranteed to be orthonormal [8].

A major advantage of this technique over other initialization methods is that it preserves the symmetry and chemical character of the trial orbitals. The downside is that one requires prior knowledge of convenient trial orbitals, which is not always straightforward in complex compounds or for bands with a high degree of hybridization. For such cases, automated techniques have been developed. However, for the analysis conducted in this thesis, the materials are sufficiently simple to rely on the projection technique, at least as the initial guess provided to the `wannier90` code.

### 4.1.3. Deformation Potential Transformation

We seek a transformation for the *phonon* part which brings the deformation potential and the dynamical matrix to a site-localized representation, which we will call by analogy the *Phonon Wannier Representation*.

Retrieving the expression for the screened potential in linear response theory:

$$V(\mathbf{r}; \{\tau_{kp}\}) = \int d^3 r' \epsilon^{-1}(\mathbf{r}, \mathbf{r}') \sum_{k\mathbf{R}_p} V_k^{\text{ion}}(\mathbf{r}' - \tau_{kp}) \quad (4.12)$$

where the sum runs over all unit cells in the crystal centered at positions  $\mathbf{R}_p$  and atom indices  $k$  within the unit cell. The absolute position of each atom is  $\tau_{kp} = \tau_k + \mathbf{R}_p$ .

We are looking for the Deformation Potential  $\partial_{\nu\mathbf{q}} V(\mathbf{r})$ , which corresponds to the variation

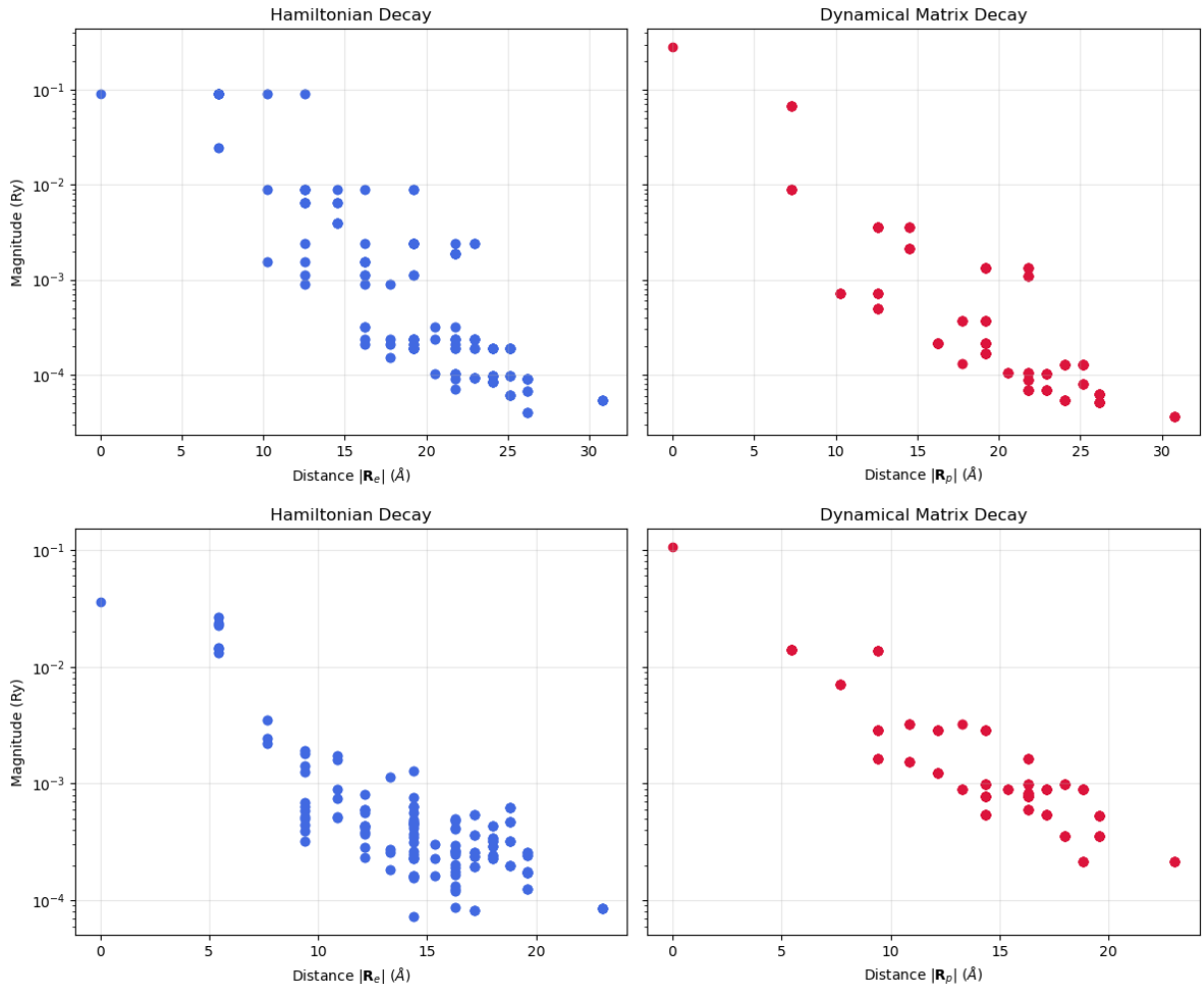


**Figure 4.2:** Semi-logarithmic real-space decay of Hamiltonian and dynamical matrix elements in two representative materials. **Top:** **Silicon (Si).** The electronic Hamiltonian and dynamical matrix exhibit a rapid decay with distance, reflecting the strong localization of maximally localized Wannier functions in a covalent semiconductor. **Bottom:** **Lithium Fluoride (LiF).** While exponential decay is still observed, dynamical matrix elements extend over slightly larger distances. This reduced localization is consistent with the polar nature of LiF, where long-range Coulomb interactions limit the spatial confinement of Wannier and phonon representations.

of the effective potential with respect to a collective displacement of the atoms  $\{\Delta\tau_{kp}^{\mathbf{q}\nu}\}$  associated with a phonon mode  $|\mathbf{q}\nu\rangle$  with momentum  $\mathbf{q}$  and branch index  $\nu$ . This can be expressed as:

$$\partial_{\nu\mathbf{q}}V(\mathbf{r}) = \frac{\partial}{\partial\eta}V(\mathbf{r}; \{\tau_{kp} + \eta\Delta\tau_{kp}^{\mathbf{q}\nu}\}) \Big|_{\eta=0} \quad (4.13)$$

The displacement field is related to the ansatz introduced in the initial derivation, this can be also seen as a projection of phonon state on the ionic position continuos basis  $\langle \tau_{kp} | \mathbf{q}\nu \rangle$ . In static conditions, taking the real part, we have:

$$\Delta\tau_{kp}^{\mathbf{q}\nu} = \operatorname{Re} \left[ \left( \frac{M_0}{M_k} \right)^{\frac{1}{2}} \mathbf{e}_{k\nu}(\mathbf{q}) e^{i\mathbf{q}\cdot\mathbf{R}_p} \right] \quad (4.14)$$

This can already be viewed as a transformation analogous to the Wannier transformation: mapping the collective phonon eigenstate  $|\mathbf{q}\nu\rangle$  to a localized displacement on a single atomic site.

To compute the directional derivative in Eq. 4.13, we use the chain rule with the gradient of the scalar field:

$$\partial_{\nu\mathbf{q}} V(\mathbf{r}) = \sum_{kp} \Delta\tau_{kp}^{\mathbf{q}\nu} \cdot \nabla_{\tau_{kp}} V(\mathbf{r}; \{\tau_{kp}\}) = \sum_{kp} e^{i\mathbf{q}\cdot\mathbf{R}_p} \left( \frac{M_0}{M_k} \right)^{\frac{1}{2}} \mathbf{e}_{k\nu}(\mathbf{q}) \cdot \partial_{k\mathbf{R}_p} V(\mathbf{r}) \quad (4.15a)$$

Where we have introduced the vector field representing the gradient with respect to atomic positions:

$$[\partial_{k\mathbf{R}_p} V(\mathbf{r})]_a = \frac{\partial}{\partial \tau_{kpa}} V(\mathbf{r}; \{\tau_{kp}\}) \quad (4.15b)$$

where  $a = x, y, z$  represents a Cartesian direction.

Exploiting the orthogonality relations between phonon eigenmodes defined in Eq. 2.11, it is possible to obtain the inverse transformation by considering:

$$\partial_{k\mathbf{R}_p} V(\mathbf{r}) = \frac{1}{N_p} \sum_{\mathbf{q}\nu} e^{-i\mathbf{q}\cdot\mathbf{R}_p} \left( \frac{M_k}{M_0} \right)^{\frac{1}{2}} \mathbf{e}_{k\nu}^*(\mathbf{q}) \partial_{\nu\mathbf{q}} V(\mathbf{r}) \quad (4.16)$$

To prove this, we substitute the expansion of  $\partial_{\nu\mathbf{q}} V(\mathbf{r})$  into the right-hand side:

$$\partial_{k\mathbf{R}_p} V(\mathbf{r}) = \frac{1}{N_p} \sum_{\mathbf{q}\nu} e^{-i\mathbf{q}\cdot\mathbf{R}_p} \left( \frac{M_k}{M_0} \right)^{\frac{1}{2}} \mathbf{e}_{k\nu}^*(\mathbf{q}) \left[ \sum_{k'p'} e^{i\mathbf{q}\cdot\mathbf{R}_{p'}} \left( \frac{M_0}{M_{k'}} \right)^{\frac{1}{2}} \mathbf{e}_{k'\nu}(\mathbf{q}) \cdot \partial_{k'\mathbf{R}_{p'}} V(\mathbf{r}) \right]$$

Since we are looking for a vector quantity, we examine its Cartesian component  $\alpha$ . We first express the scalar product inside and isolate the summation over the phonon branches  $\nu$ :

$$[\partial_{k\mathbf{R}_p} V(\mathbf{r})]_\alpha = \sum_{k'p'} \sum_{\mathbf{q}} \frac{e^{i\mathbf{q}\cdot(\mathbf{R}_{p'}-\mathbf{R}_p)}}{N_p} \sqrt{\frac{M_k}{M_{k'}}} \sum_{\beta} \left[ \sum_{\nu} e_{\alpha k\nu}^*(\mathbf{q}) e_{\beta k'\nu}(\mathbf{q}) \right] [\partial_{k'\mathbf{R}_{p'}} V(\mathbf{r})]_{\beta} \quad (4.17)$$

We now apply the completeness relation. With the appropriate normalization, we substitute the term in the square brackets with:

$$\sum_{\nu} e_{\alpha k \nu}^* e_{\beta k' \nu} = \delta_{kk'} \delta_{\alpha \beta} \quad (4.18)$$

Substituting this back, the sum over  $k'$  and  $\beta$  collapses. The Kronecker delta  $\delta_{kk'}$  forces the mass ratio  $\sqrt{M_k/M_{k'}}$  to unity, and the expression becomes:

$$[\partial_{k\mathbf{R}_p} V(\mathbf{r})]_{\alpha} = \sum_{p'} \left[ \frac{1}{N_p} \sum_{\mathbf{q}} e^{i\mathbf{q} \cdot (\mathbf{R}_{p'} - \mathbf{R}_p)} \right] [\partial_{k\mathbf{R}_{p'}} V(\mathbf{r})]_{\alpha} \quad (4.19)$$

The sum over  $\mathbf{q}$  yields  $N_p \delta_{pp'}$ , and we find exactly the term on the left-hand side.

The quantity  $\partial_{k\mathbf{R}_p} V(\mathbf{r})$  represents the change in the self-consistent potential at position  $\mathbf{r}$  due to the displacement of a single atom at position  $\tau_{kp}$ . Since the interaction is screened, one expects sufficient localization; however, there is no procedure as for MLWFs to actively achieve maximal localization. This rather depends on the polarity of the material, where less effective screening may imply a weaker localization.

To complete the picture, it is also useful to define the transformation of the dynamical matrix itself. While we defined  $D_{k\alpha, k'\beta}(\mathbf{q})$  in Eq. (2.10c) as the mass-weighted Fourier transform of the interatomic force constants, it is often more convenient to express it in the basis of the collective phonon modes  $|\mathbf{q}\nu\rangle$ .

Recalling the eigenvalue problem introduced in Chapter 2, we have:

$$\begin{aligned} & \sum_{k'\beta} D_{k\alpha, k'\beta}(\mathbf{q}) e_{k'\beta, \nu}(\mathbf{q}) = \omega_{\nu}^2(\mathbf{q}) e_{k\alpha, \nu}(\mathbf{q}) \\ \implies & \sum_{k'\beta} \sum_{k\alpha} e_{k\alpha, \mu}^*(\mathbf{q}) D_{k\alpha, k'\beta}(\mathbf{q}) e_{k'\beta, \nu}(\mathbf{q}) = \sum_{k\alpha} e_{k\alpha, \mu}^*(\mathbf{q}) \omega_{\nu}^2(\mathbf{q}) e_{k\alpha, \nu}(\mathbf{q}) \end{aligned}$$

Exploiting the orthogonality relations as before, we obtain the diagonal representation:

$$D_{\mu\nu}(\mathbf{q}) = \langle \mathbf{q}\mu | \hat{D}^{ph} | \mathbf{q}\nu \rangle = \sum_{k'\beta} \sum_{k\alpha} e_{k\alpha, \mu}^*(\mathbf{q}) D_{k\alpha, k'\beta}(\mathbf{q}) e_{k'\beta, \nu}(\mathbf{q}) = \delta_{\mu\nu} \omega_{\nu}^2(\mathbf{q}) \quad (4.20)$$

where  $\hat{D}^{ph}$  represents the dynamical operator in the abstract Hilbert space.

We now introduce the Dynamical Matrix in the *Phonon Wannier basis*,  $D_{k\alpha, k'\beta}(\mathbf{R}_p)$ , defined via the inverse Fourier transform. This quantity is directly proportional to the interatomic force constants (rescaled by atomic masses). This representation makes it

evident that the localization properties of the phonon degrees of freedom depend intrinsically on the material properties: the electronic screening determines the spatial decay of the interactions with distance  $\mathbf{R}_p$ .

The link with the matrix in the phonon mode basis becomes:

$$D_{\mu\nu}(\mathbf{q}) = \sum_{k'\beta} \sum_{k\alpha} e_{k\alpha,\mu}^*(\mathbf{q}) \left[ \sum_{\mathbf{R}_p} e^{i\mathbf{q}\cdot\mathbf{R}_p} D_{k\alpha,k'\beta}(\mathbf{R}_p) \right] e_{k'\beta,\nu}(\mathbf{q}) \quad (4.21)$$

As we did for the deformation potential, we can invert this transformation. By using the completeness of the eigenvectors and the orthogonality of the plane waves, we express the real-space matrix in terms of the quantities computed on the coarse grid:

$$D_{k\alpha,k'\beta}(\mathbf{R}_p) = \frac{1}{N_p} \sum_{\mathbf{q}} e^{-i\mathbf{q}\cdot\mathbf{R}_p} \sum_{\nu} e_{k\alpha,\nu}(\mathbf{q}) \omega_{\nu}^2(\mathbf{q}) e_{k'\beta,\nu}^*(\mathbf{q}) \quad (4.22)$$

This is the fundamental relation used to obtain the Dynamical Matrix in the localized real-space basis starting from a coarse grid calculation of the diagonal frequencies and eigenvectors. If this basis is sufficiently localized, it allows for the reliable interpolation procedure that will be detailed in the following section.

#### 4.1.4. Electron-Phonon Tensor in Momentum and Wannier Space

From the transformations introduced above, one can derive a transformation for the electron-phonon tensor as well. In the momentum representation, the coupling is associated with the overlap of delocalized quantities:

$$g_{mn,\nu}(\mathbf{k}, \mathbf{q}) = \langle m\mathbf{k} + \mathbf{q} | \partial_{\mathbf{q}\nu} V | n\mathbf{k} \rangle \quad (4.23)$$

In the Wannier representation, one can introduce the overlap between three localized quantities: an orbital centered at  $\mathbf{0}_e$  (exploiting translational invariance), one at  $\mathbf{R}_e$ , and the deformation potential in response to the displacement of one atom  $k$  in the supercell  $\mathbf{R}_p$ :

$$g_{ij,k\alpha}(\mathbf{R}_e, \mathbf{R}_p) = \langle i\mathbf{0}_e | \partial_{\mathbf{R}_p k\alpha} V | j\mathbf{R}_e \rangle \quad (4.24)$$

As the formulation suggests, if all quantities are sufficiently localized, one expects a rapid decay of the matrix elements in real space. This can be understood by interpreting Eq. (4.25) as a measure of the spatial overlap between three localized objects: two elec-

tronic Wannier orbitals and the deformation potential. A schematic visualization of this overlap is shown in Fig. 4.3.

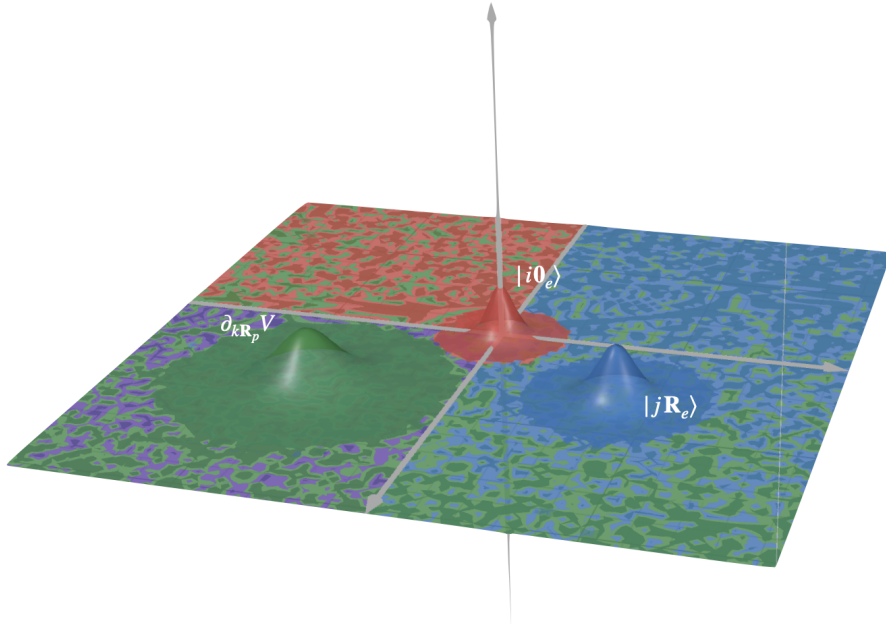


**Figure 4.3:** Schematic real-space visualization of the electron–phonon matrix element  $g_{ij,k\alpha}(\mathbf{R}_e, \mathbf{R}_p)$  as the overlap between three localized quantities: an initial electronic Wannier orbital  $|i\mathbf{0}_e\rangle$  (red), a final Wannier orbital  $|j\mathbf{R}_e\rangle$  (blue), and the deformation potential  $\partial_{k\mathbf{R}_p}V$  induced by the displacement of atom  $k$  in cell  $\mathbf{R}_p$  (green).

Implementing the correct transformation allows us to interpolate onto finer grids, which is essential for ab initio DMC implementations. A common way to check the localization of the matrix elements is to plot their magnitude, fixing the electron position at the origin and observing the decay with respect to the perturbation distance (or vice versa) as shown in figure 4.4.

To derive the exact transformation, we apply the previously derived rules to each electronic

state and the deformation potential:

$$\begin{aligned} \langle i\mathbf{R}'_e | \partial_{\mathbf{R}_p k\alpha} V | j\mathbf{R}_e \rangle &= \sum_{mn} \sum_{\mathbf{k}\mathbf{k}'} e^{i(\mathbf{k}' \cdot \mathbf{R}'_e - \mathbf{k} \cdot \mathbf{R}_e)} U_{im}^\dagger(\mathbf{k}') \langle m\mathbf{k}' | \partial_{\mathbf{R}_p k\alpha} V | n\mathbf{k} \rangle U_{nj}(\mathbf{k}) \\ &= \frac{1}{N_p} \sum_{mn\nu} \sum_{\mathbf{k}\mathbf{k}'\mathbf{q}} \left( \frac{M_k}{M_0} \right)^{\frac{1}{2}} e^{i(\mathbf{k}' \cdot \mathbf{R}'_e - \mathbf{k} \cdot \mathbf{R}_e - \mathbf{q} \cdot \mathbf{R}_p)} U_{im}^\dagger(\mathbf{k}') \langle m\mathbf{k}' | \partial_{\nu\mathbf{q}} V(\mathbf{r}) | n\mathbf{k} \rangle U_{nj}(\mathbf{k}) e_{k\nu\alpha}^*(\mathbf{q}) \\ &= \frac{1}{N_p} \sum_{mn\nu} \sum_{\mathbf{k}\mathbf{q}} \left( \frac{M_k}{M_0} \right)^{\frac{1}{2}} e^{i(\mathbf{k} \cdot (\mathbf{R}'_e - \mathbf{R}_e) + \mathbf{q} \cdot (\mathbf{R}'_e - \mathbf{R}_p))} U_{im}^\dagger(\mathbf{k} + \mathbf{q}) \langle m\mathbf{k} + \mathbf{q} | \partial_{\nu\mathbf{q}} V(\mathbf{r}) | n\mathbf{k} \rangle U_{nj}(\mathbf{k}) e_{k\nu\alpha}^*(\mathbf{q}) \end{aligned}$$

where in the last step we applied momentum conservation  $\mathbf{k}' = \mathbf{k} + \mathbf{q}$ . Finally, one can exploit the translational invariance of the quantities in Wannier space. By translating the entire system by  $-\mathbf{R}'_e$  and relabeling  $\mathbf{R}_p - \mathbf{R}'_e \rightarrow \mathbf{R}_p$  and  $\mathbf{R}_e - \mathbf{R}'_e \rightarrow \mathbf{R}_e$ , we obtain the fundamental transformation to real space:

$$\begin{aligned} g_{ij,k\alpha}(\mathbf{R}_e, \mathbf{R}_p) &= \langle i\mathbf{0}_e | \partial_{\mathbf{R}_p k\alpha} V | j\mathbf{R}_e \rangle \\ &= \frac{1}{N_p} \sum_{mn\nu} \sum_{\mathbf{k}\mathbf{q}} \left( \frac{M_k}{M_0} \right)^{\frac{1}{2}} e^{-i(\mathbf{k} \cdot \mathbf{R}_e + \mathbf{q} \cdot \mathbf{R}_p)} U_{im}^\dagger(\mathbf{k} + \mathbf{q}) g_{mn,\nu}(\mathbf{k}, \mathbf{q}) U_{nj}(\mathbf{k}) e_{k\nu\alpha}^*(\mathbf{q}) \end{aligned} \quad (4.25)$$

Often even in Wannier representation one condense the cartesian index  $\alpha$  and basis index  $k$ , in one index  $\nu = \alpha k$ . A direct comparison of the amplitude distribution of the two matrices for a certain triplet of band states  $(m, n, \nu)$  or  $(i, j, \nu)$  shows a clear transition: we go from an almost homogeneous situation in reciprocal space to a structure in real space characterized by clear "spikes," appearing as horizontal and vertical stripes. This structure suggests that the matrix can be decomposed as a linear combination of lower-rank matrices. Modern numerical linear algebra techniques allow us to find the optimal low-rank factorization, namely, the representation of the matrix as a lower-rank one that guarantees the optimal reconstruction error. This not only allows us to save memory space but also to decouple the electron and phonon contributions in the matrix, achieving a significant speedup in performance.

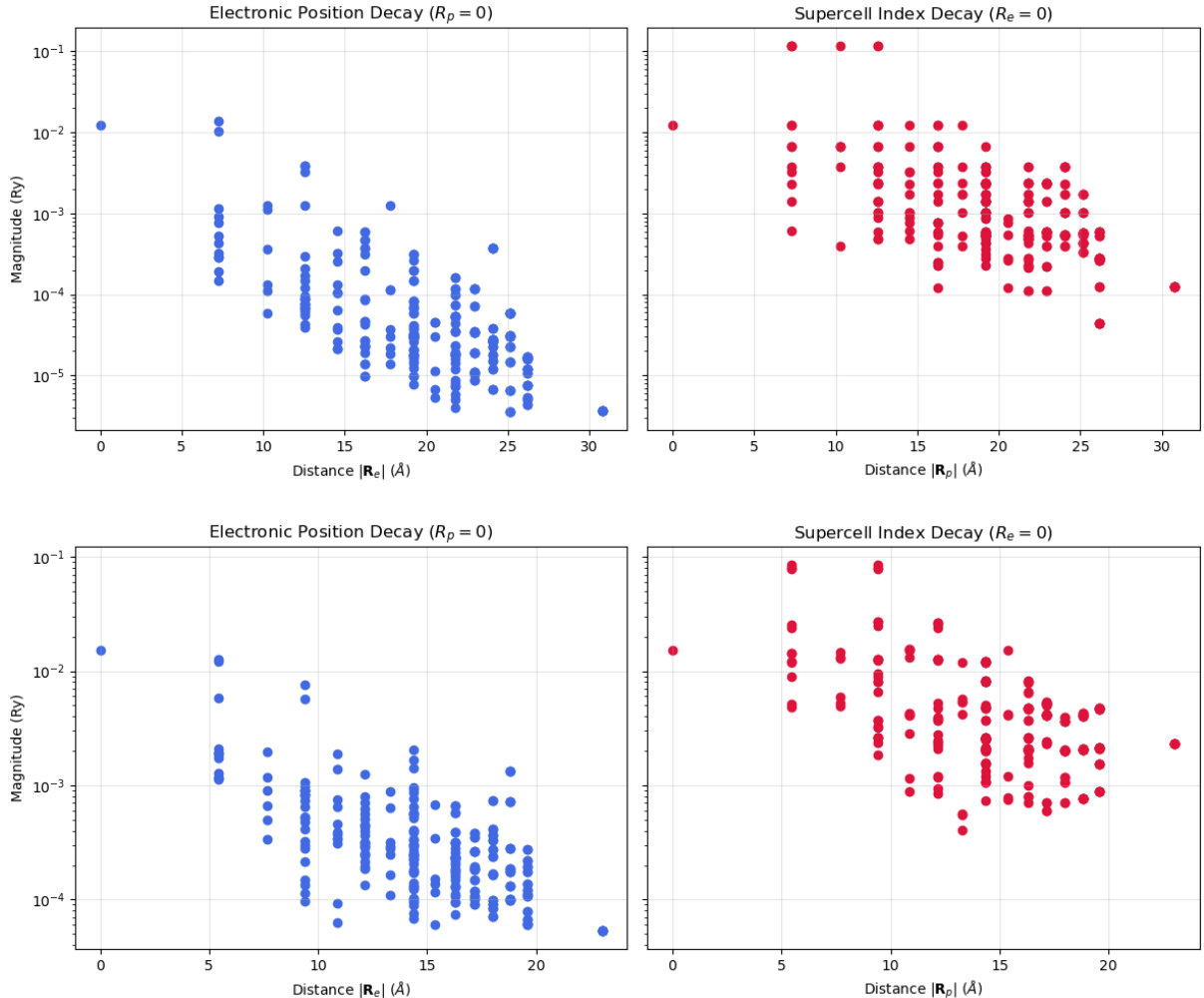


**Figure 4.4:** Semi-logarithmic real-space decay of the electron–phonon coupling tensor in Wannier space. The magnitude of  $g_{ij,k\alpha}(\mathbf{R}_e, \mathbf{R}_p)$  is shown while fixing one coordinate to the origin and varying the other: **left panels** report the decay versus the electronic separation  $|\mathbf{R}_e|$  at  $\mathbf{R}_p = \mathbf{0}$ , and **right panels** report the decay versus the perturbation (phonon) separation  $|\mathbf{R}_p|$  at  $\mathbf{R}_e = \mathbf{0}$ . **Top:** Si. The coupling is strongly localized, consistent with well-localized MLWFs and screened lattice response. **Bottom:** LiF. A slightly slower decay is observed, consistent with the polar character of the material and the more extended long-range electrostatic contribution to the lattice perturbation.

## 4.2. Tensor Decomposition

In this Section We introduce some tools that usually find vast application in the field of data analisys. They rely on the fact that data. especially high dimensional one, that are not just random noise often are arranged on, or close to, much lower dimensional spaces. The techniques here presented are thus powerful linear algebra tools for *Dimensionality Reduction*, a core process in many data driven fields.

In this section we will first present them adapted to the electron-phonon coupling data, and then use then for their initial purpose: investigate the structure of the tensor and achieve a significative compression. Later on, in the last chapter, we show that since they naturally factorize the various dimensions of the tensor, they bring a big advantage also in terms of performance, which is the main bottleneck of Wannier Interpolation.

### 4.2.1. Low-Rank Approximation: From PCA to Tensor SVD

When dealing with high-dimensional data, a fundamental dimensionality reduction technique is *Principal Component Analysis* (PCA). It relies on the idea that a data matrix  $\mathbf{X}$ , containing  $N$  samples each of dimension  $D$ , can be viewed as a collection of  $N$  vectors in a  $D$ -dimensional vector space. If the data is not *homogeneously* distributed, we expect certain directions to capture more variation than others. Specifically, there often exists a subspace of dimension  $K < D$  onto which we can project the data while preserving most of the information. This analysis is typically performed by centering the dataset around its mean, introducing the **covariance matrix**, and diagonalizing it:

$$\mathbf{C} = \frac{\mathbf{X}^T \mathbf{X}}{N - 1} = \mathbf{V} \Lambda \mathbf{V}^T \quad (4.26)$$

The columns of  $\mathbf{V}$ , denoted  $\mathbf{v}_\alpha$ , are the eigenvectors of  $\mathbf{C}$ . Each represents an independent orthogonal direction accounting for a portion of the data's variation proportional to the eigenvalue  $\lambda_\alpha$ . By projecting the data onto the subset of Principal Components with the highest variance, we obtain a meaningful low-rank representation.

### Singular Value Decomposition of the Interaction Tensor

While PCA operates on the square covariance matrix, a more general framework applicable directly to rectangular matrices, such as the interaction matrices in our model, is the *Singular Value Decomposition* (SVD). For a generic real-space interaction matrix  $\mathbf{M}$

of dimension  $N_e \times N_p$ , the SVD guarantees the existence of the factorization:

$$\mathbf{M} = \mathbf{U}\Sigma\mathbf{V}^T = \sum_{r=1}^{\min(N_e, N_p)} \sigma_r \mathbf{u}_r \mathbf{v}_r^T \quad (4.27)$$

where  $\sigma_r$  are the singular values (sorted in descending order), and  $\mathbf{u}_r, \mathbf{v}_r$  are the left and right singular vectors.

In the context of the electron-phonon interaction, the object of interest is not a simple matrix but a higher-order tensor  $g_{ij,\nu}(\mathbf{R}_e, \mathbf{R}_p)$  depending on spatial indices  $(\mathbf{R}_e, \mathbf{R}_p)$  and quantum numbers (band indices  $i, j$  and cartesian/basis index  $\nu$ ). To apply the SVD efficiently, we adopt a "slicing" strategy. We treat the quantum indices as fixed parameters and perform the decomposition specifically on the spatial degrees of freedom. For each triplet  $(i, j, \nu)$ , we flatten the 3D lattice grids into 1D super-indices and decompose the resulting spatial coupling matrix, where the tensor slice are  $N_e \times N_p$  matrices and the singular vector are  $N_e \times 1$  and  $N_p \times 1$ , for simplicity we keep however the indexing of this direction with  $\mathbf{R}_e, \mathbf{R}_p$

Using the notation where  $g_{v,n,m}$  represents the spatial matrix for a fixed mode and band pair, the decomposition is written as:

$$g_{ijk\alpha}^{(r)}(\vec{R}_e, \vec{R}_p) = \sum_{\tilde{r}=1}^r \sigma_{\tilde{r}ijk\alpha} u(\mathbf{R}_e)_{\tilde{r}ik\alpha} v^\top(\mathbf{R}_p)_{\tilde{r}jk\alpha} \quad (4.28)$$

or, collecting the singular vector as row of a collection of matrices  $\{U, V\}_{ij\nu}$ , each of them being respectively  $N_e \times r_{max}$  and  $N_p \times r_{max}$ , and a collection of  $r_{max} \times r_{max}$  diagonal matrices  $\{\Sigma\}_{ij\nu}$ :

$$g_{ijk\alpha}^{(r)}(\vec{R}_e, \vec{R}_p) = U(r)_{i,j,\nu} \Sigma(r)_{ij\nu} V(r)_{i,j,\nu}^\top \quad (4.29)$$

Where with  $U(r)$  we indicate the original matrix considered up to column  $r$ , and  $\Sigma(r)$  equal the first  $r \times r$  block.

**Physical Interpretation and Error Bounds.** This decomposition offers a profound physical insight, as highlighted by Luo et al. [26]. The factorization effectively *decouples* the electron and phonon coordinates. The term  $\mathbf{u}(\mathbf{R}_e)$  represents an effective electronic wavefunction component, while  $\mathbf{v}(\mathbf{R}_p)$  acts as a phonon source term. By retaining only the top  $r$  components (where typically  $r \ll \min(N_e, N_p)$ ), we approximate the complex, non-local interaction as a sum of separable, rank-1 interactions. This separability is the key mechanism that reduces the interpolation complexity from quadratic to linear, as show later.

The accuracy of this truncation is rigorously bounded by the Eckart-Young-Mirsky theorem [30]. The theorem states that for any rank- $r$  approximation, the reconstruction error in the Frobenius norm is determined solely by the discarded singular values:

$$\|g - g^r\|_F^2 = \sum_{ij\nu} \sum_{\tilde{r}=r+1}^r \sigma_{\tilde{r}ij\nu}^2 \quad (4.30)$$

This property allows us to strictly control the interpolation accuracy: by monitoring the cumulative sum of the squared singular values (as implemented in our `svd_trend` analysis), we can determine the minimal rank  $r_{max}$  required to achieve a target fidelity (e.g., 99.9%) before performing the full interpolation.

However, the approach described above relies on a specific "slicing" of our tensor. Effectively, we separate the dependence on the three quantum indices, treating them as external parameters. For each triplet  $(i, j, \nu)$ , we construct the two-dimensional matrix  $M(\vec{R}_e, \vec{R}_p) = g_{ij\nu}(\vec{R}_e, \vec{R}_p)$  and apply the Singular Value Decomposition to it individually as showed in 4.5.a.

This procedure finds an optimal factorization/basus for each *slice* in isolation, but not a global one. Consequently, it does not capture any correlation between different band indices or phonon modes. While this *slice-wise* SVD might be efficient for compression if the correlations between quantum numbers are weak, it ignores the global structure of the data. In principle, one might prefer a framework that performs the factorization while preserving the full tensor structure, as this allows for the extraction of deeper physical insights directly from the decomposition.

### 4.2.2. Tucker Decomposition

The electron-phonon coupling is a 5-dimensional tensor in either the Bloch or Wannier representation. In the latter, considering  $N_w$  Wannier orbitals,  $N_p, N_e$  direct lattice vectors, and  $N_\nu = 3N_{at}$  for the last index, we have  $g \in \mathbb{C}^{N_p \times N_e \times N_\nu \times N_w \times N_w}$ , and similarly for the tensor in Bloch space.

With the Tucker decomposition, we consider a Low Rank factorization for each dimension, denoting the rank of each as  $R_i \leq N_i$ . This implies the following mapping:

$$(N_p \times N_e \times N_\nu \times N_w \times N_w) \rightarrow (R_1 \times R_2 \times R_3 \times R_4 \times R_5) \quad (4.31)$$

We express the full tensor as a **core tensor**,  $\Sigma \in \mathbb{C}^{(R_1 \times R_2 \times R_3 \times R_4 \times R_5)}$ , which is *contracted* with a factor matrix for each dimension  $A^{(i)} \in \mathbb{C}^{N_i \times R_i}$ . Each factor matrix represents a

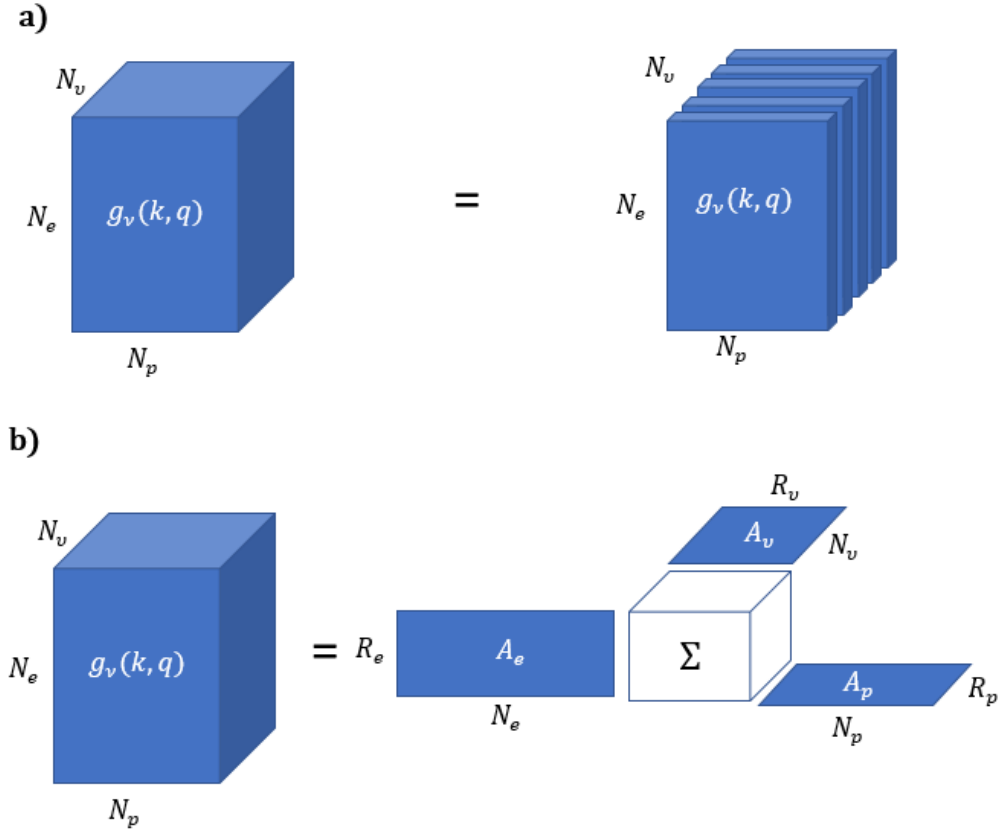


**Figure 4.5: Comparison of Decomposition Strategies.** **a)** The slice-wise SVD approach treats the higher-order tensor as a stack of independent matrices, decomposing each slice individually. **b)** A tensor decomposition (such as Tucker) maintains the multi-dimensional structure, factorizing the object into a core tensor  $\Sigma$  and mode-specific factor matrices  $A$ . *Note: For visualization purposes, the schematic consider a simplified 3D tensor  $\mathbf{g}_v(k, q)$  where the electronic band indices  $m$  and  $n$  are fixed, rather than the full 5D interaction tensor.*

given dimension  $i$  of the tensor with a low-rank representation of size  $R_i$ ; these can be viewed as different principal components or features corresponding to variations in that dimension.

The connection with SVD is that, in the previous approach, we had a single feature index  $r$ , with its weight  $\sigma_r$  and two vectors (one for each spatial dimension) to reconstruct the corresponding rank-1 matrix, and we proceeded with  $N_w \times N_w \times N_v$  sliced independent decompositions. Here instead, each entry in the core tensor  $\sigma_{r_1 r_2 r_3 r_4 r_5}$  represents the importance of a specific combination of principal components across different tensor dimensions. From the corresponding vectors  $\{\mathbf{a}^{r_i}\}$  (corresponding to the  $r_i$ -th column of

$A^{(i)}$ ), one can obtain a rank-1 tensor contribution<sup>2</sup> as:

$$g_{n_p n_e \nu i j} = \sigma_{r_1 r_2 r_3 r_4 r_5} a_{n_p}^{r_1} a_{n_e}^{r_2} a_{\nu}^{r_3} a_i^{r_4} a_j^{r_5} \quad (4.32)$$

This idea is visually expressed in Figure 4.5b.

To include the full rank, one must sum more terms from the previous definition. This can be done either with the tensor formalism of the **n-mode product** or using the contraction introduced by the **Einstein Formalism** in general relativity, where an index that appears twice in an expression indicates a summation, as follows:

$$g_{n_p n_e \nu i j} = \sum_{r_1=1}^{R_1} \cdots \sum_{r_5=1}^{R_5} \sigma_{r_1 r_2 r_3 r_4 r_5} a_{n_p}^{r_1} a_{n_e}^{r_2} a_{\nu}^{r_3} a_i^{r_4} a_j^{r_5} \equiv \sum_{r_1 r_2 r_3 r_4 r_5} A_{n_p r_1}^{(1)} A_{n_e r_2}^{(2)} A_{\nu r_3}^{(3)} A_{i r_4}^{(4)} A_{j r_5}^{(5)} \quad (4.33)$$

The great advantage is that in this case one factorize all the dimension of the tensor, and most importantly look for an unique basis which factorize it also over different band indices.

### 4.2.3. Notes on the implementation

All decompositions presented in this work are obtained using well-established and widely adopted numerical libraries. In particular, matrix factorizations are performed using `scipy.linalg`, which provides both deterministic and randomized implementations of the Singular Value Decomposition (SVD). Depending on the size of the sliced matrices, and so on the number of lattice vectors, either approach can be optimal in practice: deterministic SVD is preferred for moderate dimensions, while randomized algorithms are employed for larger problems to reduce computational cost without compromising accuracy.

The Tucker decomposition is computed using the `tensorly` library, which implements standard algorithms for tensor factorization. In this work we adopt the Higher-Order Orthogonal Iteration (HOOI) scheme [31, 32], which iteratively refines the factor matrices by solving a sequence of truncated SVD problems on mode-wise matricizations of the tensor, in other terms, it consider SVD on slices of the tensor over different dimension.

---

<sup>2</sup>Strictly speaking, the *rank* of a tensor is defined as the minimal number of rank-1 tensors required to reconstruct it exactly (CP rank). In the context of Tucker decomposition, we refer to the *multilinear rank*, which is the tuple  $(R_1, R_2, \dots, R_5)$  representing the linear rank of the tensor unfolded along each respective mode.

This procedure naturally enforces orthogonality of the factor matrices, a property that is particularly desirable in the present context, as it provides a well-conditioned low-rank reconstruction and allows a clear interpretation of the contributions along different tensor modes.

In practice, the HOOI algorithm was observed to be numerically stable for the tensors considered here. All results shown in this work were obtained using a fixed number of iterations (typically 10) and a relative convergence tolerance of  $10^{-4}$  on the reconstruction error, which was sufficient to reach stable factor matrices and core tensor values. We verified that increasing the number of iterations did not lead to appreciable changes in the compressed representations.

It is worth noting that, although Tucker decomposition is computationally more demanding than a simple matrix SVD, this cost is incurred only once as a preprocessing step. In particular, on a common mid-ranged Notebook, for a tensor defined on 6x6x6 Grid with 6 modes and 4 bands, Tucker takes around 20 minutes and SVD 1 minute. The resulting compressed representation is then stored and reused throughout the Monte Carlo sampling. Consequently, the additional overhead associated with Tucker decomposition does not affect the overall efficiency of the Diagrammatic Monte Carlo algorithm, with interpolation performances and accuracy differences with SVD that can be advantageous.

#### 4.2.4. Compression Results

Starting from electron–phonon matrix elements computed on a coarse *ab initio* grid, we build low-rank compressed representations of the corresponding Wannier-space tensor. For the slice-wise SVD we factorize, for each fixed  $(i, j, \tilde{\nu})$ , the spatial matrix  $g_{ij\tilde{\nu}}(\mathbf{R}_e, \mathbf{R}_p)$  and retain a truncation rank  $r \leq r_{\max}$  (with  $r_{\max} = \min(N_e, N_p)$ ). For Tucker decomposition we keep the band and mode directions full rank, and compress only the lattice-vector modes, using the same target rank  $r$  along  $\mathbf{R}_e$  and  $\mathbf{R}_p$ . It is convenient to introduce an *effective* core tensor where the band and mode factor matrices have already been absorbed. The resulting low-rank approximation reads:

$$C_{r_e r_p i j \tilde{\nu}} = \sum_{r_i=1}^{N_w} \sum_{r_j=1}^{N_w} \sum_{r_{\tilde{\nu}}=1}^{N_{\tilde{\nu}}} \Sigma_{r_e r_p r_i r_j r_{\tilde{\nu}}} A_{ir_i}^{(i)} A_{jr_j}^{(j)} A_{\tilde{\nu} r_{\tilde{\nu}}}^{(\tilde{\nu})}, \quad (4.34a)$$

$$g_{ij\tilde{\nu}}^{(r)}(\mathbf{R}_e, \mathbf{R}_p) = \sum_{r_e=1}^r \sum_{r_p=1}^r C_{r_e r_p i j \tilde{\nu}} A_{\mathbf{R}_e r_e}^{(e)} A_{\mathbf{R}_p r_p}^{(p)}. \quad (4.34b)$$

Here we have introduced a flattened Cartesian/atomic index  $\tilde{\nu} \equiv (k, \alpha)$ .

We quantify the approximation quality through the relative Frobenius reconstruction error

$$\epsilon(r) = \frac{\sum_{ij\nu} \sum_{\mathbf{R}_e, \mathbf{R}_p} |g_{ij\nu}(\mathbf{R}_e, \mathbf{R}_p) - g_{ij\nu}^{(r)}(\mathbf{R}_e, \mathbf{R}_p)|^2}{\sum_{ij\nu} \sum_{\mathbf{R}_e, \mathbf{R}_p} |g_{ij\nu}(\mathbf{R}_e, \mathbf{R}_p)|^2}, \quad (4.35)$$

which for slice-wise SVD can be evaluated directly from the discarded singular values (Eq. 4.30), while for Tucker it is computed by explicit reconstruction. The same analysis is performed in Bloch space, with identical definitions and different index meaning.

Results are shown in Fig. 4.6. The key observation is the strong contrast between Bloch and Wannier representations: in Wannier space the coupling admits an efficient low-rank representation with only a few components, whereas in Bloch space the delocalized nature of the states and the non-smooth gauge lead to a much slower decay. Moreover, while in Wannier space SVD and Tucker yield comparable accuracy, in Bloch space Tucker is penalized by the attempt to learn a single global basis across all band and mode indices, resulting in substantially larger errors.

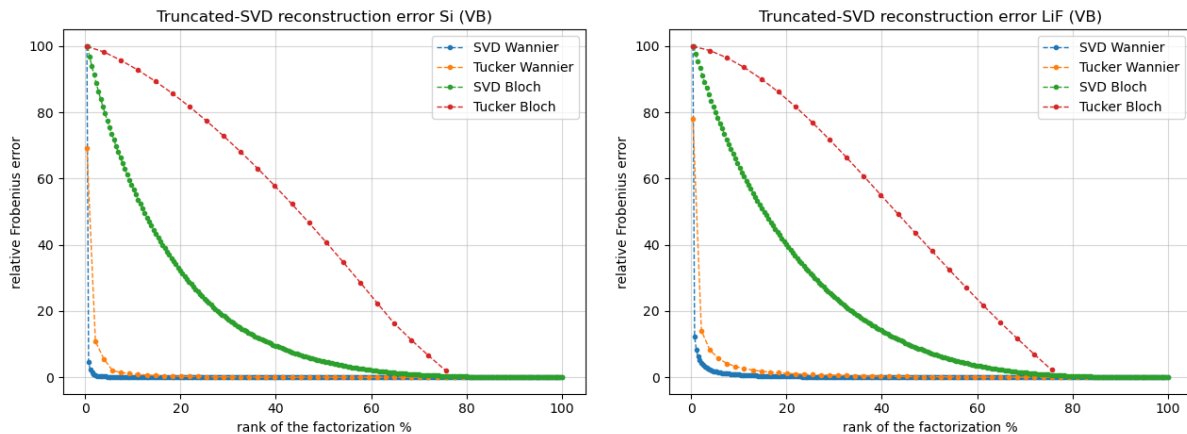


**Figure 4.6:** Relative Frobenius reconstruction error as a function of retained rank (valence-band subspace). We compare truncated SVD in Bloch and Wannier representations, and Tucker decomposition evaluated in both spaces, for silicon and LiF.

Focusing on the Wannier curves (Fig. 4.7), slice-wise SVD reaches an almost negligible reconstruction error already at  $r/r_{\max} \simeq 2\%$ , in agreement with Ref. [26]. Tucker instead saturates around  $r/r_{\max} \simeq 8\%$ , which is again expected, considering the trade-off encountered when looking for a single shared basis over the full tensor. This has a positive counterpart in terms of memory: slice-wise SVD stores one set of singular vectors per slice, leading to a memory cost scaling as  $r(N_e + N_p)N_iN_jN_\nu$ , whereas Tucker stores a global core of size  $r^2N_iN_jN_\nu$  plus factor matrices (dominantly  $r(N_e + N_p)$ ). For the optimal ranks in Fig. 4.7, this corresponds to a memory footprint of  $\sim 4\text{--}5\%$  for slice-wise

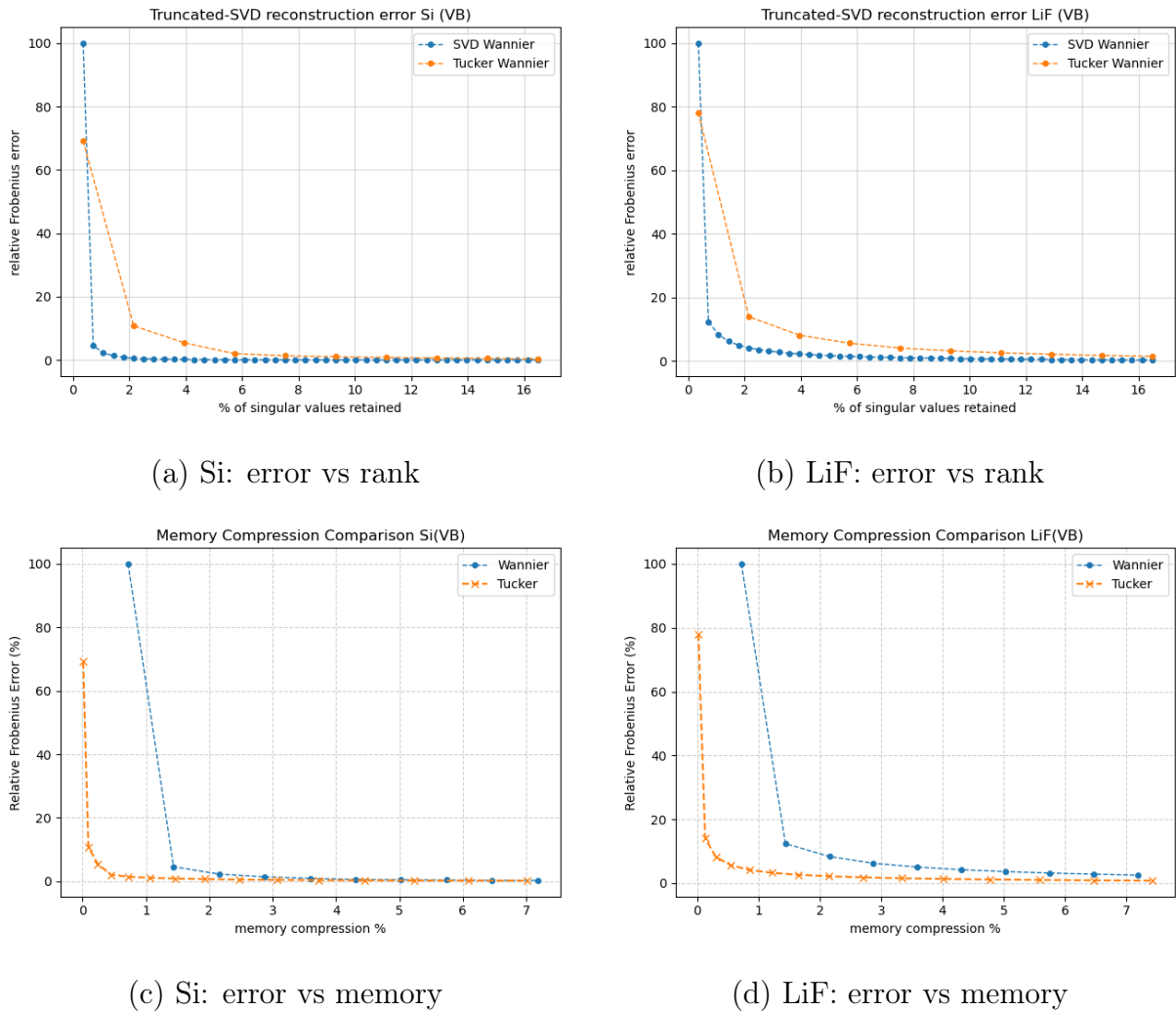


Figure 4.7: Zoom of Wannier-space reconstruction errors as a function of retained rank fraction (top row) and effective memory footprint (bottom row), for silicon and LiF.

SVD versus 1% for Tucker.

#### 4.2.5. Structure of the Tensor in Bloch and Wannier Representations

To further understand the latent structure of the electron–phonon (e–ph) matrix elements in the two representations, we begin by inspecting heat-map visualizations of their amplitudes. Already at this level, a clear qualitative difference emerges. In the Bloch representation, the tensor exhibits a rather homogeneous amplitude distribution, with no evident low-rank structure. In contrast, in the Wannier representation the spatial localization of the electronic orbitals induces pronounced vertical and horizontal patterns, which are naturally compatible with a low-rank description.

This behavior is more accentuated in silicon, due to its non-polar nature, whereas in lithium fluoride a finite long-range background is present as a consequence of polar coupling. Nevertheless, this background does not significantly compromise the overall compression performance. As shown in Fig. 4.8, in the Wannier case even a small fraction of the retained information (of the order of 4%) is sufficient to reconstruct most of the tensor amplitude, while in the Bloch representation a comparable truncation clearly fails to capture the relevant structure.

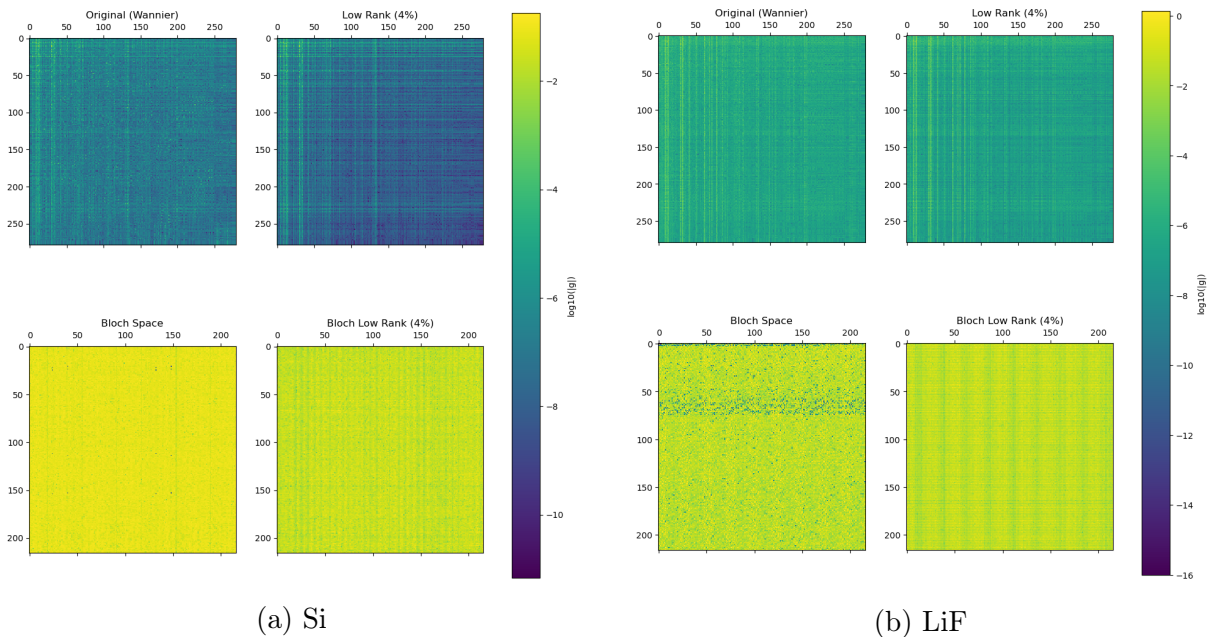


**Figure 4.8:** Heat-map representation of the electron–phonon coupling tensor for a fixed triplet of band and phonon-mode indices. **Left:** silicon (covalent semiconductor). **Right:** lithium fluoride (polar insulator). The Wannier representation reveals a structured, low-rank-like pattern absent in the Bloch representation.

Beyond compression, the global Tucker decomposition can also be exploited as a data-analysis tool in high-dimensional space, in particular to probe the structure of the electron–phonon matrix directly in the Bloch representation. A natural example is the analysis of the energy distribution over electronic bands, defined as a quantity proportional to the squared amplitude of the matrix elements, in close analogy with signal theory.

For a Tucker decomposition at rank  $r$ , the band-resolved energy can be evaluated directly from the core tensor as

$$E_m^{(r)} \propto \sum_{R_k, R_q, R_\nu, R_n} \left| C_{R_k R_q R_\nu R_n m}^{(r)} \right|^2, \quad (4.36)$$

where  $\mathcal{C}^{(r)}$  denotes the Tucker core at rank  $r$ , and  $m$  labels the final electronic band. The proportionality constant is irrelevant when considering relative distributions.

Figure 4.9(b) shows that the correct reconstruction of the absolute band-resolved energy contributions requires the Tucker rank to approach that of the full tensor. This reflects the fact that the total norm of the electron–phonon matrix is recovered only when a sufficiently large number of latent components is retained.

In contrast, when considering the normalized quantities  $E_m^{(r)} / \sum_{m'} E_{m'}^{(r)}$ , Fig. 4.9(a) demonstrates that the relative distribution among different final bands converges rapidly with rank. This indicates that the Tucker decomposition captures the structural information, namely, the relative importance of different scattering bands, at significantly lower rank than required to reproduce the absolute energy scale.

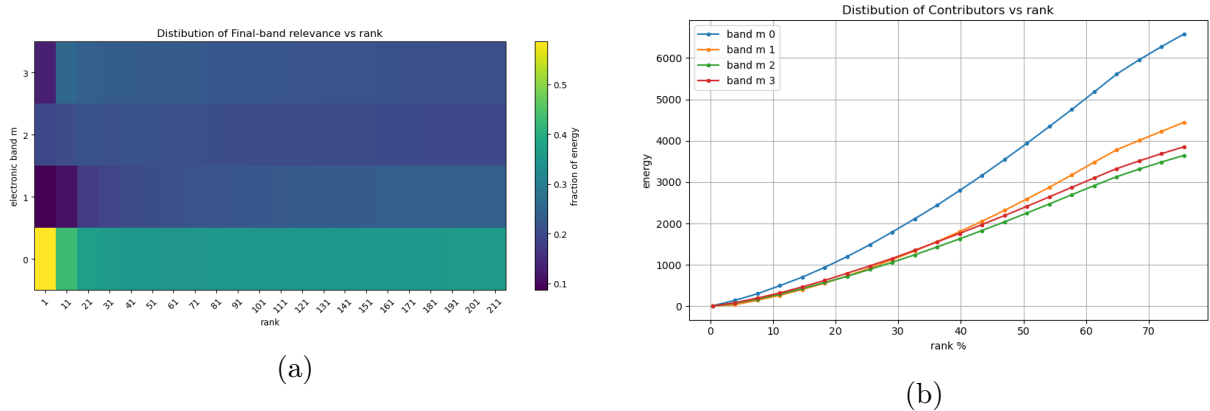


**Figure 4.9:** Learning band-resolved structure versus total energy in the Tucker decomposition for silicon. **(a)** Heat-map of the normalized fraction of the electron–phonon coupling norm associated with different final electronic bands as a function of the Tucker rank. **(b)** Cumulative contribution to the total coupling norm versus rank for the same bands. While the relative distribution among bands stabilizes at low rank, the total norm converges more gradually, indicating that structural information is captured earlier than the absolute energy scale.

### 4.3. Interpolation

The locality of Wannier orbitals and of the deformation potential implies a rapid decay of the Hamiltonian and electron–phonon matrix elements in real space. As a consequence, their Fourier transforms can be accurately reconstructed on arbitrarily dense momentum grids starting from data computed on a coarse mesh. The interpolation error is controlled by the truncation of long-range real-space contributions, which are negligible when the

Wannier representation is sufficiently localized. For this reason, Wannier interpolation has become a standard and highly reliable technique in first-principles electronic-structure calculations[8? ].

### 4.3.1. Wannier Interpolation

The fundamental transformation relating the diagonal eigenvalues to the Wannier Hamiltonian is defined as follows:

$$H_{mn}^{el}(\mathbf{k}') = U_{im}^\dagger(\mathbf{k}') \left[ \frac{1}{N_e} \sum_{\mathbf{R}_e} e^{i\mathbf{k}' \cdot \mathbf{R}_e} H_{ij}^{el}(\mathbf{R}_e) \right] U_{nj}(\mathbf{k}') = \delta_{mn} \varepsilon_{n\mathbf{k}'}.$$
 (4.37)

At this stage, the transformation matrices  $U(\mathbf{k}')$  at arbitrary momenta are unknown, since the Bloch eigenstates at  $\mathbf{k}'$  have not been computed. However, by construction the Hamiltonian on the left-hand side of Eq. 4.37 must be diagonal in the band indices. This implies that  $U(\mathbf{k}')$  is simply the matrix that diagonalizes the Fourier-transformed Wannier Hamiltonian inside the brackets.

Therefore, the electronic structure at any  $\mathbf{k}'$  can be obtained through two steps:

1. Fourier interpolation of the Hamiltonian in the Wannier representation.
2. Diagonalization of the resulting matrix.

This yields the eigenvalues  $\varepsilon_{n\mathbf{k}'}$ , the rotation matrices  $U(\mathbf{k}')$ , and consequently the Bloch eigenstates at arbitrary momenta. An example of the interpolated band structure is shown in Fig. 4.10.

In practical implementations, the sum over  $\mathbf{R}_e$  is performed over a Wigner–Seitz supercell, including appropriate boundary weights to preserve crystal symmetry. Additionally, in the presence of degeneracies, the diagonalization defines eigenvectors only up to a unitary transformation within the degenerate subspace. Care must therefore be taken if a smooth gauge is required for derivative-based quantities.

### 4.3.2. Disentanglement

Wannier interpolation becomes more subtle when the bands of interest do not form an isolated manifold. This occurs, for instance, for the conduction bands of silicon or in metallic systems, where target bands are entangled with higher-energy states.

Attempting to isolate such bands using a sharp energy cutoff leads to discontinuities in

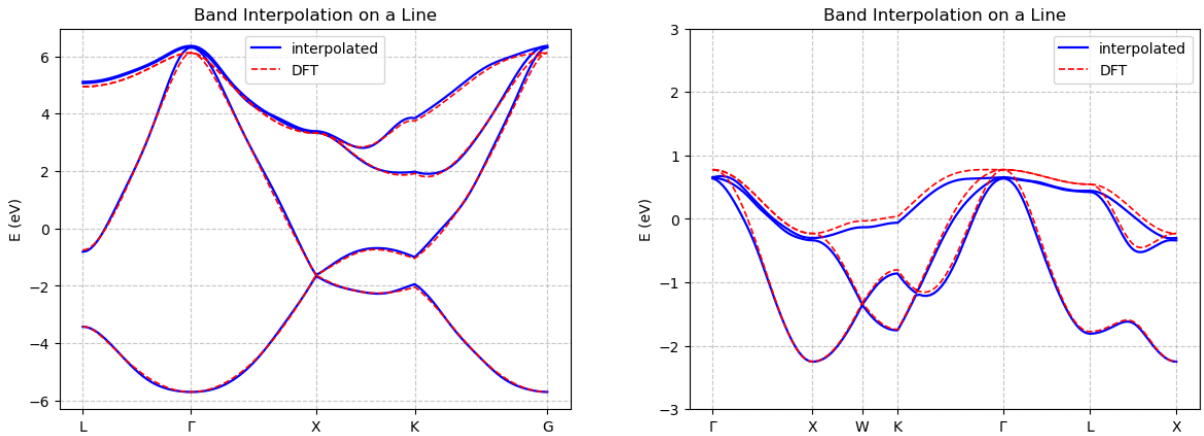


**Figure 4.10:** Wannier-interpolated electronic band structures along high-symmetry paths. **Left:** Silicon (four highest valence bands). **Right:** Lithium fluoride (three highest valence bands). The interpolation is performed from a  $6 \times 6 \times 6$  coarse grid computed with QE+EPW. Red curves correspond to independent VASP calculations. The excellent agreement confirms the accuracy of the Fourier interpolation procedure.

$\mathbf{k}$ -space and results in spurious oscillations in the interpolated bands, a numerical artifact analogous to the Gibbs phenomenon [8].

The standard solution is the disentanglement procedure of Souza, Marzari, and Vanderbilt. One defines an outer energy window containing  $N_{\text{win}}$  Bloch states, larger than the number of desired Wannier functions  $N_W$ . An optimal subspace is then constructed via a rectangular, semi-unitary transformation matrix  $U(\mathbf{k})$ :

$$|\phi_{i\mathbf{k}}\rangle = \sum_{m=1}^{N_{\text{win}}} U_{mi}(\mathbf{k}) |\psi_{m\mathbf{k}}\rangle, \quad U^\dagger(\mathbf{k}) U(\mathbf{k}) = \mathbb{I}_{N_W}. \quad (4.38)$$

To ensure that physically relevant bands are exactly reproduced, a frozen window is typically introduced. Inside this inner window the Bloch states are preserved one-to-one, while outside it the algorithm optimizes band mixing to achieve maximal smoothness in  $\mathbf{k}$ -space. An example for silicon is shown in Fig. 4.11. The interpolation remains accurate within the frozen window, while bands above the cutoff may exhibit oscillations due to residual mixing.

### 4.3.3. Phonon Interpolation

The vibrational spectrum can be interpolated analogously by exploiting the real-space decay of the interatomic force constants. The squared phonon frequencies at arbitrary  $\mathbf{q}'$

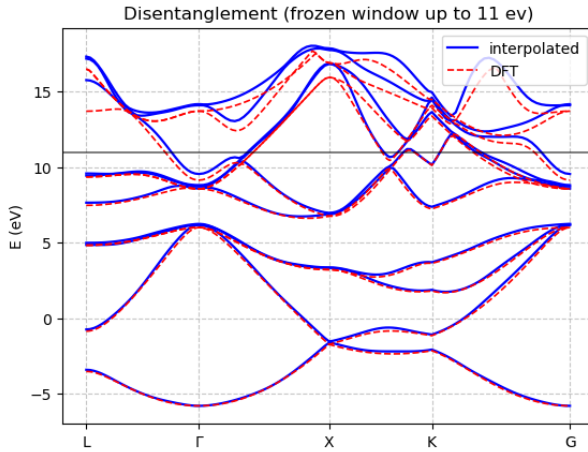


**Figure 4.11:** Interpolation of the four highest valence bands of Si together with selected conduction bands. The black horizontal line at 11 eV marks the frozen window boundary. Bands below this threshold are accurately reproduced, while those above may display oscillatory behavior. Higher bands are nevertheless required to properly describe the entangled manifold.

are obtained from the real-space dynamical matrix via

$$D_{\mu\nu}(\mathbf{q}') = \sum_{\kappa\alpha,\kappa'\beta} e_{\kappa\alpha,\nu}^*(\mathbf{q}') \left[ \frac{1}{N_p} \sum_{\mathbf{R}_p} e^{i\mathbf{q}' \cdot \mathbf{R}_p} D_{\kappa\alpha,\kappa'\beta}(\mathbf{R}_p) \right] e_{\kappa'\beta,\mu}(\mathbf{q}') = \delta_{\nu\mu} \omega_{\mathbf{q}'\nu}^2. \quad (4.39)$$

The polarization vectors and squared frequencies are obtained by diagonalizing the Fourier-transformed dynamical matrix inside the brackets. This allows efficient computation of phonon dispersions on dense grids starting from coarse-grid DFT calculations.

Unlike the electronic case, interatomic force constants may decay slowly, particularly in polar materials where long-range dipole–dipole interactions are present. Truncation of these long-range contributions introduces finite-size effects and may violate translational invariance. Physically, acoustic phonon frequencies must vanish at  $\Gamma$ ; truncation errors disrupt this cancellation and may lead to small negative or imaginary frequencies.

To correct this artifact, the Acoustic Sum Rule (ASR) is typically imposed, enforcing that the total force on the unit cell vanishes under rigid translation.

#### 4.3.4. Matrix Element Interpolation

Finally, we reach the central objective of this work: the evaluation of the electron–phonon interaction vertex  $g_{mn,\nu}(\mathbf{k}, \mathbf{q})$  at arbitrary points in the Brillouin zone. Having established

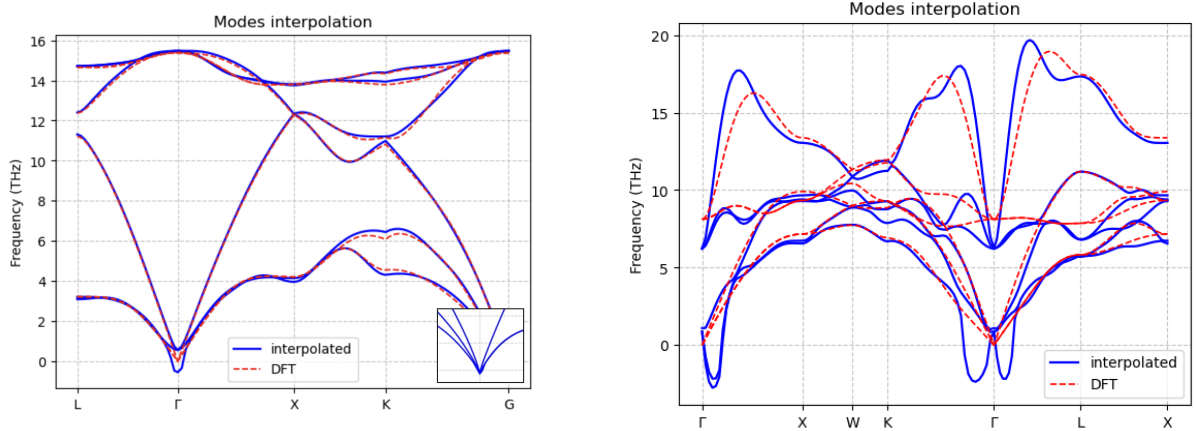


**Figure 4.12:** Wannier-interpolated phonon dispersions from a  $6 \times 6 \times 6$  coarse grid computed with QE+EPW. Red curves correspond to independent finite-difference VASP calculations. No ASR is imposed. **Left (Si):** Good overall agreement is observed; small negative frequencies at  $\Gamma$  arise from finite-size effects. The inset shows results from a  $10 \times 10 \times 10$  grid, which restores the correct acoustic behavior. **Right (LiF):** Stronger oscillations and imaginary frequencies appear due to long-range dipole interactions. No LO–TO correction is included.

interpolation protocols for both electronic states and vibrational modes, these ingredients can now be combined consistently.

As in the previous cases, the key observation is that the coupling tensor in the Wannier representation,  $g_{ij,\kappa\alpha}(\mathbf{R}_e, \mathbf{R}_p)$ , is expressed in terms of localized electronic orbitals and atomic displacements, and therefore decays rapidly in real space. The vertex at a new pair of wavevectors  $(\mathbf{k}', \mathbf{q}')$  is obtained by a double Fourier transform in the electronic and phononic lattice vectors, followed by the appropriate unitary rotations into the Bloch and phonon eigenmode bases.

The standard interpolation formula, obtained by inverting Eq. (4.25), reads

$$\begin{aligned}
 g_{mn,\nu}(\mathbf{k}', \mathbf{q}') &= \langle m\mathbf{k}' + \mathbf{q}' | \partial_{\mathbf{q}'\nu} V | n\mathbf{k}' \rangle \\
 &= \sum_{\mathbf{R}_e, \mathbf{R}_p} e^{i(\mathbf{k}' \cdot \mathbf{R}_e + \mathbf{q}' \cdot \mathbf{R}_p)} \sum_{i,j} \sum_{\kappa\alpha} U_{mi}^\dagger(\mathbf{k}' + \mathbf{q}') \left[ \left( \frac{M_0}{M_\kappa} \right)^{1/2} g_{ij,\kappa\alpha}(\mathbf{R}_e, \mathbf{R}_p) \right] U_{jn}(\mathbf{k}') e_{\kappa\alpha,\nu}(\mathbf{q}').
 \end{aligned} \tag{4.40}$$

Equation (4.40) highlights the structure of the interpolation scheme: (i) a real-space

summation weighted by phase factors corresponding to a Fourier Transformation (ii) a rotation into the Bloch basis via  $U(\mathbf{k})$ , and (iii) a projection onto phonon eigenmodes through the polarization vectors  $e_{\kappa\alpha,\nu}(\mathbf{q})$ . All quantities required for this construction are obtained on demand from the previously interpolated electron and phonon matrix elements.

To assess the accuracy of the procedure, we evaluate the mode-resolved coupling strength defined following Ref. [26]:

$$D_\nu(\mathbf{q}) = \hbar^{-1} \sqrt{\frac{2\omega_{\nu\mathbf{q}} M_{\text{uc}}}{N_b} \sum_{mn} |g_{mn\nu}(\mathbf{k} = \Gamma, \mathbf{q})|^2}, \quad (4.41)$$

where  $M_{\text{uc}}$  is the mass of the unit cell and the sum runs over the selected band manifold. This quantity provides a compact measure of the momentum- and mode-dependent electron–phonon interaction strength.

Figures 4.13 show the resulting  $D_\nu(\mathbf{q})$  along high-symmetry paths for silicon and lithium fluoride. The full interpolation (blue curves) is already obtained within the Wannier interpolation scheme and displays very good agreement with literature results for silicon, both in magnitude and dispersion trends, confirming the correctness of Eq. (4.40) and of the implemented rotation procedure, up to finite size error, boundary condition and degeneracy issues.

The deviations observed in the compressed schemes therefore originate solely from the low-rank approximation of the Wannier-space tensor. At reduced rank, the decomposition efficiently captures the dominant, spatially localized components of  $g_{ij,\kappa\alpha}(\mathbf{R}_e, \mathbf{R}_p)$ , while more homogeneous and extended background contributions are only partially retained, which suggest to renounce to some compression to achieve more reliable results. Since Eq. (4.40) involves a coherent double Fourier summation over all lattice vectors, even small long-range components can interfere constructively in momentum space. Their truncation manifests as mild oscillatory artifacts, particularly near extrema of the dispersion. Despite this, the hierarchy of phonon branches and the overall momentum dependence remain robust, indicating that the essential electron–phonon interaction is largely captured within a reduced-rank representation of the Wannier tensor.

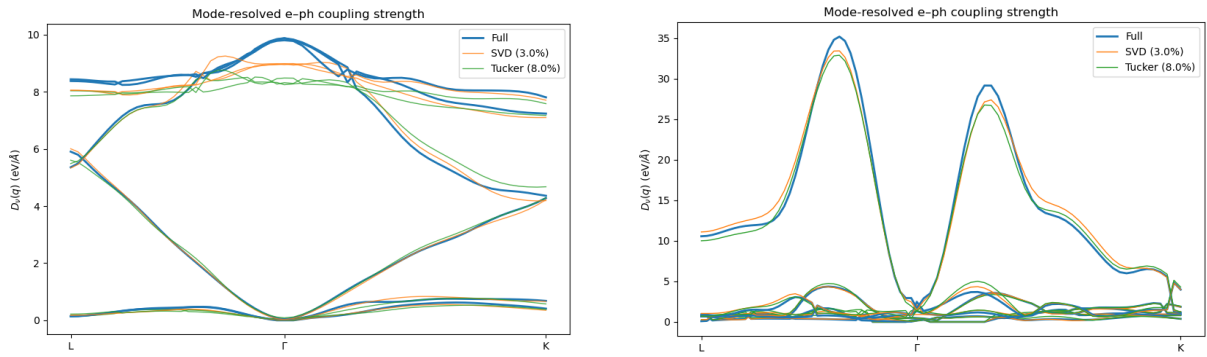


**Figure 4.13:** Mode-resolved electron–phonon coupling strength  $D_n(\mathbf{q})$  defined in Eq. (4.41), evaluated along the  $L\text{-}\Gamma\text{-}K$  high-symmetry path. **Left:** Silicon. **Right:** Lithium fluoride. The full interpolation scheme (blue) is compared with compressed representations obtained using SVD (3%) and Tucker ( $\sim 8\%$ ). The complete interpolation reproduces the expected dispersion and peak structure in agreement with literature results. The reduced-rank schemes preserve the dominant phonon branches and overall momentum dependence, while small oscillatory deviations near extrema arise.



# 5 | Back to Monte Carlo

## 5.1. Interpolation performance

Formulae such as Eq. (4.40) correspond to the standard implementation of electron–phonon interpolation adopted in widely used codes such as EPW or VASP. A closer inspection, however, reveals a clear computational bottleneck in the evaluation of the real-space Fourier transform,

$$g_{mn,\nu}(\mathbf{k}', \mathbf{q}') = \dots \left[ \sum_{\mathbf{R}_e, \mathbf{R}_p} e^{i(\mathbf{k}' \cdot \mathbf{R}_e + \mathbf{q}' \cdot \mathbf{R}_p)} g_{ij,\kappa\alpha}(\mathbf{R}_e, \mathbf{R}_p) \right] \dots, \quad (5.1)$$

namely the double summation over electronic ( $\mathbf{R}_e$ ) and phononic ( $\mathbf{R}_p$ ) lattice vectors. In a brute-force implementation, this step scales as  $\mathcal{O}(N_{R_e} N_{R_p})$  and rapidly becomes the dominant cost for large Wannier supercells or dense sampling, representing a severe limitation for Diagrammatic Monte Carlo (DMC) applications, where millions of vertices must be evaluated on the fly.

A substantial improvement is obtained by exploiting the low-rank structure of the real-space interaction tensor discussed in the previous sections. By inserting the sliced-SVD decomposition of Eq. (4.28) into Eq. (4.40), the double Fourier sum factorizes into two independent single sums,

$$\begin{aligned} g_{mn,\nu}^{(r)}(\mathbf{k}', \mathbf{q}') &= \sum_{i,j} \sum_{k\alpha} \sum_{\tilde{r}=1}^r \sigma_{\tilde{r}ijk\alpha} \left( \frac{M_0}{M_k} \right)^{\frac{1}{2}} U_{mi}^\dagger(\mathbf{k}' + \mathbf{q}') \\ &\times \left( \sum_{\mathbf{R}_e} e^{i\mathbf{k}' \cdot \mathbf{R}_e} u_{\tilde{r}ik\alpha}(\mathbf{R}_e) \right) \left( \sum_{\mathbf{R}_p} e^{i\mathbf{q}' \cdot \mathbf{R}_p} v_{\tilde{r}jk\alpha}(\mathbf{R}_p) \right) \\ &\times U_{jn}(\mathbf{k}') e_{\kappa\alpha,\nu}(\mathbf{q}'). \end{aligned} \quad (5.2)$$

As a consequence, the computational complexity of the interpolation step is reduced from

quadratic to linear in the grid size,

$$\mathcal{O}(N_{R_e} N_{R_p}) \longrightarrow \mathcal{O}((N_{R_e} + N_{R_p}) r), \quad (5.3)$$

where  $r \ll \min(N_{R_e}, N_{R_p})$  is the retained SVD rank.

A similar strategy can be applied when using the partially truncated Tucker representation introduced in Eq. (4.34b), where band and mode indices are kept at full rank and only the spatial directions are compressed. In this case the interpolated matrix elements read

$$\begin{aligned} g_{mn,\nu}^{(r)}(\mathbf{k}', \mathbf{q}') &= \sum_{i,j} \sum_{\tilde{\nu}} \left( \frac{M_0}{M_{\tilde{\nu}}} \right)^{\frac{1}{2}} U_{mi}^{\dagger}(\mathbf{k}' + \mathbf{q}') \\ &\times \sum_{r_e=1}^r \sum_{r_p=1}^r C_{r_e r_p i j \tilde{\nu}} \left( \sum_{\mathbf{R}_e} e^{i \mathbf{k}' \cdot \mathbf{R}_e} a^{r_e}(\mathbf{R}_e) \right) \left( \sum_{\mathbf{R}_p} e^{i \mathbf{q}' \cdot \mathbf{R}_p} a^{r_p}(\mathbf{R}_p) \right) \\ &\times U_{jn}(\mathbf{k}') e_{\tilde{\nu},\nu}(\mathbf{q}'). \end{aligned} \quad (5.4)$$

The Fourier transforms of the spatial basis functions scale as  $\mathcal{O}(N_{R_e} r)$  and  $\mathcal{O}(N_{R_p} r)$ , while the subsequent contraction with the core tensor introduces an additional  $\mathcal{O}(r^2)$  cost. The overall complexity therefore becomes

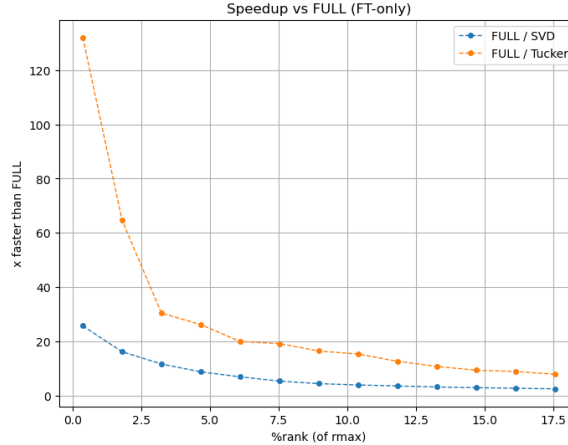
$$\mathcal{O}(N_{R_e} N_{R_p}) \longrightarrow \mathcal{O}((N_{R_e} + N_{R_p}) r) + \mathcal{O}(r^2), \quad (5.5)$$

which remains strongly advantageous in the empirically observed low-rank regime  $r \ll N_{R_e}, N_{R_p}$ .

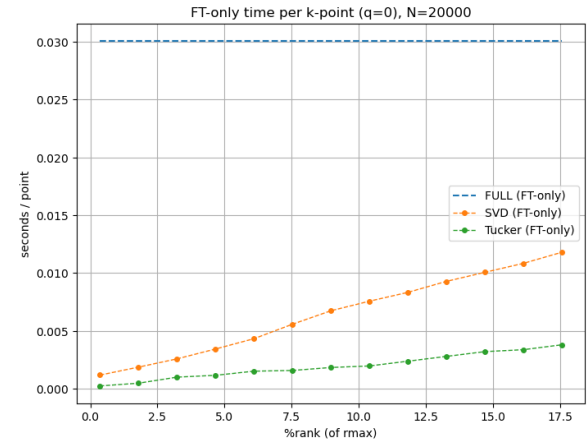
**Numerical performance.** Benchmark tests performed on the developed code for  $N = 10^4 - 2 \times 10^4$  random  $\mathbf{k}$ -points confirm the expected scaling. Figure 5.1 shows both the absolute time per  $\mathbf{k}$ -point and the speedup relative to the full (uncompressed) Fourier transform. In the current Python implementation, the Tucker-based interpolation consistently outperforms the sliced-SVD approach at fixed rank. This is likely due to the tensorial structure of the Tucker formulation, which allows more efficient use of vectorized linear algebra kernels in scientific Python libraries.

In both approaches, an optimal trade-off between accuracy and performance is reached at moderate compression ratios. Consistently with the compression analysis of the previous section, SVD achieves negligible reconstruction error already at  $\sim 2\%$  of the maximal rank, while Tucker requires  $\sim 8\%$ , with the opposite trend in terms of storage requirements. In this regime the interpolation performance of the two methods is comparable, while at

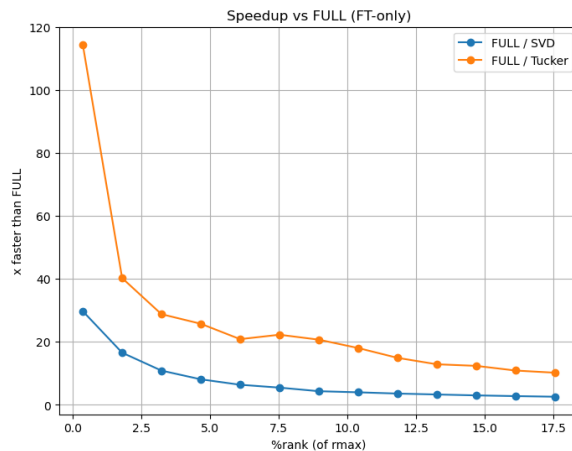
lower ranks Tucker offers a significantly larger speedup at the price of a controlled loss of accuracy.



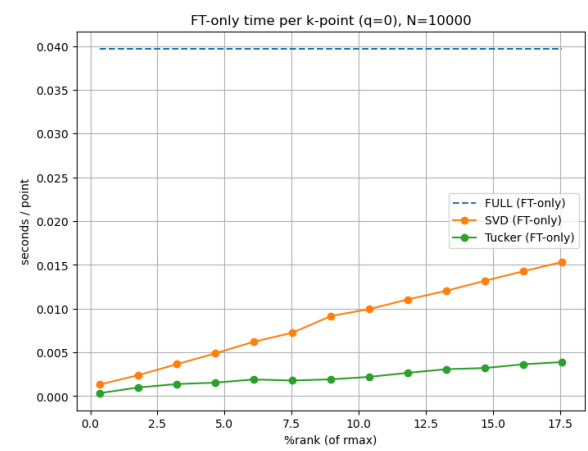
(a) Si: speedup vs rank



(b) Si: time per k-point



(c) LiF: speedup vs rank



(d) LiF: time per k-point

Figure 5.1: Interpolation performance for Silicon and LiF. Top row: speedup with respect to the full real-space Fourier transform. Bottom row: absolute interpolation time per  $\mathbf{k}$ -point. Both sliced-SVD and Tucker-based schemes achieve substantial acceleration, with Tucker providing the largest speedup at fixed rank in the present implementation.

This improvement enables the evaluation of electron–phonon matrix elements on ultra-dense momentum grids directly on the fly, with a fraction of the memory and computational cost required by standard approaches. This capability is essential for achieving convergence in Diagrammatic Monte Carlo simulations and represents a key practical outcome of the tensor-based compression strategy developed in this work.

## 5.2. Sign Problem

In order to stress-test the momentum- and band-resolved implementation, we introduced two additional ingredients beyond the standard breathing model: (i) a fictitious multiband electronic dispersion and (ii) a complex phase in the electron–phonon coupling of the form

$$\varepsilon_m(k) = -2t \cos(mk) - \Delta_m \quad (5.6)$$

$$g_{mn}(q) = 2g \sin\left(\frac{q}{2}\right) e^{i\phi(q)}, \quad \phi(q) = \alpha q(m - n) \quad (5.7)$$

Here  $m$  labels the band index and  $\Delta_m$  introduces an energy offset between bands. While the coupling resembles the breathing-mode structure, times an additional phase factor.

In the intraband limit, where only transitions within the same band are allowed (we just considered a phase  $\alpha q$ ), the phase contributions largely cancel along closed phonon lines, the Monte Carlo sampling remains stable and we do not see significative deviations in the Green function estimator.

In the multiband case, instead, the electron momentum and band index are modified along diagram segments, and the accumulated phase factors from different vertices no longer compensate pairwise. The Monte Carlo estimator becomes dominated by interference among configurations with different phases, leading to large fluctuations. This is the manifestation of the sign (or phase) problem that often arises in quantum Monte Carlo methods.



**Figure 5.2:** Improved Green-function estimator for different coupling scenarios. **Left:** Intraband breathing model with complex phase; the estimator remains stable. **Center and Right:** Multiband dispersion with phase-dependent coupling; strong oscillations and rapidly growing fluctuations signal the onset of a severe phase problem.

Figure 5.2 summarizes this behavior. The first panel shows the intraband case, where the improved Green-function estimator remains stable even with complex coupling. The second and third panels correspond to the multiband dispersion: strong oscillations appear

and the estimator becomes unstable.

Several strategies have been proposed in the literature to mitigate such phase problems. For instance, matrix-product-based techniques have recently been employed to reorganize the diagrammatic expansion in a more stable form [27]. A more solid approach is provided by *Bold Diagrammatic Monte Carlo* [33], where the stochastic sampling is embedded within a self-consistent loop and diagrams are constructed using dressed (bold) propagators. Remarkably, in this framework a moderate sign problem may even improve convergence by stabilizing the fixed-point iteration.

### 5.3. Conclusions and Further Developments

At the time of writing this thesis, the procedures described here, in particular those presented in Chapter 4, have been tested first within VASP and subsequently within the Quantum Espresso + EPW pipeline. Only the latter environment allowed us to reproduce the results reported in the literature. The methodology was benchmarked on two physically very different systems, LiF and Si, which nevertheless exhibited qualitatively similar behavior in terms of compressibility. This suggests that the possibility of obtaining an efficient low-rank representation should be attributed primarily to the localized nature of the Wannier representation, rather than to specific properties of the individual materials.

At the same time, it is important to stress that the main achievement of this work is neither the good compression ratios obtained, although these are certainly beneficial in terms of memory usage, nor the claim of being able to interpolate on extremely dense meshes, a task that is already reliably handled by established Wannier-interpolation libraries. The real motivation lies elsewhere: the direct application of Wannier interpolation inside Diagrammatic Monte Carlo is obstructed by the bottleneck introduced by the need to perform millions of interpolations per second during Monte Carlo updates. Our analysis shows that the true computational bottleneck is the double Fourier transform over the real- and reciprocal-space meshes on which the dataset is defined, whose cost scales quadratically with the number of grid points. By contrast, the diagonalization of the dynamical matrix and of the electronic Hamiltonian, required to obtain the rotation matrices, has negligible cost since it involves matrices of size equal to the number of bands or phonon modes considered.

The advantage of Tucker and SVD decompositions is therefore the factorization of the Wannier-space tensor, reducing the quadratic scaling to an effectively linear one in the low-rank regime. In practice, we observe speed-ups of approximately one order of magni-

tude. Tucker decomposition requires a more demanding preprocessing stage but provides additional physical insight and allows the use of modern tensor-based computational tools. While the gain for a single interpolated data point may appear modest, it becomes significant when accumulated over the large number of evaluations required in DiagMC.

For coarse  $6 \times 6 \times 6$  grids, the entire factorization procedure can be carried out locally. For denser meshes, often necessary for accurate phonon dispersions, the memory requirements increase substantially. For instance, a  $10 \times 10 \times 10$  grid required approximately 96 GB of RAM on one node of the VSC cluster, with a preprocessing time of about half an hour for the SVD.

In an ideal development, given the presence of several delicate aspects in fully faithful Wannier interpolation, such as disentanglement, acoustic sum rule enforcement, boundary conditions, and LO–TO splitting, it would be desirable to integrate the tensor factorization and DiagMC interface directly within established electronic-structure codes capable of performing accurate interpolation, such as VASP or EPW. A practical strategy would consist in computing and storing the factorization offline, and subsequently loading it into memory during the DiagMC simulation, which would then perform the factorized Fourier transform on demand. As observed in our analysis, it is advisable not to optimize strictly at the compression–error tradeoff minimum, but rather to retain slightly higher ranks in order to capture small-amplitude yet long-range contributions that may be physically relevant.

All of this, of course, relies on a high-quality initial DFT calculation, which itself may present subtle numerical challenges.

Once integrated into Diagrammatic Monte Carlo, properly adapted to handle multiband sign-problem effects, and having partially validated our implementation, this framework has the potential to provide access to observables with a level of accuracy that is difficult to achieve with other methods. In particular, the self-energy, from which many physical observables can be extracted in a controlled manner, becomes accessible without relying on uncontrolled approximations, even though the underlying electron–phonon matrix elements originate from first-principles calculations.

# Bibliography

- [1] Bryan O’Gorman, Sandy Irani, James Whitfield, and Bill Fefferman. Intractability of electronic structure in a fixed basis. *PRX Quantum*, 3(2):020322, 2022. doi: 10.1103/PRXQuantum.3.020322.
- [2] Neil W. Ashcroft and N. David Mermin. *Solid State Physics*. Saunders College, Philadelphia, 1976. ISBN 9780030839931.
- [3] Michael Tinkham. *Group Theory and Quantum Mechanics*. Dover Publications, 2003.
- [4] Nicola Marzari, Arash A. Mostofi, Jonathan R. Yates, Ivo Souza, and David Vanderbilt. Maximally localized wannier functions: Theory and applications. *Reviews of Modern Physics*, 84:1419–1475, 2012. doi: 10.1103/RevModPhys.84.1419.
- [5] David S. Sholl and Janice A. Steckel. *Density Functional Theory: A Practical Introduction*. Wiley, Hoboken, New Jersey, 2009. ISBN 9780470408953.
- [6] Alexander L. Fetter and John Dirk Walecka. *Quantum Theory of Many-Particle Systems*. McGraw–Hill, New York, 1971.
- [7] Luca Guido Molinari. Second quantization, 2023. Lecture notes, Università degli Studi di Milano.
- [8] Manuel Engel. *Electron-Phonon Interactions Using the Projector-Augmented-Wave Method*. Doctoral thesis, University of Vienna, Vienna, Austria, 2023. Supervisor: Georg Kresse.
- [9] Stefano Baroni, Stefano de Gironcoli, Andrea Dal Corso, and Paolo Giannozzi. Phonons and related crystal properties from density-functional perturbation theory. *Rev. Mod. Phys.*, 73:515–562, 2001. doi: 10.1103/RevModPhys.73.515.
- [10] VASP Wiki contributors. Phonons: Theory — density functional perturbation theory. [https://vasp.at/wiki/Phonons:\\_Theory#Density\\_functional\\_perturbation\\_theory](https://vasp.at/wiki/Phonons:_Theory#Density_functional_perturbation_theory), . Accessed: 2026-02-XX.

- [11] Feliciano Giustino. Electron-phonon interactions from first principles. *Rev. Mod. Phys.*, 89:015003, Feb 2017. doi: 10.1103/RevModPhys.89.015003.
- [12] Stefano Ragni. Diagrammatic monte carlo study of the holstein polaron. Master’s thesis, Alma Mater Studiorum – University of Bologna, Bologna, Italy, 2019-2020. Supervisor: Cesare Franchini; Co-supervisor: Thomas Hahn.
- [13] VASP Wiki contributors. Electron-phonon interactions — vasp wiki. [https://vasp.at/wiki/Category:Electron-phonon\\_interactions](https://vasp.at/wiki/Category:Electron-phonon_interactions), . Accessed: 2026-02-XX.
- [14] Marios Zacharias and Feliciano Giustino. One-shot calculation of temperature-dependent optical spectra and phonon-induced band-gap renormalization. *Physical Review B*, 94(075125), 2016. doi: 10.1103/PhysRevB.94.075125.
- [15] Piers Coleman. *Introduction to Many-Body Physics*. Cambridge University Press, Cambridge, 2015. ISBN 978-0-521-86488-6.
- [16] Murray Gell-Mann and Francis E. Low. Bound states in quantum field theory. *Physical Review*, 84(2):350–354, 1951. doi: 10.1103/PhysRev.84.350.
- [17] Luca Guido Molinari. The gell-mann and low theorem and the reduction formula, 2017. Lecture notes.
- [18] Hartmut Haug and Stephan W. Koch. *Quantum Theory of the Optical and Electronic Properties of Semiconductors*. World Scientific Publishing Co., Singapore, 4th edition, 2004. ISBN 9789812387561.
- [19] N. V. Prokof’ev and B. V. Svistunov. Polaron problem by diagrammatic quantum monte carlo. *Phys. Rev. Lett.*, 81:2514–2517, 1998. doi: 10.1103/PhysRevLett.81.2514.
- [20] A. S. Mishchenko, N. V. Prokof’ev, A. Sakamoto, and B. V. Svistunov. Diagrammatic quantum monte carlo study of the fröhlich polaron. *Phys. Rev. B*, 62:6317–6336, 2000. doi: 10.1103/PhysRevB.62.6317.
- [21] J. E. Gubernatis, N. Kawashima, and P. Werner. *Quantum Monte Carlo Methods: Algorithms for Lattice Models*. Cambridge University Press, Cambridge, 2016. ISBN 978-1-107-00642-0.
- [22] M. Berciu. Green’s function of a dressed particle. *Physical Review Letters*, 97:036402, 2006. doi: 10.1103/PhysRevLett.97.036402.
- [23] M. Berciu and H. Fehske. Momentum average approximation for models with elec-

- tron–phonon coupling dependent on the phonon momentum. *Physical Review B*, 82: 085116, 2010. doi: 10.1103/PhysRevB.82.085116.
- [24] Feliciano Giustino, Marvin L. Cohen, and Steven G. Louie. Electron-phonon interaction using wannier functions. *Physical Review B*, 76(16):165108, October 2007. doi: 10.1103/PhysRevB.76.165108.
- [25] Manuel Engel, Martijn Marsman, Cesare Franchini, and Georg Kresse. Electron-phonon interactions using the projector augmented-wave method and wannier functions. *Physical Review B*, 101:184302, 2020. doi: 10.1103/PhysRevB.101.184302.
- [26] Yao Luo, Dhruv Desai, Benjamin K. Chang, Jinsoo Park, and Marco Bernardi. Data-driven compression of electron-phonon interactions. *Phys. Rev. X*, 14:021023, 2024. doi: 10.1103/PhysRevX.14.021023.
- [27] Y. Luo, J. Park, and M. Bernardi. First-principles diagrammatic monte carlo for electron–phonon interactions and polaron. *Nature Physics*, 21:1275–1282, 2025. doi: 10.1038/s41567-025-02954-1.
- [28] Samuel Poncé, Elena R. Margine, Claudio Verdi, and Feliciano Giustino. Epw: Electron-phonon coupling, transport and superconducting properties using maximally localized wannier functions. *Computer Physics Communications*, 209:116–133, 2016. doi: 10.1016/j.cpc.2016.07.028.
- [29] Arash A. Mostofi, Jonathan R. Yates, Young-Su Lee, Ivo Souza, David Vanderbilt, and Nicola Marzari. wannier90: A tool for obtaining maximally-localised wannier functions. *Computer Physics Communications*, 178:685–699, 2008. doi: 10.1016/j.cpc.2007.11.016.
- [30] Avrim Blum, John Hopcroft, and Ravindran Kannan. Singular value decomposition (svd), 2020. Lecture Notes / Chapter from Foundations of Data Science.
- [31] Lieven De Lathauwer, Bart De Moor, and Joos Vandewalle. A multilinear singular value decomposition. *SIAM Journal on Matrix Analysis and Applications*, 21(4): 1253–1278, 2000.
- [32] Tamara G. Kolda and Brett W. Bader. Tensor decompositions and applications. *SIAM Review*, 51(3):455–500, 2009.
- [33] Nikolay Prokof’ev and Boris Svistunov. Bold diagrammatic monte carlo technique: When the sign problem is welcome. *Physical Review Letters*, 99:250201, 2007. doi: 10.1103/PhysRevLett.99.250201.



# A | Appendix A

If you need to include an appendix to support the research in your thesis, you can place it at the end of the manuscript. An appendix contains supplementary material (figures, tables, data, codes, mathematical proofs, surveys, . . .) which supplement the main results contained in the previous chapters.



# B | Appendix B

## B.0.1. Add Update

We report here the constructive evaluation of the diagram-weight ratio associated with the insertion of a phonon line between imaginary times  $\tau_I$  and  $\tau_F$ , carrying momentum  $\mathbf{q}'$  and mode  $\nu'$ . The insertion is performed by introducing a creation vertex at  $\tau_I$ , which scatters the electron into band  $m'$ , and the corresponding annihilation vertex at  $\tau_F$ , after which the electron propagates in band  $m''$ .

Let  $\tau_i$  denote the time of the last existing vertex preceding  $\tau_I$  and  $\tau_j$  the time of the first existing vertex following  $\tau_F$  (with the conventions that the cases in which one of them does not exist are treated separately; see the code implementation). We define  $l = j - i$ , so that the interval  $(\tau_I, \tau_F)$  spans  $l - 1$  existing vertices in between.

The insertion produces three types of contributions. First, cutting the electron propagator on the segment  $(\tau_i, \tau_{i+1})$  at time  $\tau_I$  and assigning the outgoing band  $m'$  yields

$$F_1 = g_{m'm_i\nu'}(\mathbf{k}_i, \mathbf{q}') \frac{G_{m'\mathbf{k}_i+\mathbf{q}'}^{(0)}(\tau_{i+1} - \tau_I)}{G_{m_i\mathbf{k}_i}^{(0)}(\tau_{i+1} - \tau_I)} \frac{g_{m_{i+1}m'\nu_{i+1}}(\mathbf{k}_i + \mathbf{q}', \mathbf{q}_{i+1})}{g_{m_{i+1}m_i\nu_{i+1}}(\mathbf{k}_i, \mathbf{q}_{i+1})}. \quad (\text{B.1})$$

Here the last ratio accounts for the fact that the existing vertex at  $\tau_{i+1}$  receives an incoming electron state whose momentum has been shifted by  $\mathbf{q}'$  and whose band index has been changed from  $m_i$  to  $m'$ .

All intermediate vertices between  $\tau_{i+1}$  and  $\tau_{j-1}$  are affected only through the momentum shift  $\mathbf{k} \mapsto \mathbf{k} + \mathbf{q}'$  on the incoming electron line. This gives

$$F_2 = \prod_{p=1}^{l-2} \frac{G_{m_{i+p}\mathbf{k}_{i+p}+\mathbf{q}'}^{(0)}(\tau_{i+p+1} - \tau_{i+p})}{G_{m_{i+p}\mathbf{k}_{i+p}}^{(0)}(\tau_{i+p+1} - \tau_{i+p})} \frac{g_{m_{i+p+1}m_{i+p}\nu_{i+p+1}}(\mathbf{k}_{i+p} + \mathbf{q}', \mathbf{q}_{i+p+1})}{g_{m_{i+p+1}m_{i+p}\nu_{i+p+1}}(\mathbf{k}_{i+p}, \mathbf{q}_{i+p+1})}, \quad (\text{B.2})$$

with the convention that  $F_2 = 1$  whenever  $l \leq 2$  (empty product).

Finally, the insertion at  $\tau_F$  modifies the last shifted electron segment, introduces the annihilation vertex, and updates the electron propagator and (if present) the subsequent

vertex at  $\tau_j$  due to the change of outgoing band to  $m''$ :

$$F_3 = \frac{G_{m_{j-1} \mathbf{k}_{j-1} + \mathbf{q}'}^{(0)}(\tau_F - \tau_{j-1})}{G_{m_{j-1} \mathbf{k}_{j-1}}^{(0)}(\tau_F - \tau_{j-1})} g_{m'' m_{j-1} \nu'}(\mathbf{k}_{j-1} + \mathbf{q}', -\mathbf{q}') \frac{G_{m'' \mathbf{k}_j}^{(0)}(\tau_j - \tau_F)}{G_{m_j \mathbf{k}_j}^{(0)}(\tau_j - \tau_F)} \frac{g_{m_{j+1} m'' \nu_j}(\mathbf{k}_j, \mathbf{q}_j)}{g_{m_{j+1} m_j \nu_j}(\mathbf{k}_j, \mathbf{q}_j)}. \quad (\text{B.3})$$

Collecting all factors, the diagram weight ratio reads

$$\frac{W_{\text{add}}}{W} = D_{\nu' \mathbf{q}'}^{(0)}(\tau_F - \tau_I) F_1 F_2 F_3. \quad (\text{B.4})$$

The corresponding remove update yields the inverse ratio. In practice, when removing a phonon line, the stored electron momenta on the interval previously shifted by  $\mathbf{q}'$  must first be mapped back by subtracting  $\mathbf{q}'$  before reconstructing the numerator factors of the updated diagram.

## Acknowledgements

I would like to thank my supervisor, Professor Cesare Franchini, first for proposing the idea of this interesting project at the intersection of quantum many-body theory and advanced simulation and data analysis tools, and for giving me access to the computing infrastructure of the Vienna Scientific Cluster (VSC). Second, for his supervision during the different phases of the work, and last but not least, for giving me the opportunity to enter into contact with an exciting research environment between Bologna and Vienna.

In this sense, I would like to sincerely thank Dr. Stefano Ragni, who helped me in the first stage of the project by providing fundamental insight into the theoretical and implementation aspects of Diagrammatic Monte Carlo, together with Dr. Lorenzo Celiberti, who also provided useful support during the transition to Density Functional Theory simulations. Finally, last only in chronological order, I would like to thank Dr. Manuel Engel, who provided fundamental support in understanding the theory of electron–phonon interaction and Wannier interpolation, and guided me in the use of its implementation in the VASP code.

